Understanding Defects in Advanced Energy Materials from First-Principles Calculations

Ekta Arora

Department of Physics

Indian Institute of Technology Delhi

Understanding Defects in Advanced Energy Materials from First-Principles Calculations

by

Ekta Arora

Department of Physics

Submitted

in fulfillment of the requirements of the degree of Doctor of

Philosophy

to the

Indian Institute of Technology Delhi

Dedicated to

my parents and husband

Certificate

This is to certify that the thesis entitled **"Understanding Defects in Advanced Energy Materials from First-Principles Calculations"** being submitted by **Ekta Arora**, to the Indian Institute of Technology Delhi, for the award of the degree of **Doctor of Philosophy** in Physics is a record of bonafide research work carried out by her under my supervision and guidance. She has fulfilled the requirements for the submission of the thesis, which to the best of my knowledge has reached the required standard. The material contained in the thesis has not been submitted in part or full to any other University or Institute for the award of any degree or diploma.

Prof. Saswata Bhattacharya

Department of Physics,

Indian Institute of Technology Delhi,

Hauz Khas, New Delhi 110016, India.

Date:

Place: New Delhi

Acknowledgements

Abstract

With the world's growing energy needs and the exhausting supply of fossil fuels, it has become crucial to shift to renewable energy sources. The renewable energy sources that are cost-effective, environmentally friendly, and abundant in nature are the solution to the current situation. The advanced solid-state materials used for addressing environmental issues have drawn significant research attention. In this thesis, advanced energy materials and their crystal defects are investigated with state-of-the-art Density Functional Theory (DFT) and *ab-initio* thermodynamics. The thesis mainly addresses the three classes of advanced energy materials, viz., hydrogen-storage materials, electrocatalyst materials used in electrochemical reduction of CO_2 to CO, and solid-state electrolyte materials for the all-solid-state batteries.

Hydrogen is considered a clean, abundant, and thus, a promising alternative for fossil fuels. Complex metal hydrides are referred to as a suitable medium for the storage of hydrogen. The release of hydrogen from such materials is possible only in the presence of an appropriate catalyst. Transition metal (TM) atom dopants improve the desorption kinetics and environmental condition requirements. The mechanism of dehydrogenation from catalyzed complex metal hydrides involves the diffusion of hydrogen-related intrinsic defects. We emphasize the role of environmental conditions and doping on the relative stability of the H-related defects in $NaAlH_4$, a prototypical system widely studied for the application of hydrogen storage. Firstly, we examine the effect of temperature and pressure on H-related defects' stability and concentration by incorporating *ab initio* thermodynamics. Next, the most suitable TM atom dopants are selected based on various factors like stability, structural distortion, and change in concentration of intrinsic defects in dopants' presence.

Another way to solve environmental concerns is to lower the concentration of CO_2 in the atmosphere by chemically reduce CO_2 to various other critical industrial feedstocks. Electrochemical reduction (ECR) of CO_2 to CO is carried out in a cell where the cathode material works as an electrocatalyst. The Electrocatalyst is required to have high

Faradaic efficiency and product selectivity. Cu-based alloys and compounds are known to have sufficiently high Faradaic efficiency. Experimentally, it is observed that Cu-In-O nanocomposites exhibit very high electrocatalytic activity and product selectivity. Cu-In-O nanocomposites efficiently suppress competitive hydrogen evolution reactions. We validate the experimental findings through our computational investigations. We study the effect of point defects on the Cu-In-O nanocomposites' catalytic activity by inducing various vacancy defects in the nanocomposite. Further, we explain the role of In-atoms in enhancing the product selectivity by suppressing the competitive hydrogen evolution reactions.

Li-ion batteries are the leading energy storage technology with a wide range of applications in portable electronics and automobiles. The use of flammable liquid electrolytes inhibits their realization in large scale energy applications. Replacing liquid electrolytes with solid-state electrolytes as in all-solid-state batteries ensures safety with improved battery design. However, achieving high ionic conductivity and appropriate mechanical properties for a solid-state candidate material is a challenge. We determine the mechanical stability of various sulfide materials for electrolytic applications. We also investigate the role of point defects, viz. halide doping, in improving the candidate materials' mechanical properties. We perform *ab-initio* molecular dynamics simulations to estimate the materials' diffusional properties and select the best-suited material based on the diffusional properties. We also elucidate the role of Li-vacancy in enhancing the diffusion of Li-ions through the bulk of such materials.

Contents

List of Tables

List of Figures

Chapter 1

Introduction

The modern lifestyle of society has led to an ever-growing demand for energy resources. Fossil fuels, such as petroleum, coal, and gas, have been relied upon for more than a century to generate electricity, power automobiles, and run industries [1, 2]. These fossil fuels have various advantages, e.g., excellent efficiency and reliability. Besides, fossil fuels are readily available and can be found in abundance in almost every part of the world. They are mainly composed of carbon and hydrogen compounds that are chemically stable and do not form other products even if stored for a long time. Hence, they require simple setups and transportation infrastructures. Despite the numerous benefits of fossil fuels, their prolonged utilization has taken an enormous toll on the environment. Energy generation from fossil fuels involves various processes like extraction, transportation, and burning.

Extraction of the fossil fuels

Fossil fuels are produced from buried remains of plants and animals under extreme temperature and pressure conditions beneath the earth's surface for many centuries. They are extracted with the process of surface mining and well drilling. Surface and underground mining is usually done to extract coal. Coal mining has dangerous impacts on the

miners' health; it is the leading cause of pneumoconiosis, commonly known as "black lung disease". Besides, the mining process requires removing vegetation and natural habitats from the land area, followed by the blasting of land up to large depths with explosives. Thus, mining leads to land degradation. It makes the areas prone to landslides and mudslides. The mined earth is generally left barren for decades. Also, the excess soil and minerals dug out of the earth are eventually dumped into the nearby water bodies, which contaminates the water disturbing the ecological balance of aquatic life and causing severe health problems to the people in the affected area.

On the other hand, the extraction of oil and gas through drilling or hydraulic fracturing is equally detrimental to most of the world's health and safety. The underground water that comes to the surface contains high concentrations of heavy metals, radioactive materials, and hydrocarbons. Millions of gallons of wastewater are produced, which is hard to dispose of safely and is not suitable for drinking. Also, the chemicals used in hydraulic fracturing are dangerous and cause fatal diseases like cancer and various neurological disorders. Large areas of land are disrupted in drilling wells and placing pipelines, disturbing the wildlife habitats. Oil drilling is a major cause of oil pollutions, like oil spills. Excess oil is released into the environment, which deposits layers of oil on the sea's surface. The oil over the sea surface reduces dissolved oxygen concentration; hence, it is dangerous for aquatic life. It also limits the amount of sunlight reaching the animals underwater. Hence, overall, fossil fuel extraction from the earth's crust is detrimental to natural habitats, vegetation, and the affected area's major population.

Transportation of fossil fuels

Besides, the transportation of fossil fuels from the extraction site to the utility site creates much pollution. The coal is usually transported through railways or roadways transport systems. Coal dust is a significant cause of cardiovascular and respiratory ailments com-

mon in communities dwelling near such routes. The transportation of natural gas requires an extensive infrastructure of transmission pipelines. There is a high risk of gas leakage, which leads to methane emissions. Also, the high flammability of natural gas can cause catastrophic accidents. The transportation of oil occurs mainly through supertankers, rails, trucks, and pipelines. In all the routes, there is a severe risk of leakage and explosions. The other substantial problem that arises from oil leakage is oil spills, which are fatal for aquatic life. Therefore, transportation of oil and gas from the wellheads to operational sites can be hazardous for the environment.

Burning of the fossil fuels

Finally, fossil fuels are burnt to generate energy, emitting dangerous pollutants into the atmosphere. As fossil fuels are formed from the buried plants and animals, they are typically carbon-rich complex compounds. When combusted, fossil fuels emit a high amount of CO_2, causing global warming. The average world temperature has risen by ~ 1 degree since the industrial revolution. Global warming is the primary reason for disturbed ecosystems, extreme climates, and catastrophic events like floods, drought, storms, and wildfires. Also, the burning of fossil fuels releases nitrogen oxides into the atmosphere, which causes acid rains and smog and disturbs the natural content of nitrogen in the air. Thus, continuous extraction, transportation, and combustion have wreaked devastation on the environment for many decades. To prevent further impacts of the climate crisis, we must take the transformation actions to phase out fossil fuel utilization entirely and rely on renewable energy sources. The goal is to meet the world's growing energy needs while reducing the hazardous gases' accumulation in the atmosphere.

Renewable energy resources

Renewable energy is generated from natural sources, like the sun, water, and wind. These energy sources are available in abundance on the planet and provide energy in their cleanest form. They are naturally replenishable, thus, are very cost-effective. The natural sources have been in use for several centuries, like wind energy was used to power boats, solar energy was used for lightning. In the present day scenario, the availability of various outstanding and inexpensive technologies to harness nature's power has made renewable energy an integral part of the world energy economy [3, 4, 5]. Solar energy runs photo-voltaic cells convert the energy harnessed from the sun to the electricity that powers the industries and the homes. The solar panels installed on the rooftops provide electricity on a large scale to the entire neighborhood [3]. Windmills located in the open area are used to generate electricity from the rotating turbines' mechanical energy. Wind energy is the most inexpensive renewable energy [6]. Like windmills, hydroelectric power plants are set up to generate the electricity from the mechanical energy of water falling from large dams with very high kinetic energy [7]. Similarly, other natural sources of energy, like biomass energy, which is mostly used in rural areas as a cooking fuel, and geothermal energy drawn by drilling wells into the earth's crust to capture the steaming hot water.

In addition to solar, wind, and water energies, there are natural sources of energy that are abundant in the earth's atmosphere and provide a considerable amount of clean energy. One such example is hydrogen energy. A huge amount of energy can release on combusting molecular hydrogen in the presence of atmospheric oxygen without emitting any hazardous pollutants. Therefore, exploiting hydrogen energy to run vehicles, businesses and industries can prevent the foreseen world energy crisis greatly. [8, 9]

Rechargeable Li-ion batteries are leading energy storage technology used to power a wide range of electronic gadgets, vehicles, and appliances. Li-ion batteries are light-weighted and have a very high energy density. Thus they are an efficient and inexpensive substitute for fossil fuels in the transport industry. Besides, replacing fossil fuels with rechargeable

batteries to fuel vehicles can significantly control air pollution. [10, 11]

Hence, if used for a larger ratio of energy requirements, renewable sources of energy can prevent the foreseen world energy crisis at the same time, can substantially improve the current situation of the planet. However, for a rapid and complete shift of energy resources from fossil fuels to renewable sources, renewable energy technology must be practically implementable. The majority of renewable energy requires superior technology for production and storage.

1.1 Advanced energy materials

Advanced solid-state materials use various smart technologies to harness and utilize energy from renewable sources. They provide efficient and straightforward methods to produce, store and transport the energy to make renewable energy available to a larger population. Hydrogen energy is one of the cleanest forms of energy, and the gravimetric density of the H_2 is exceptionally high. However, hydrogen is not freely available in the atmosphere. It requires to be produced from other molecules like hydrocarbons and water. As soon as hydrogen is generated, it diffuses into the air. Because of the high diffusivity of H_2 molecules, the volumetric energy density is very low. Therefore, hydrogen requires a suitable medium for its storage and transportation. The conventional methods used for its storage include liquefying hydrogen at cryogenic temperatures and storing highly compressed hydrogen gas in high-pressure cylinders. Both the methods are very energy-intensive and pose serious safety concerns. The absence of a straightforward, reversible, safe, and reliable method of storage of hydrogen inhibits its implementation into practical applications. Advanced solid-state materials are a promising medium for the efficient storage and delivery of hydrogen [12]. Scientists have been exploring various materials, including Clathrates [13, 14, 15], metal-organic frameworks [16, 17], complex metal hydrides [18], and many more. The advanced solid-state energy materials enable reversible

hydrogen storage that can release H_2 at ambient environmental conditions and are safe as well as cheap.

The large concentration of CO_2 in the atmosphere leads to extreme climate changes and is dangerous for living beings. It is essential to lower the CO_2 content for the recovery of the planet from the climate crisis. A promising method to reduce the greenhouse gas concentration in the atmosphere is to reduce such gases to form other useful industrial precursors chemically [19, 20]. Many methods can reduce CO_2 to the high-value industrial products, e.g., chemical reduction, photocatalytic reduction, hydrogenation, and electrochemical reduction. Electrochemical reduction of CO_2 to CO is a simple process that can take place in a two-chamber electrolytic cell. The high thermodynamic stability of the CO_2 molecule makes the reduction process impossible to proceed without a suitable electrocatalyst. The cathode material in the electrochemical cell works as an electrocatalyst where the molecule of CO_2 gets adsorbed and forms an intermediate compound, which dissociates from form CO molecule, an essential industrial precursor. The cathode materials working as an electrocatalyst are among the most crucial parts of the electrochemical reduction process [21]. The electrocatalyst is an advanced solid-state material required to exhibit very high Faradaic efficiency and high product selectivity.

The Li-ion batteries are used to power portable electronics like cameras, laptops, mobile phones, and electric vehicles. The Li-ion batteries exhibit the highest value of electrochemical voltage per cell. Therefore, they are a booming technology in the energy storage sector. However, the liquid electrolytes in the cell are volatile materials and are prone to catch fire in case of a short circuit. The safety issues with the current battery designs push scientists to search for an alternative for liquid electrolytes [22]. Inorganic solid-state materials with an electrolyte's characteristics like high ion-mobility, no conduction of electrons, and mechanical stability can replace the liquid electrolytes to eliminate the risk of explosions. Advanced energy materials, e.g., various sulfides and oxides of lithium, have been shown to exhibit ion mobility values very close to the conventional liquid elec-

trolytes. Therefore, such materials can substitute the liquid electrolyte materials without much loss of the current density of the cell and provide significantly improved battery designs with almost no risk of catching fire.

Hence, hydrogen energy, battery energy, and electrochemical reduction of CO_2 are the technologies that provide a reliable and efficient way to fulfill the energy requirements and improve all living beings' environment and health. Advanced solid-state energy materials are promising media that enable the use of such renewable forms of energy and ensure efficiency, sustainability, and safety [23, 22, 24, 25, 26]. In the following sections, we have thoroughly explained the importance of advanced energy materials in the leading technologies, viz. hydrogen storage, electrochemical reduction of CO_2 to CO, and Solid-state Li-ion batteries.

1.2   Hydrogen storage

Hydrogen is very abundant in the earth's atmosphere and a carbon-free source of energy. Therefore, it is considered a potential alternative for the conventional energy sources [23, 27].On combustion, it releases a large amount of energy, and the only byproduct is benign water.

$$H_2 + O_2 \rightarrow Energy + H_2O$$
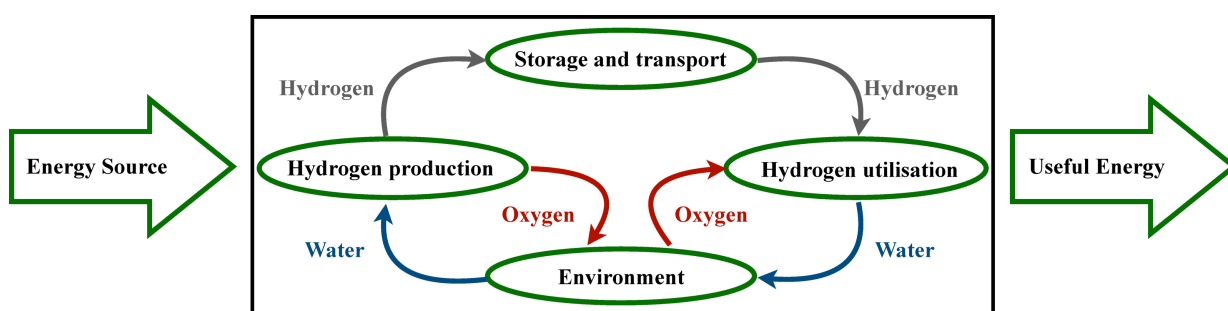
Figure 1.1: Life cycle of the hydrogen gas used as renewable energy

Therefore, it is widely accepted as the cleanest renewable energy that can substitute fossil fuels for many onboard applications in the near future [28, 29, 30, 31, 32, 29, 33, 34, 30].

1.2.1   Challenges in using the hydrogen energy

To use hydrogen energy efficiently, several challenges need to be addressed. First, the cost-effective generation of hydrogen gas at a large scale is required. Currently, hydrogen is mainly produced from feedstocks like fossil fuels, biomass, water, and microorganisms. Water is considered the most promising precursor as it is carbon-free; hence, it has less impact on the environment [35, 36, 37].

After the successful hydrogen generation, the next major challenge is its storage and transportation, as it diffuses into the air as soon as it is produced.

Conventional methods to store hydrogen

Conventionally, hydrogen is stored physically either in liquid or in gaseous form. The liquefication of hydrogen occurs at cryogenic temperatures, whereas the compressed hydrogen gas is stored in very high pressure (350-700 bar) cylinders [38]. The boiling point of hydrogen is $\sim$20 K. Therefore, hydrogen storage in liquid form requires cryogenic temperatures below 20 K. This process is very energy-intensive and practically feasible only for the bulk storage of hydrogen. Hence, it is not suitable for onboard automotive applications. The storage of hydrogen in gaseous form requires very high (350-700 bar) pressure tanks. It is technologically very challenging to compress hydrogen gas to $\sim$700 bars. Further, to ensure safety, such high pressures must be contained in high-strength metal tanks. High-strength steel tanks weigh as much as a hundred times the weight of hydrogen stored. It is impractical to use such heavy tanks for vehicular applications. To make hydrogen energy feasible for mobile applications, the storage medium must be compact, light-weighted, and economical.

Though hydrogen has a high gravimetric energy density, i.e., 120 KJ/g, highest amongst

all known combustible substances, it has a very low volumetric energy density, which is 2700 times less than that of gasoline and 3.2 times less than that of natural gas. Therefore, it is vital to store hydrogen in a way to improve its volumetric energy density.

Storage of hydrogen in solid-state materials

Advanced solid-state materials for the storage and transport of hydrogen have gained much research attention in the recent past. For the practical storage and release of hydrogen, the material must exhibit high gravimetric and volumetric density, reversibility, fast kinetics, and easy release of hydrogen at ambient environmental conditions [23]. Some examples of solid-state materials include metal-organic frameworks [39], clathrates [40], carbon nanotubes [41], metal hydrides [28], and complex metal hydrides [29, 33, 34, 30]. Complex metal hydrides are promising candidate materials because of their high gravimetric density of hydrogen release [42]. Typically complex metal hydrides are the alanates, borohydrides, and amides. Hydrogen is strongly attached via covalent bonding with the Al, B, and N atoms to form complex anions like $[AlH_4]^-$, $[BH_4]^-$, and $[NH_2]^-$. The metal atoms from the group I and II of the periodic table are attached via ionic bonds with these anionic complexes. As hydrogen is strongly bonded with the other atoms in such materials, hydrogen release occurs at relatively higher temperatures with sluggish reaction kinetics. This hinders the realization of complex metal hydrides into practical applications. The reaction kinetics and operating temperature range can be significantly improved in the presence of suitable catalysts [27, 43, 44, 45, 46, 47, 48, 49]. The extensive research effort is dedicated to finding the appropriate catalysts for various complex metal hydride materials.

1.2.2 Significant research done in past

In 1997, B.Bogdanovic et al. showed that the catalytic effects of transition metal dopants could lower the dissociation temperature significantly and enhance the reaction kinetics

drastically[27]. A lot of experimental[50, 43, 51, 45, 52] and theoretical[44, 53, 47] work has been done to understand the mechanism of desorption of hydrogen from doped $NaAlH_4$. Jorge Iniguez et al.[43] showed that Ti atom could accommodate many hydrogen atoms in its vicinity, due to which the presence of Ti atoms in $NaAlH_4$ facilitates the softening and breaking of the bond between Al and H and hence, release of H_2. Also, they showed a possibility of Ti atoms dragging extra hydrogen atoms into the system, which may be a reason for improved H-storage capacity. Ti atoms in a particular local environment have been shown to be responsible for catalyzing the rehydrogenation in $NaAlH_4$ by Santanu Chaudhary and James T Muckerman[44] where they showed that the local environment of catalytic atoms plays an important role in rehydrogenation reactions. W. Lohstroh and M. Fichtner suggested that diffusion of heavier species such as Al_xH_y or NaH seems to be rate-limiting factors in dehydrogenation $NaAlH_4$ to Na_3AlH_6[45]. Hydrogen release and uptake are accompanied by long-range diffusion of metal species. The study of Hakan Gunaydin[53] suggested that bulk diffusion of Al species is the rate-limiting step in the dehydrogenation of Ti-doped samples of $NaAlH_4$. Gareth B. Wilson-Short et al.[47] proposed a specific mechanism for the process of diffusion and decomposition. They suggested that charged defects play a crucial in this process. The charge carriers provided by hydrogen-related defects aid the diffusion of Na- and Al-related defects. The role of hydrogen-related defects in the dehydrogenation of catalyzed $NaAlH_4$ was studied by Amra Peles and Chris G. Van de Walle in 2007[49]. It was suggested that transition metal dopants such as Ti, Zr may play an electronically active impurity role, promoting the diffusion of hydrogen.

1.3   Electrochemical reduction of CO_2

Because of the continuous exploitation of fossil fuels for about a century, greenhouse gases, e.g., CO_2, are accumulated in the atmosphere. The increased content of CO_2 in

the atmosphere is the main reason behind extreme weather events like floods, drought, forest fires, rising sea levels, and glacier melting. The concentration of CO_2 in the air for the year 2020 is 411.29 ppm (parts per million), whereas the suggested safe level ranges between 200-350 ppm.

One effective way to alleviate the effects of CO_2 is the chemical reduction of CO_2 to form other critical industrial precursors [54]. The chemical reduction of CO_2 is a widely accepted approach because it reduces the content of CO_2 in the atmosphere while also helping in the synthesis of high valued chemicals and fuels; hence, it is a path toward sustainable development [54, 55, 56, 57]. Reducing CO_2 through electrochemical reduction (ECR) has several advantages. First, the reaction rates are high and can be tuned. They exhibit high efficiency and use non-toxic electrolyte materials. Besides, they can efficiently run on renewable energy sources, i.e., hydroelectricity, solar energy, and wind energy [19, 20, 58, 59]. Due to the high thermodynamic stability of the CO_2 molecules,
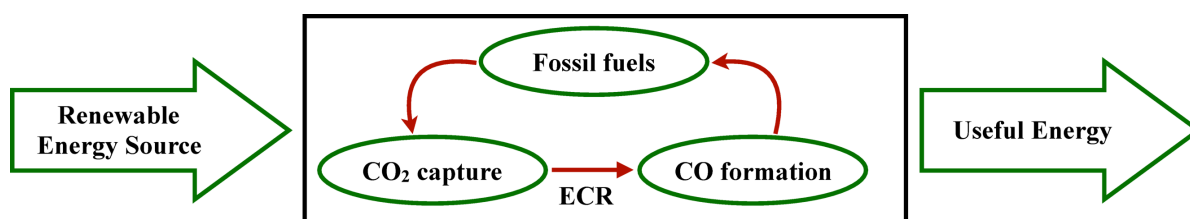
Figure 1.2: Life cycle of CO_2 on recycling

the reduction process is kinetically very sluggish and almost impossible without a suitable electrocatalyst. The final product of an electrochemical reduction reaction depends highly on the electrocatalyst's choice and the electrode potential. The ECR of CO_2 to CO usually occurs via the three-step process on the electrocatalyst's surface as a cathode material [21, 60].

1.3.1   Mechanism of ECR in the presence of an electrocatalyst

First, the linear CO_2 molecule is adsorbed on the surface of the cathode, gains an electron from the cathode, and bends:

$CO_2 + e^- \rightarrow CO_2{}^*$
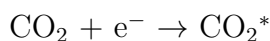
Then, it accepts one proton to form an activated compound, $COOH^*$:

$CO_2{}^* + H^+ + Energy \rightarrow COOH^*$

This step is the energy-intensive step and is considered the rate-limiting step for the ECR process.

Next, the C-O bond dissociates, and CO gas is desorbed from the surface of the cathode:

$COOH^* \rightarrow CO + H_2O + Energy$
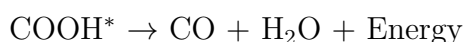
1.3.2   Main challenges

The reduction potential of the above reactions is similar to that of the hydrogen evolution reaction (HER). Therefore, ECR of CO_2 to CO and HER are competitive reactions. Thus, the electrocatalyst must exhibit very high product selectivity to suppress competitive HER. The other main challenge of the process is the requirement of very high overpotential, which limits their commercialization. The electrocatalyst should be chosen judiciously to ensure high product selectivity, high Faradaic efficiency, and improved reaction kinetics at lowered overpotential values.

1.3.3   Significant research done in past

Intensive research on developing and realizing the suitable electrocatalyst has been done since 1980 [61, 62, 63, 64, 65, 21, 60]. Because of low cost and high selectivity of the Cu-based electrocatalysts, they have attracted scientists' attention in the recent past [20]. However, Cu-based electrocatalysts exhibit a rather higher values of overpotentials leading to poor Faradaic efficiencies. A significant research has been dedicated in the regard

of improving the Faradaic efficiency these materials. It has been suggested that bimetallic alloys of Cu with other metallic elements like Pd [64], In [63] can enhance the Faradaic efficiency of formation of CO from reduction of CO_2. Also, using various compositions of metals in bimetallic Cu-Sn [66] and Cu-Au [67] alloys leads to high Faradaic efficiencies. The presence of In-atoms in the elctrocatalystst has been reported to supress the competitive hydrogen evolution reaction in many recent studies [68, 21, 60]. On the other hand, the presence of point defects like oxygen vacancies are found to significantly increase the value of Faradaic efficiency [69]. The presence of oxygen vacancy defects facilitates the adsorption of CO_2 on the surface of In_2O_3 and Ga_2O_3 catalysts with a decrease in the adsorption energy calculated in DFT studies [70]. In another study, it is found that increasing the concentration of oxygen vacancies in Co_3O_4 increases the product selectivity of the catalyst to 85% [71].

1.4 Rechargeable Battery

A battery is an energy storage device that converts the stored chemical energy into electrical energy. A battery is composed of more than one electrochemical cell. A typical electrochemical cell's basic construction idea involves two electrode materials at different chemical potentials separated by an ion conductor, called the electrolyte. The energy is stored in the form of a difference in chemical potentials of the electrode materials. Electrons flow from one electrode to the other through the external circuit when connected to an external circuit. The ions move in the opposite direction through the electrolyte. The average voltage generated by an electrochemical cell ranges from 1.0 V to 3.6 V, depending on its chemistry.
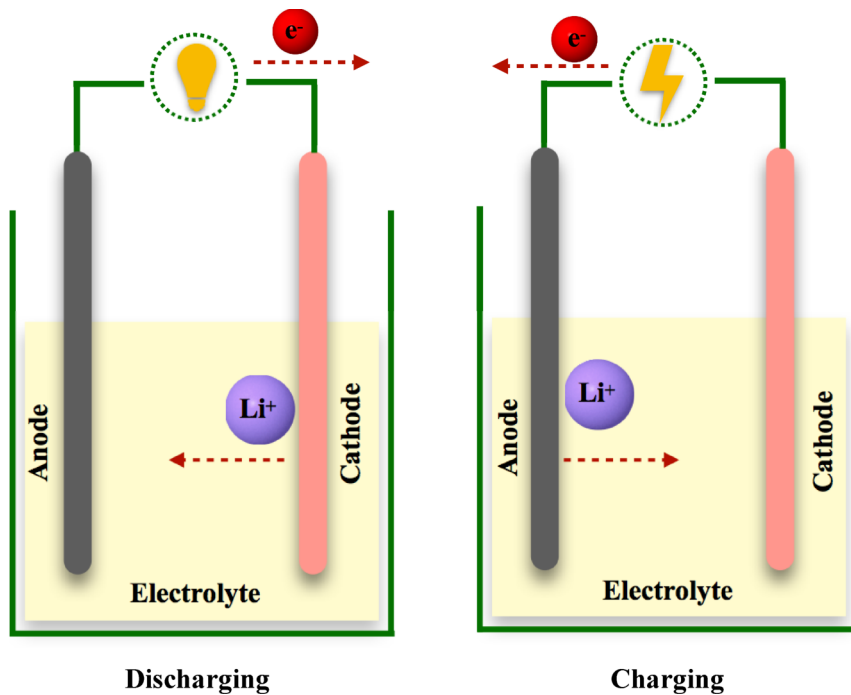
Figure 1.3: Charging and discharging mechanism of Li-ion battery

1.4.1   History of batteries

The term "battery" was first used in 1749 by an American scientist, Benjamin Frankin, when he generated electricity from a set of connected capacitors. However, the actual battery was invented by an Italian physicist, Alessandro Volta, in 1800 using copper, zinc, and saltwater [72]. The first rechargeable battery was invented in 1859 by a French physicist, Gaston Plante, commonly known as a lead-acid battery [73]. Lead-acid battery exhibits an average cell voltage of 2.1 V and is still prevailing, is commonly used in ignition start of cars. Another remarkable invention in rechargeable batteries occurred in 1899 when Walder Jungner invented the Nickel-Cadmium battery using Cd as the negative electrode and NiOOH as the positive electrode material separated by an alkaline solution [74]. It was first commercialized in 1960. NiMH (Nickel-metal hydride) batteries were first designed and mass-produced in 1980, following which the use of portable electronic devices, such as mobile phones, cameras, and notebook computers, significantly increased. The

average voltage of a NiMH cell is 2.1 V. The work on developing high-density Li-ion batteries was started by Stanley Whittingham in the late 1970s. He used high energy density electrodes, viz. lithium(Li) and titanium disulfide(TiS_2) [75]. However, this combination of electrodes posed severe safety concerns. Continued research for about two decades by three Nobel laureates, viz., Stanley Whittingham, John Bannister Goodenough, and Akira Yoshino led to the development of high energy density rechargeable Li-ion batteries [76].

The properties of lithium, i.e., light-weight and high electrochemical potential, make the Li-ion batteries the most promising battery technology with the highest cell voltage of 3.6 V achieved for a single cell so far [77, 78]. Li-ion batteries have a high energy density, i.e., approximately two times that of Ni-based batteries. Besides high cell voltage and high energy density, Li-ion batteries have several advantages: low maintenance, less self-discharge, and no memory. All these advantages of Li-ion batteries make them suitable for a wide range of applications, from portable electronics to electric vehicles.

1.4.2   Main challenges

Though the number of electric vehicles is rapidly increasing globally, several issues need to be addressed for the full-fledged uptake of battery vehicles. The first major issue with conventional Li-ion batteries is safety. The organic liquid electrolyte being flammable poses the risk of thermal runaway and explosion in a short circuit [79, 22]. There is a tradeoff between the capacity of the battery and the safety. Therefore, the current electric vehicles have a short driving range of 50-100 miles on a single charge. Other limitations of conventional Li-ion batteries include higher cost, sensitivity for extreme temperature, less specific energy, and short cycling life.

1.4.3   Solid-state batteries

All-solid-state batteries are a promising alternative to conventional batteries [80]. An All-solid-state battery consists of a solid electrolyte along with solid electrodes. The solid electrolyte material is not flammable, hence, eliminates the risk of thermal runaway. All-solid-state batteries exhibit tremendously improved thermal stability and electrochemical stability. Improved electrochemical stability enables high-density Li-metal cathodes; thus, it helps achieve high energy density. It makes the battery design simpler and more compact, hence, lowers the overall cost of manufacturing and packaging [81, 82]. Solid-state batteries have attracted tremendous research efforts in the recent past. The inorganic materials suitable for electrolytic applications can be majorly categorized into oxides and sulfides. Some common examples of prototypical materials being studied include Li_2S-P_2S_5 systems, $Li_7La_3Zr_2O_{12}$, Li_4GeS_4, Li_3PO_4, etc. However, there are several challenges in employing a solid material as an electrolyte in the battery. Solids are not as good ionic conductors as liquids. Therefore, achieving good ionic conductivity in the solid electrolyte material is the biggest challenge. Besides, the mechanical strength of a material plays a vital role in determining the material's applicability. The electrode materials expand and contract while cycling due to intercalation and deintercalation of Li-ion. The solid electrolyte material must maintain physical contact with the electrodes to maintain the battery's proper functioning. The solid electrolyte material must be ductile enough to prevent fracturing during cycling while avoiding the formation of dendrites that causes capacity fading [83, 84, 85, 86, 87, 88, 89]. Therefore, achieving appropriate mechanical properties in the material is a significant challenge. In addition to being a reasonably good ion conductor and mechanically appropriate, the solid electrolyte material must be electrochemically stable against the high-density metallic electrodes. Scientists have been trying to tune these properties of several candidate materials using various means. Inducing crystal defects is one such proven way to achieve the desired characteristics in the materials.

1.4.4   Significant research done in past

The development of highly conductive solid-state electrolytes (SSE) is one prerequisite for realizing their applicability. Recent discoveries in ultrafast solid Li-ion conductors that exhibit ion-mobility comparable to the conventional organic liquid electrolytes have led to many research interests in this field [90, 91, 92]. Most of the recent research has been focused on oxide as well as sulfide materials. Both of them have their advantages and disadvantages. Sulfide SSEs exhibit higher ionic conductivity, which is probably due to the higher polarizability of sulfide ions. However, they are hygroscopic and form toxic H_2S when exposed to moisture. On the other hand, oxide materials show good electrochemical and chemical stability. However, they have very low ionic conductivity at room temperature [93].

In the recent past, many studies have been carried out to find out the descriptors for ionic conductivity in various materials like LISICON [94, 95, 96], NASICON [97], perovskites [98], etc. It has been suggested that ionic conductivity can be enhanced if the lattice volume is increased in many materials [95, 97, 98, 99]. It has also been reported that replacing the anions in the structure by moving down in a group in the periodic table may decrease the activation energy, thereby increasing the ionic conductivity [95, 100, 101]. Recently, Sokseiha Muy et al. [102] have shown that high ionic conductivity is related to ions' large thermal displacement amplitude. They suggested that large amplitudes correspond to the soft atomic potentials, which in turn are associated with the low frequency of vibrations [103, 104]. Hence, large amplitudes of vibration and low frequency of vibration may lead to high ionic conductivity.

In addition to high Li-ion conductivity, adequate elastic properties are essential prerequisites for an SSE to be viable [86]. During charging and discharging of a battery, Li-ions intercalate into and out of electrodes. This leads to cyclic volumetric expansion and contraction of the electrodes. It has been reported that metallic electrodes exhibit a chemical strain of up to 10% during electrochemical cycling. The strain can cause fragmentation

of electrode materials. This leads to the formation of dendrites. The dendritic formation is responsible for the mechanical degradation of the cell and affects its durability. It is suggested that the elastic moduli of an SSE significantly influences the formation and propagation of dendrites during cycling. According to linear elasticity theory, the shear modulus, G of the electrolyte must be greater than twice the shear modulus of Li atom to suppress the dendritic formation [83]. In addition to this, SSE should deform elastically to maintain physical contact with the electrodes during cycling. A softer material may be an easier SSE to achieve better contact with electrodes. The stiffness of a solid material can be determined from Young's modulus of elasticity, E. It is a function of bond dissociation enthalpy per unit volume [84, 105]. The bond energy between Li and S in sulfide SSEs is lower than that in oxides. Therefore, sulfides are softer and exhibit a lower value of Young's modulus, hence, less tendency towards fracturing. The reported values of Young's modulus of elasticity of various oxide SSEs are in the range 150 GPa [85, 86, 87, 88, 89] whereas, the values for Li_2S-P_2S_5 glasses have been reported to be in the range 18-25 GPa[106].

With the advent of high-speed computing facilities like high-performance computers (HPC), computational materials science has emerged as a potential research field. A wide range of properties from the fundamental ground state energies to the excited state properties can be calculated at low cost and within less time frame than experimental studies. This is a promising medium to provide a theoretical guide to the experiments. Computational studies are the best alternatives for experiments in extreme environmental conditions.

1.5   Objectives of the thesis

The thesis aims at understanding and investigating the role of crystal defects on various properties of advanced energy materials. Our methodology includes First-principles study within the framework of state-of-the-art density functional theory (DFT) plus the well-

established methodologies of *ab-initio* thermodynamics and molecular dynamics (AIMD). Firstly, we describe the role of charged hydrogen-related defects in the dehydrogenation mechanism of $NaAlH_4$, a prototypical hydrogen storage material. We investigate the effect of temperature and pressure on various charged defects' relative stability. Additionally, we show that transition-metal (TM) atom dopants facilitate the dehydrogenation reactions in such materials. We explain the selection of the most suitable TM dopants to improve the reaction kinetics in $NaAlH_4$.

Secondly, we explain the mechanism of electrochemical reduction of CO_2 to CO on the surface of an electrocatalyst. We investigate the role of oxygen vacancies in Cu-In-O nanocomposites in enhancing the catalytic activity of the electrocatalyst. Further, we show the role of In-atoms in improving the product selectivity of the catalyst.

Thirdly, we explain the importance of solid-state electrolyte materials in Li-ion batteries. We study the elastic properties of various sulfide materials to determine the mechanical stability of the candidate electrolyte materials. We also explain the role of halide doping in improving the mechanical properties of the materials. Then, we select the best-suited material among various sulfide materials based on the diffusional properties. We elucidate the role of Li-vacancies in enhancing the ion mobility through the bulk materials.

The main objective of the thesis is :

1. To elucidate the role of temperature and pressure on the relative stability and concentration of the intrinsic defects in the bulk $NaAlH_4$.

2. To select the best-suited transition metal atom dopant for enhancing the hydrogen desorption kinetics in $NaAlH_4$.

3. To investigate the role of oxygen vacancy defects in the Cu-In-O nanocomposites for enhancing the catalytic activity of the material.

4. To understand the role of In-atom in the Cu-In-O nanocomposites in improving the product selectivity.

5. To determine the mechanical stability of various candidate solid-state electrolyte ma-

terials and to study the effect of halide doping on the mechanical properties of such materials.

6. To select the best candidate material for the application of solid electrolyte based on Li-ion diffusivity values through the bulk materials.

7. To investigate the role of lithium vacancy defects in enhancing the diffusion of ions through such materials.

1.6   Organisation of the thesis

The thesis is organized in the following six chapters:

In chapter 1, a brief introduction to advanced energy materials has been discussed.

In chapter 2, various computational methodologies, including density functional theory (DFT), *ab initio* thermodynamics, genetic algorithm (GA), and molecular dynamics (MD) are broadly explained.

Chapter 3 explains the role of charged defects in the dehydrogenation of $NaAlH_4$ at realistic environmental conditions. $NaAlH_4$ is a complex metal hydride studied as a prototypical system for hydrogen storage applications for the last few decades. Complex metal hydrides seem to have a promising future in the hydrogen storage industry because of their straightforward hydrogen release under achievable environmental conditions. They exhibit high gravimetric and volumetric energy densities. However, because of the relatively high thermodynamic stability of $[AlH_4]^-$ units, the release of hydrogen is possible only in the presence of an appropriate catalyst. The hydrogen release mechanism from the complex metal hydrides includes self-diffusion of charged hydrogen-related defects, i.e., hydrogen vacancy defects and interstitial hydrogen defects. The self-diffusion of a defect through the bulk material depends on the thermodynamic stability of the defect configuration. In the theoretical studies, we estimate the stability of a defect from the defects' formation energy. However, the formation energy calculations performed at the DFT level

do not give any insights into the defect stability at finite temperature conditions. As the material is usually operational at room temperatures or moderately higher temperatures, it is essential to understand the hydrogen desorption mechanism at realistic environmental conditions. We have included the effects of temperature and partial pressure of hydrogen with the help of *ab-inito* thermodynamics on top of DFT calculations. We observe that the most stable defect states estimated from the DFT alone are no longer the stable defect states on the inclusion of temperature and pressure terms in the formation energy calculations. Thus, it is very crucial to incorporate the effects of temperature and pressure while determining the stability of intrinsic defects in such materials at the experimental conditions. Further, in this chapter, we describe the role of transition metal atom dopants in improving the reaction kinetics and the required environmental conditions for the release of hydrogen from $NaAlH_4$. TM atoms have partially filled d-orbitals. That is why they tend to make as many bonds with other atoms as possible. They attract the hydrogen atoms from the $[AlH_4]^-$ units and slightly distort the geometry of the alanates, loosening the strong Al-H bonds. Therefore, the presence of TM atoms in the system makes hydrogen release possible at ambient environmental conditions. As earlier mentioned, the dehydrogenation mechanism involves the self-diffusion of the charged H-related defects. The TM atom dopants shift the Fermi energy level that affects the stability of these H-related defects; hence, the self-diffusion of these defects is altered. The selection of the best suitable TM atom dopant is made based on the two factors discussed above. The more a TM atom distorts the geometry and increases the stability of the intrinsic defects, the more suitable it is considered for the catalytic applications in such materials.

Chapter 4 describes the role of point defects, i.e., oxygen-vacancy, in the activation of electrocatalysts used in the electrochemical reduction of CO_2 to CO. The increased content of CO_2 in the atmosphere is the leading cause of climate change, resulting in catastrophic events like floods, drought, glacier melting, and many more. On the other hand, CO is an important industrial feedstock that can be used to synthesize high-value chemicals,

including fuels. Therefore, the conversion of CO_2 to CO through the electrochemical reduction (ECR) process reduces the concentration of the CO_2 in the atmosphere while also producing high-value industrial feedstocks. ECR is carried out in an electrochemical cell with the cathode material acting as an electrocatalyst. The electrocatalyst is required to exhibit high values of Faradaic efficiency as well as high product selectivity. Experimentally synthesized Cu-In-O nanocomposites show exceptionally high values of Faradaic efficiency. We study the mechanism of ECR in the proposed nanocomposites with the help of our DFT calculations. We model the system with the cascade genetic algorithm (cGA) technique to depict the experimentally synthesized nanocomposite. ECR proceeds with a two-step process. Firstly, CO_2 is adsorbed at the electrocatalyst's surface and gets reduced to an activated intermediate compound $COOH^*$. The first step is endothermic and determines the ease of the whole process. Secondly, $COOH^*$ dissociates into CO and H_2O with the release of energy. The second step is a spontaneous process. We determine the favorable site for the ECR process by adsorbing the COOH group and H-atom at various sites in the modeled cluster. We observe that the spontaneous dissociation of COOH to form CO and H_2O occurs only at the site closer to oxygen-vacancy. Further, we calculate the reaction enthalpy of the first step in the clusters with different oxygen vacancy concentrations. We show that by increasing the concentration of oxygen vacancy defects in the system, the reaction enthalpy of the endothermic step decreases. Therefore, we can infer that the proposed Cu-In-O nanocomposites' catalytic activity is mainly due to the oxygen-vacancies in the system. Further, we validate the role of In-atoms in improving the electrocatalyst product selectivity by the suppression of the hydrogen evolution at the In-site.

Chapter 5 describes the mechanical and diffusional properties of various sulfide materials for the application of solid-state electrolytes in Li-ion batteries. Li-ion batteries are used in a wide range of applications. However, the liquid electrolyte materials pose a serious risk of catching fire and exploding. Therefore, solid-state electrolyte materials have been

considered for replacing the liquid electrolytes. Solid-state electrolyte materials eliminate the risk of explosion and compact the battery design, such that the all-solid-state batteries can be used in onboard vehicular applications. However, a candidate solid-state material must exhibit high mechanical stability and high Li-ion diffusivity. We determine the mechanical stability of various candidate materials by calculating the elastic properties from the DFT calculations. We calculate the elastic moduli like bulk modulus (B), Young's modulus (E), and shear modulus (G) of elasticity with the help of elastic coefficients determined directly from the stress-strain relation. Then, the mechanical stability of the materials is estimated from Pugh's criterion of ductility. According to Pugh's criterion, the ductility of a material can be determined from the ratio of bulk modulus to shear modulus of elasticity, i.e., the value of B/G ratio. If the B/G ratio is greater than 1.75, the materials are considered ductile, thus, mechanically stable for the application of solid-state electrolyte, whereas, if the B/G ratio is less than 1.75, the material is brittle and not suitable for electrolytic applications. We determine the ductility of all the considered materials from the above-stated rule and observe that the sulfide materials are ductile, hence, mechanically appropriate for the electrolytic applications. Further, we investigate the role of halide-doping by doping Cl, Br, and I-atoms in the bulk materials. The halide doping enhances the mechanical properties of such materials attributed to the high electron-affinity of the dopant atoms that softens the Li-S bonds in the materials, thus increasing the value of B. Following this, we calculate the diffusional properties of such materials at various temperatures with the help of *ab-initio* molecular dynamics (AIMD) simulations. Various diffusional properties calculated include tracer diffusivity and conductivity, jump diffusivity, the density of mobile Li-ions, and jump-diffusion pathways. A thorough investigation of the Li-ions' diffusional pathways leads to the selection of the best-suited candidate material. Finally, we elucidate the role of lithium vacancy defects in bulk materials. We find out that the vacancy defects provide more vacant lattice sites for the Li-ions to transport from one end to the other end of the cell by hopping among

the lattice sites. Therefore, inducing Li-vacancy defects in the bulk materials enhances the Li-ion conductivity.

In chapter 6, the results discussed in the previous chapters are summarised.

Chapter 2

Theoretical methodology

2.1 First principles calculations

First-principles calculations are based on the interaction among the fundamental particles, viz., electrons ad nuclei, that make up the whole matter. The basic equations for electrons and nuclei are the stepping stones for determining a wide range of the condensed matter system's properties [107]. The accurate understanding and application of such interactions lead to predicting the relevant system's behavior under various experimental conditions, thus helping solve various critical problems of materials science.

2.2 many-body problem

In the first-principles approach, the matter is defined by the arrangement of its constituent elementary particles, i.e., electrons and nuclei. Therefore, the quantum mechanical treatment of the matter includes solving many-body Scrödinger's equation:

$$H\Psi = E\Psi \tag{2.1}$$

Here, H is the many-body hamiltonian, Ψ is the wavefunction, whereas E denotes the total energy of the system. The many-body hamiltonian for a system of electrons and nuclei consists of terms representing kinetic energies of all the electrons as well as the nuclei, potential energies of interaction among electrons, nuclei, and electron-nuclei interactions. The many-body hamiltonian can be written as follows [107]:

$$H = -\frac{\hbar^2}{2m}\sum_i \nabla_i^2 - \sum_{i,I}\frac{Z_I e^2}{|r_i - R_I|} + \frac{1}{2}\sum_{i,j}\frac{e^2}{|r_i - r_j|} - \sum_I \frac{\hbar^2}{2M_I}\nabla_I^2 + \frac{1}{2}\sum_{I,J}\frac{Z_I Z_J e^2}{|R_I - R_J|} \quad (2.2)$$

Here, m is the mass of an electron, and M denotes the mass of the nucleus. i and j denote the indices for electrons whereas the upper case letters I and J denote the indices for nuclei. r and R respectively represent the positions for electrons and nuclei. Z denotes the atomic number. In eq.2, the first term represents the total kinetic energy of all the electrons in the system; the second term represents the interaction energy of electrons and nuclei, whereas the third term denotes the energy of interaction among electrons, and the fourth and fifth terms respectively denote the kinetic energy and interaction energy of the nuclei.

2.2.1   Born Oppenheimer approximation

The mass of a proton is 1836 times that of an electron. Therefore, we can say that nuclei are much heavier than electrons, and the mass of nuclei can be assumed to be infinite compared to the electrons. The time scale of motion of electrons are nuclei are distinct. Hence, the motion of electrons and nuclei can be treated separately [108]. While considering the energy of electrons, the nuclei can be assumed to be stationary, i.e., nuclei's kinetic energy is neglected. Therefore, the fourth term in Eq. 2.2 can be approximated to zero. While the fifth term can be added as a constant term. The Eq. 2.2 is thus, reduced to the hamiltonian for electrons:

$$\hat{H} = -\frac{\hbar^2}{2m} \sum_i \nabla_i^2 - \sum_{i,I} \frac{Z_I e^2}{|r_i - R_I|} + \frac{1}{2} \sum_{i,j} \frac{e^2}{|r_i - r_j|} + E_{II} \tag{2.3}$$

Thus, the theoretical explanation of various phenomena in condensed matter physics ultimately emerges from the theory of electrons. Comprehensive knowledge of a system's electronic structure leads to predicting a wide range of ground-state and excited-state properties with much accuracy. The electronic ground state aids in determining numerous properties like charge density, cohesive energy, elastic constants, phase transition. At the same time, excited states of electrons determine specific heat, optical properties, spectra. The ground state of the electron is a vital part of the electronic structure. It plays a crucial role in determining the spatial arrangement of nuclei in the many-body interacting systems, thus predicting the matter's structure.

The first term in Eq. 2.3 is the total kinetic energy of the electrons. It is usually denoted by $\hat{T}$. The second term represents the potential due to the set of nuclei in the system, which is generally termed as the external potential, $\hat{V}_{ext}$. The third term is the Coulombic potential among the electrons. It is also known as Hartree potential, $V_{Hartree}$. The last term denotes the potential among nuclei. It is simply a classical additive term in the electronic ground state calculations. Therefore, the hamiltonian for an interacting system of many electrons can be written in simplest form as:

$$\hat{H} = \hat{T} + \hat{V}_{ext}(r) + \hat{V}_{Hartree} + E_{II} \tag{2.4}$$

Now, the total energy of the system can be obtained from the expectation value of the above written hamiltonian.

$$E = <\hat{H}> = \frac{<\Psi|\hat{H}|\Psi>}{<\Psi|\Psi>} \tag{2.5}$$

2.2.2   Independent electron approximation

Basically, there are two independent particle approximations, viz., "noninteracting" and "Hartree-Fock" [109] approximations. Both the approximations neglect any type of correlation among the electrons. However, the electrons follow the well known Pauli's exclusion principle. In the noninteracting approximation, the electrons are considered to be under the influence of an effective potential. In noninteracting approximation, the Schrödinger's equation for an electron can be written as:

$$\hat{H}_{\text{eff}}\psi_i = \left(-\frac{\hbar^2}{2m}\nabla_i^2 + \hat{V}_{\text{eff}}(r)\right)\psi_i(r)$$
$$= \epsilon_i\psi_i(r) \tag{2.6}$$

Here, $\psi_i(r)$ denotes the wavefunction corresponding to an electron positioned at r, and $V_{\text{eff}}(r)$ is the effective potential acting on the electron. $V_{\text{eff}}(r)$ is a function of position of the electron, r. ϵ_i is the energy of the electron.

Whereas, in the Hartree-Fock approximation, the electrons are assumed to be moving under the effect of Coulombic interactions. Here the wavefunction, $\Psi(r)$ for N electrons, is represented by an N × N antisymmetrized determinant of electronic orbitals ($\phi(r)$), known as Slater determinant, as shown below [109]:

$$\Psi(r_1, r_2, \ldots, r_N) = \frac{1}{\sqrt{N!}}\begin{vmatrix} \phi_1(r_1) & \phi_2(r_1) & \ldots & \phi_N(r_1) \\ \phi_1(r_2) & \phi_2(r_2) & \ldots & \phi_N(r_2) \\ \vdots & \vdots & \ldots & \vdots \\ \phi_1(r_N) & \phi_2(r_N) & \ldots & \phi_N(r_N) \end{vmatrix} \tag{2.7}$$

Hartree Fock method involves the minimization of energy with respect to the parameters included in the wavefunction. Though the Hartree-Fock method is successfully applied in the energy and wavefunction prediction of atoms and molecules and nuclear physics, it has certain limitations. The first limitation lies in the fundamental assumption of the

method that the electrons are uncorrelated. However, the electron-electron correlation energy is a crucial term in accurately determining the energy of the system. The other important issue is that, for an N electrons system, the Hartree-Fock method requires to solve a set of 3N Schrödinger's equations. Solving such a large number of equations is computationally very expensive and time-consuming. Therefore, there is a need for a robust theory that can include the effect of electron-electron correlation, simultaneously can reduce the computational cost and time.

2.3   Density functional theory

Within the domain of first-principles calculations, density functional theory (DFT) is one widely accepted and well-established method to solve the many-body problem in condensed matter physics. The theory provides vigorous methods to adequately incorporate the electron-electron correlations in the independent-particle approach for a many-body interacting system. Density functional theory is based on the precept that electrons' ground state density largely governs the state of a system. The density of electrons, which is a function of position, $n_0(r)$ determines the many-body interacting system's wavefunction. Therefore, all the system properties, including ground state and excited properties, can be assessed as functionals of $n_0(r)$. Figure 2.1 represents a scematic diagram showing the basic idea of density functional theory, where the interactions among electrons and nuclei are replaced with an electron density.

The theory is based on two theorems given by Hohenberg and Kohn in 1964 [110].
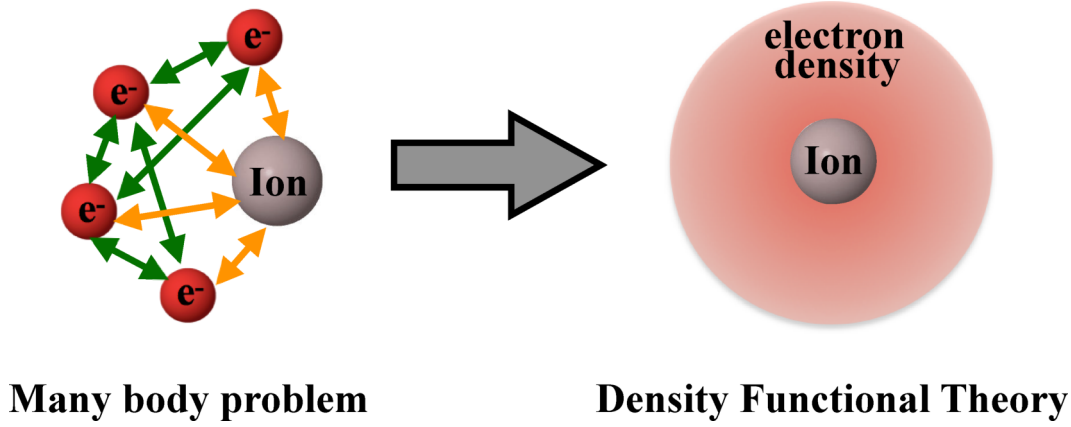
Figure 2.1: The individual interactions among electrons and nuclei is replaced with overall electron density in density functional theory.

2.3.1   Hohenberg-Kohn Theorem

The formulation of Hohenberg and Kohn is relevant to any many-body interacting system of electrons in the external potential $V_{ext}(r)$, where the hamiltonian can be expressed as:

$$\hat{H} = -\frac{\hbar^2}{2m} \sum_i \nabla_i^2 + \sum_i V_{ext}(r) + \frac{1}{2} \sum_{i,j} \frac{e^2}{|r_i - r_j|} \tag{2.8}$$

The two theorems given by Hohenberg and Kohn can be explained like this. First, the ground state particle density $n_0(r)$ of an interacting system uniquely determines the external potential $V_{ext}(r)$, which determines the complete hamiltonian of the system written in Eq. 2.8. Putting this hamiltonian in Schrödinger's equation, one can find the ground state wavefunction, thus finding out the wavefunction for all the system's states. Therefore, all the ground state and excited-state properties of the many-particle interacting system can be calculated from the ground state particle density. Second, the exact ground state density produces the global minimum of the energy functional. The exact ground state density of a system can be obtained by minimizing the energy functional E[n] [107, 110]. The total ground state energy functional can be written as:
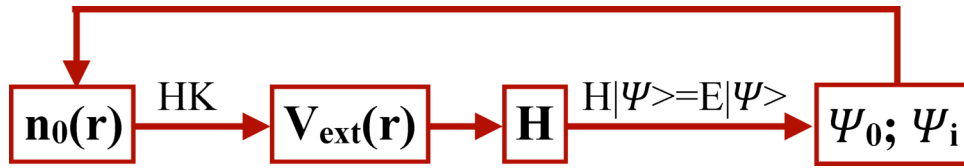
Figure 2.2: schematic diagram to explain Hohenberg-Kohn theorems.

$$E[n] = T[n] + E_{\text{int}}[n] + \int dr^3 V_{\text{ext}}(r)n_0(r) + E_{II} \tag{2.9}$$

Here, $T[n]$ and E_{int} are respectively the kinetic energy and inetraction potential energy of the electrons. These two terms depend only on the density of electrons, thus are called universal functional of density. The kinetic energy and potential of electrons can be grouped into a universal functional of density:

$$F_{\text{HK}}[n] = T[n] + E_{\text{int}}[n] \tag{2.10}$$

The total energy can now be written as:

$$E[n] = F_{\text{HK}}[n] + \int dr^3 V_{\text{ext}}(r)n_0(r) + E_{II} \tag{2.11}$$

Though Hohenberg-Kohn theorem simplifies the problem of many-particle interacting systems to a great extent, it does not provide any insights into the nature of the functional $F_{\text{HK}}[n]$. There is no known method to formulate the direct dependence of kinetic energy on the density.

2.3.2   Kohn-Sham DFT

Kohn-Sham's approach to density functional theory solves this problem by replacing the actual system of interacting particles with an auxiliary system of noninteracting particles [111]. The kinetic energy is thus, calculated exactly from the individual electron wavefunctions. However, the interaction energy terms can be written as explicit functionals of

the density. Electronic orbitals govern the kinetic energy of independent electrons instead
of density. Therefore, it is possible to determine all those properties of the system that
have no direct relation to the density, such as the metallic and nonmetallic behavior of
the matter. Thus, Kohn-Sham DFT provides a robust method to calculate the electronic
structure of a many-particle interacting system, thereby determining all the ground state
and excited state properties.

Auxiliary system: The auxiliary system of noninteracting electrons is modeled such that
it has the same ground-state density as that of the original interacting system. There is
no interaction among the electrons. Each electron is assumed to be under the influence of
a local effective potential $V_{\text{eff}}(r)$. The hamiltonian of the auxiliary system can be written
as [111, 107]:

$$\hat{H}_{\text{aux}} = \hat{T}_{\text{aux}} + \hat{V}_{\text{eff}}(r) \qquad (2.12)$$

Here, $\hat{T}_{\text{aux}}$ represents the kinetic energy operator of electrons in the auxiliary system:

$$
\begin{aligned}
T_{\text{aux}} &= -\frac{1}{2} \sum_{i=1}^{N} <\psi_i|\nabla^2|\psi_i> \\
&= -\frac{1}{2} \sum_{i=1}^{N} \int d^3 r (\nabla \psi_i)^2
\end{aligned}
\qquad (2.13)
$$

Here, N is the total number of electrons and ψ_i denotes the wavefunction of an electron.
In the Kohn-Sham approach, the total energy of the many-body interacting system of
electrons can be written as [111, 107]:

$$
\begin{aligned}
E_{\text{KS}} = &-\frac{1}{2} \sum_{i=1}^{N} \int d^3 r (\nabla \psi_i)^2 + \int d^3 r V_{\text{ext}}(r) n(r) \\
&+ \frac{1}{2} \int d^3 r d^3 r' \frac{n(r) n(r')}{|r - r'|} + E_{II} + E_{xc}
\end{aligned}
\qquad (2.14)
$$

Here, the first term is the total kinetic energy of the electrons, which is written as an explicit function of electronic orbitals. The second term represents the potential energy due to the external potential from nuclei in the system. The third term is the Coulombic interaction among the electrons. This is the self interaction energy of density of electrons with itself. It is often termed as Hartree energy, E_{Hartree}. The fourth term is the classical interaction among the nuclei of the system. The fifth term is the exchange-correlation energy. All the effects of the exchange and correlations on the kinetic energy of electrons is incorporated in this term. The above equation can be written as:

$$E_{\text{KS}} = T_{\text{aux}} + V_{\text{ext}} + E_{\text{Hartree}} + E_{II} + E_{xc} \tag{2.15}$$

2.3.3 Exchange-correlation energy, E_{xc}

The exchange and correlation energy is the difference in the actual kinetic energy and interaction energy of the fully interacting many-particle system and the auxiliary system. In other words, the exchange and correlation energy term E_{xc} groups the exchange and correlattion effects of the many-body interacting system. In terms of Hohenberg-Kohn function, F_{HK} the exchange-correlation can be written as [107]:

$$E_{xc}[n] = F_{\text{HK}} - (T_{\text{aux}} + V_{\text{ext}})$$
$$= T[n] - T_{\text{aux}} + E_{\text{int}}[n] - E_{\text{Hartree}} \tag{2.16}$$

Here, the exchange-correlation energy is written as a functional of density. The functional can be expressed in integral form as follows:

$$E_{xc}[n] = \int dr n(r) \epsilon[n, r] \tag{2.17}$$

Here, $\epsilon[n, r]$ is the energy per electron at a point r, represented as a functional of local density in the electron's locale. The exact ground state density and energy can be

determined by solving the Kohn-Sham equations, given the correct form of exchange-correlation functional [112, 113]. Hence, if the E_{xc} functional is successfully applied, the Kohn-Sham approach leads to determining adequate ground state properties of a many-body interacting system.

2.3.4   Exchange-correlation functionals

The accuracy of the electronic structure calculation through DFT relies largely on the precise determination of the exchange-correlation functional, $\epsilon[n, r]$. There are various approximate methods in Kohn-Sham DFT used to determine the $\epsilon[n, r]$ functional with significant accuracy and practical to implement [114]. The wide acceptance of DFT calculations in computational materials science is attributed to the success of these approximate methods. Several approximations include local density approximation (LDA), generalized gradient approximation (GGA) [115], meta-GGA, and hybrid functionals [116].

  The LDA functional depends on the local density of the electrons. It takes into account the density only in the neighborhood of the electron at a given position. In contrast, GGA incorporates the effect of the gradient of density ∇n. GGA is considered more accurate than the LDA because it depends on the density's variation with position and the density.

$$E_{xc}^{GGA}[n] = \int dr n(r) \epsilon^{GGA}[n(r), \nabla n(r)] \tag{2.18}$$

Meta-GGA is a further improved approach that incorporates the Laplacian of the density, i.e., the second-order derivative of the density with respect to position $\nabla^2 n$. The functionals GGA and meta-GGA are obtained by adding the gradient and laplacian terms to the LDA energy. Hybrid functionals are formulated by adding some fraction of exact exchange energy obtained from the Hartree-Fock methodology to the DFT functionals. Hybrid functionals exhibit higher accuracy than LDA and GGA functionals. However, they incur higher computational costs and time. In this thesis, the properties of advanced

Heaven of chemical accuracy
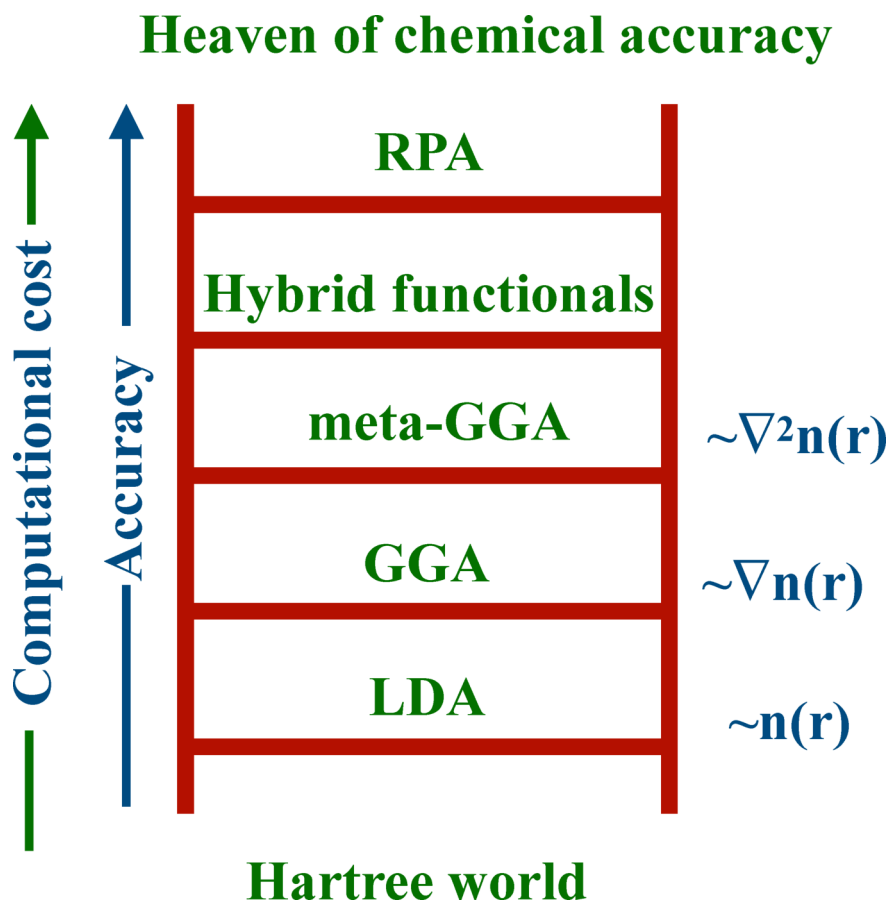
Figure 2.3: Jacob's ladder for exchange-correlation functionals.

energy materials are calculated mainly from the GGA functionals. One of the most widely used GGA functionals is PBE, given by Perdew, Burke, and Ernzerhof [117]. PBE is a parameter-free approach; therefore, it is viable for a variety of materials.

2.3.5   Self-consistent Kohn-Sham equations

The methodology of Kohn-Sham is an independent particle approach with an effective potential to understand the electronic structure of a many-body interacting system. The effective potential must be self-consistent with the exact ground-state density.

$$\hat{H}_{KS}\Psi = E_{KS}\Psi \tag{2.19}$$

Where, $\hat{H}_{KS}$ is Kohn-Sham hamiltonian operator, which contains kinetic energy and effective potential operators:

$$\hat{H}_{KS} = -\frac{1}{2} \sum_{i=1}^{N} \nabla_i^2 + \hat{V}_{eff}(r) \tag{2.20}$$

$$V_{eff}[n, r] = V_{ext}(r) + V_{Hartree}[n] + V_{xc}[n] \tag{2.21}$$

Eq.2.19, 2.20, and 2.21 represent a set of Kohn-Sham equations to be solved self consistently to determine the exact ground state density and energy. The workflow to obtain the self-consistent solutions of Kohn-Sham equations is following.

First, a reasonable guess is made for the ground state density of the system. Then, the effective potential, V_{eff} is calculated with Eq. 2.21. Next, Eq. 2.19 is solved to determine the corresponding electronic wavefunctions, which leads to the determination of a new ground state density. This density is again fed into Eq. 2.21. the loop continues until the self-consistent values of energy and density are obtained. Once the self-consistent ground state density and energy are successfully determined, various ground state and excited state properties can be calculated.

2.4   Basis sets

The quantum mechanical treatment of a system involves representing electronic wavefunction as a linear combination of basis functions called basis sets [107].

$$\psi_i(\vec{r}) = \sum_{\alpha} C_{i\alpha} \phi_\alpha(\vec{r}) \tag{2.22}$$

Here, $\psi_i(\vec{r})$ is the electronic wavefunctions, $C_{i\alpha}$ are the coefficients of expansion and $\phi_\alpha(\vec{r})$ represent the basis functions. The mapping of electronic wavefunctions to suitable basis sets is essential to efficiently implement the differential equation to a computer simulation.

For practically feasible determination of the state of the system, the basis sets must be finite-sized and apt to represent the real wavefunction. The basis sets must lead to fast production computations without any compromise on the accuracy of converged results. A given level of accuracy should be achieved with the least possible number of basis functions in the expansion series. Besides, the basis sets should be transferable among various atomic arrangements. The accuracy of a calculation highly depends on the size of the basis set. The larger the basis sets, the more accurate the calculations will be. However, increasing the number of basis functions requires more computer operations per electron, which incurs higher computational costs. Therefore, usually, there is a tradeoff between the accuracy and the computational cost.

In general, basis sets are categorized into two main classes:

• Atomic basis sets

• Plane-wave basis sets

2.4.1   Atomic-basis sets

Atomic basis sets are generated fundamentally from the linear combinations of the atomic-orbital type basis functions. They are generally centered on the nuclei; thus are often referred to as the localized basis sets. They are the most suitable basis sets for representing the isolated atomic and molecular systems' wavefunctions. The free atoms and molecules' wavefunctions fall off exponentially at the larger distance from the nucleus, and localized basis sets are formulated mainly to possess this characteristic. All the atomic-basis sets approaches are based on the "linear combination of atomic orbitals (LCAO)" theory [118]:

Linear Combination of Atomic Orbitals (LCAO)

LCAO is a well-established methodology to describe molecular orbitals' formulation by the superposition of atomic orbitals having the same energy levels. The superimposing orbitals must have the same symmetry and overlap properly. Usually, the number of

molecular orbitals formed is equal to the number of participating atomic orbitals in the linear combination [118].

Atomic basis sets are generally categorized into:

Slater-type orbitals,

Gaussian-type orbitals, and

Numerical-type orbitals

Slater-type atomic orbitals (STOs):

John C. Slater first introduced Slater-type orbitals in the year 1930 [119]. Here, the radial part and the angular part of the atomic orbitals are treated separately. The following expression gives the radial part:

$$\mathrm{R_{STO}}(r) = \mathrm{N}r^{n-1}\exp[-\mathrm{b}r] \tag{2.23}$$

Here, $\mathrm{R}(r)$ represents the radial part of the orbital and r is the radial distance of electron from the nucleus. N is the normalising constant. Normalising constant can be determined from the following condition:

$$\mathrm{N}^2 \int_0^\infty \left(r^{n-1}\exp[-\mathrm{b}r]\right)^2 r^2 dr = 1 \tag{2.24}$$

This gives:

$$N = (2\mathrm{b})^n \left(\frac{2\mathrm{b}}{(2n)!}\right)^{\frac{1}{2}} \tag{2.25}$$

Here b represents the screening constant. The screening constant describes the effective nuclear charge, which is partially shielded by the surrounding electrons. It is generally referred to as "orbital exponent" and is determined by Slater's rule as written below:

$$\mathrm{b} = \frac{Z - s}{n} \tag{2.26}$$

Here, Z is the atomic number and s represents the screening constant.

The angular part of the Slater-type orbitals are generally represented by the spherical harmonic, $Y_l^m(\theta, \phi)$. Thus, the expression for Slater-type atomic orbital can be written as [119]:

$$\Phi_{n,l,m}(r, \theta, \phi) = R(r)Y_l^m(\theta, \phi) \tag{2.27}$$

$$\Phi_{n,l,m}(r, \theta, \phi) = (2b)^n \left(\frac{2b}{(2n)!}\right)^{\frac{1}{2}} r^{n-1}\exp[-br]Y_l^m(\theta, \phi) \tag{2.28}$$

From the above equation, it is clear that the STOs decay exponentially with r in the long-range, whereas they follow Kato's electron-nucleus cusp condition near the nucleus, i.e., in the short-range. The Slater-type atomic basis sets are mainly used to describe the wavefunctions of atomic or diatomic systems. The integrals that arise for more than two-atom systems can not be solved analytically. Therefore, the molecular systems with more than two atomic centers are often hard to solve within the STO frameworks.

Gaussian-type atomic orbitals (GTOs):

Boys first proposed Gaussian-type atomic orbitals in the year 1950 [120]. They are still one of the most prevailing basis functions in quantum computation programs. Under GTOs' framework, the solutions to Schrödinger's equations in a molecular system are described by the linear combination of Gaussian type atomic orbitals. The radial part is written as a gaussian function of the electron's position with respect to the nucleus, as shown below:

$$\mathrm{R_{GTO}}(r) = \mathrm{N}\exp[-\alpha r^2] \tag{2.29}$$

Here, α is a real parameter that is estimated from the energy minimization. The radial part of the orbital determines the characteristics of the molecular orbital. The GTOs are much simpler to solve and implement on a computational program due to the " gaussian product rule". In the case of a two-centered system, the orbital is calculated at a single point somewhere on the line joining the two centers. Thus, a two-centered integral is

reduced to a one-centered integral. The mathematical form of the product rule for a two-centered GTO is given as follows:

Let the two centers be defined by points as A and B with the respective distances of electrons as r_A and r_B. The radial part of the two-centered orbital is proportional to the product of gaussian functions of r_A and r_B, as shown below:

$$R_{\text{two-center}}(r_A, r_B) \propto \exp[-\alpha r_A^2] \times \exp[-\beta r_B^2] \tag{2.30}$$

Using the "gaussian product rule", the above expression can be reduced to:

$$R_{\text{one-center}}(r_A, r_B) = \exp\left[-\frac{\alpha\beta}{\alpha+\beta}(B-A)^2\right]\exp\left[-(\alpha+\beta)r^2\right] \tag{2.31}$$

Here, r is the position of the electron with respect to the new center-point, C. The position of the new center-point is determined from the following expression:

$$C = \left(\frac{\alpha}{\alpha+\beta}\right)A + \left(\frac{\beta}{\alpha+\beta}\right)B \tag{2.32}$$

Similarly, a four-centered integral is reduced to a two-centered one. Thus, the " gaussian product rule" tremendously improves the ease of the integral calculations and saves computational time.

The angular part of the gaussian orbitals can broadly be expressed in two ways, as in:

• Cartesian-GTOs

• Spherical-GTOs

Cartesian Gaussian type orbitals: In cartesian GTOs, the angular part of the orbital is represented in terms of the cartesian components of the position r. The angular part can be written as:

$$Y(p, q, s) = x^p + y^q + z^s \tag{2.33}$$

where $p + q + s = n$, n is an integer. Thus, the above equation represents a homogeneous polynomial in x,y, and z with degree n. Mathematically, there are $(n + 1)(n + 2)/2$ polynomials in a three-component variable. Therefore, there are 3 cartesian GTOs for $n = 1$; 6 cartesian GTOs for $n = 2$; 10 cartesian GTOs for $n = 3$; and so on. The overall orbital equation can be written on combining the radial and angular parts as follows:

$$\Phi(r, p, q, s) = (x^p + y^q + z^s)\exp[-\alpha r^2] \tag{2.34}$$

Spherical gaussian type orbitals: In spherical GTOs the angular part of the orbital is represented by the spherical harmonic: $Y_l^m(\theta, \phi)$

The overall orbital expression is written as follows:

$$\Phi(r, n, l, m) = Y_l^m(\theta, \phi)\exp[-\alpha r^2] \tag{2.35}$$

n determines the radius of the orbit l and m are angular momentum quantum numbers, that determine the type of the orbital.

r^2 in the exponent of GTOs leads to the rapid decay of the wavefunction with distance from the nucleus. Thus GTOs are rather a poorer representation of the atomic orbitals. Therefore, for the accurate calculations in the framework of GTO, the basis sets must be large. The additional computational operations needed for the larger basis sets are compensated with the GTOs' high computational efficiency.

Numeric atom centered orbitals (NATOs)

Numeric atom-centered orbitals (NAOs) are incorporated in "Fritz Haber Institute-*ab initio* molecular simulations (FHI-aims)" computer simulation package [121]. It is an all-electron and full-potential solution of Kohn-Sham's one-particle equations. Therefore,

NAO is the most accurate localized basis set with no possibility of errors arising from neglecting the core of atoms. The mathematical form of the NAOs consists of two parts, viz., radial function and angular function, as shown below:

$$\Phi(r, \theta, \phi) = \frac{u(r)}{r} Y_l^m(\theta, \phi) \tag{2.36}$$

Here, the angular part of the wavefunction, $Y_l^m(\theta, \phi)$ is represented by the spherical harmonics, whereas the radial part, $u(r)$ is atom-centered and numerically enlisted for individual elements. The availability of basis functions individually for each element leads to more flexible calculations. $u(r)$ are strictly localised within the region specified by a cut-off radius, r_{cut}; outside r_{cut} the radial function falls to zero.

A confinement potential, $V_{conf}(r)$ is added to the potential energy term in the radial equation:

$$\left[-\frac{1}{2}\frac{d^2}{dr^2} + \frac{l(l+1)}{r^2} + V(r) + V_{conf}(r) \right] u(r) = \epsilon u(r) \tag{2.37}$$

where l is the angular momentum of the electron and ϵ denotes the eigen value of the above equation. The function of $V_{conf}(r)$ is to eliminate any slow decaying radial function tails. The shape of $V_{conf}(r)$ is chosen in a way to ensure smooth fall of each radial wavefunction and its deriavatives to zero beyond r_{cut}.

The numeric atom-centered basis sets are constructed by an iterative method as explained here:

The starting point is the smallest basis set that consists of only the free atomic orbital. A large number of candidate radial basis functions of various shapes and characteristics are collected as an open pool. Then, these basis functions are added to the starting free atomic orbital. The function that brings the maximum change in the total energy values is selected to form the basis set. The selection process continues until there is no significant change in the total energy by adding a new basis function.

Therefore, the NAO basis sets can be obtained for a range of problems from minimal free

atomic basis functions to a larger basis set that is required for the energy convergence with accuracy to meV levels. The basis sets so formed are hierarchical, i.e., the larger basis sets naturally carry the smaller basis sets.

2.4.2 Plane-wave basis sets

In the plane-wave basis sets approach, the basis functions are the plane-wave functions:

$$\psi_i = \sum_\alpha C_{i\alpha} \exp[i\vec{G}.\vec{r}] \tag{2.38}$$

Schrödinger's equations with constant potentials have the solutions in the form of plane waves. Hence plane waves are the suitable basis functions for the electronic band structure calculations in free-particle approximations. Plane waves are usually applied for infinite and periodic systems where the electronic wavefunction is governed by Bloch theorem [122, 123].

Bloch theorem

For a periodic crystalline structure, the translation operation by a unitcell length leaves the system unchanged. The lattice translational vector is given by:

$$\vec{T} = n_1\vec{a}_1 + n_2\vec{a}_2 + n_3\vec{a}_3 \tag{2.39}$$

where, $\vec{a}_1$, $\vec{a}_2$, and $\vec{a}_3$ are the primitive lattice vectors. n_1, n_2, and n_3 are the intergers. $\vec{T}$ defines the periodicity of the crystal structure. The electrons in the crystalline system are subjected to a periodic potential:

$$V(\vec{r} + \vec{T}) = V(\vec{r}) \tag{2.40}$$

Under the effect of the periodic external potential, the solutions of the single-electron Kohn-Sham equation take the following form:

$$\Psi_k = u_k(r)\exp(i\vec{k}.\vec{r}) \tag{2.41}$$

Here, $u_k(r)$ is the periodic function of position and has the same periodicity as that of the crystal lattice. $\exp(i\vec{k}.\vec{r})$ is the expression for a plane wave. $\vec{k}$ is the wave vector in the first Brillouin zone. Hence, the electronic orbital can be expressed as plane waves in a crystalline lattice. The function $u_k(r)$ can be written as a function of reciprocal lattice vector, $\vec{G}$ and plane-wave basis sets, c_k, as shown below:

$$u_k(r) = c_k \sum_{\vec{G}} \exp(i\vec{G}.\vec{r}) \tag{2.42}$$

Thus, Eq. 2.41 can be rewritten as:

$$\Psi_k = \sum_{G} c_k u_k(r)\exp(i\vec{k} + \vec{G}.\vec{r}) \tag{2.43}$$

Thus, the Bloch theorem allows representing the electronic wavefunction in terms of expanding plane waves basis functions for each value of k-vector. Theoretically, the complete solution of Kohn-Sham equations consists of an infinite set of plane wave basis functions. However, due to the computational limits, generally, cutoff values for electronic energies, E_{cut} are predefined depending on the system. The expansion of plane waves is truncated at E_{cut} values (explained in more detail in the next section).

Pseudopotentials

The electronic wavefunctions depend on the positions of the electrons inside the atom. The electrons that are near the nuclei are called the core electrons. Thus, the core electrons have almost no interaction with the neighboring atoms or molecules, thus playing

no role in the atom's chemical bonding. The valence electrons majorly govern the chemistry of a system. The valence electrons experience an effective potential of nuclei and electrons. The orbitals for the core electrons are rapidly oscillating, and it is not easy to write the exact plane-wave basis sets for such electrons. The pseudopotential approach is introduced to replace the effect of core electrons and the nuclei with a fictitious potential [124, 125]. While the plane waves well define the electronic orbitals in the outer region. Generally, there is a cutoff radius from the nucleus, beyond which the valence electrons are described by the plane waves and take part in the chemical interactions that govern the condensed matter system. The pseudopotential methods drastically reduce the number of plane-wave basis sets required for solving Kohn-Sham equations; thus, they need less computational memory and enhance the computational speed.

In the early attempts of developing pseudopotentials, the electrostatic potential was simply replaced by a repulsive core. This approach worked fine for the analytical calculations but failed during the expansion of the basis sets. Another proposed approach was to use the empirical potentials. In this method, the pseudopotentials are obtained by fitting band structures, ground-state energies, and other bulk properties of the system to the experimental data. The empirical pseudopotentials hold good for the specific systems but can not be generalized to describe other materials.

Ab initio Pseudopotentials

The *ab initio* pseudopotentials are formulated from the all-electron calculations. Such pseudopotentials maintain most of the characteristics of the all-electron potentials, thus offer much-improved accuracy. Here, the valence electron wavefunctions remain unaltered on introducing pseudopotentials in the core region. Therefore, all-electron wavefunctions and pseudo wavefunctions are the same outside the core region. *Ab-initio* pseudopotential approach requires the conservation of eigenvalues, charge density, and the scattering properties of the core. For the accurate calculations of the exchange and correlation energy

and bonding characteristics of the atom, the pseudo wavefunctions and the all-electron wavefunctions must be the same outside the core region. There are two types of *ab-initio* pseudopotential:

1. Norm Conserving Pseudopotentials (NCPP)

2. Ultrasoft Pseudopotentials (USPP)

Norm Conserving Pseudopotentials (NCPP)

As the name suggests, norm conserving pseudopotential approach, the norms of the pseudo wavefunction and the original wavefunction are equal within the core region [124, 126]. Mathematically, the norm conserving condition can be expressed as follows:

$$\int_0^{r_c} \Phi_{\text{ae}}^*(r)\Phi_{\text{ae}}(r)dr = \int_0^{r_c} \Phi_{\text{pseudo}}^*(r)\Phi_{\text{pseudo}}(r)dr \tag{2.44}$$

Where, Φ_{ae} denotes the all-electron wavefunction and Φ_{pseudo} denotes the pseudo wavefunction.

The norm-conserving pseudopotentials consist of two parts, viz. the radial part and the angular part.

$$V_{\text{NCPP}} = V_{\text{local}}(r) + V_{\text{non local}}(l) \tag{2.45}$$

$$V_{\text{non local}}(l) = \sum_l V_l(l)|l><l| \tag{2.46}$$

The angular part of the potential is written separately for each angular momentum of the electron; thus is the nonlocal potential. The presence of the nonlocal potential makes the NCPP as transferable [127]. Therefore, NCPP is suitable for explaining various characteristics of the nucleus under a variety of atomic environments. The other conservation conditions for the NCPP are:

1. The total orbital energy of the all-electron orbitals and the pseudo orbitals is the same inside the core region: $\epsilon_{\text{ae}} = \epsilon_{\text{pseudo}}$

2. The all-electron wavefunction and pseudo wavefunction are the same outside the core region: $\Phi_{ae}(r) = \Phi_{pseudo}(r); r > r_c$

The limitation of the NCPP is that they are still hard and computationally expensive.

Ultrasoft Pseudopotentials (USPP)

The norm-conserving constraint is lifted in the ultrasoft pseudopotential approach, which allows efficient calculations through much smoother pseudopotentials [128]. The pseudo wavefunction is very soft within the core region that can be described by a smaller basis set. As the norm conservation is not followed, the charge density inside and outside the core region is matched with an augmentation charge density added to the core region. The augmentation charge is the difference in the norms of the all-electron wavefunction and the pseudo wavefunction, as described below:

$$Q_{nm}(r) = \Phi_n^{ae*}(r)\Phi_m^{ae}(r) - \Phi_n^{USPP*}(r)\Phi_m^{USPP}(r) \tag{2.47}$$

where $\Phi^{ae}(r)$ and $\Phi^{USPP}(r)$ respectively denote the all-electron wavefunction and the pseudo wavefunction under ultrasoft pseudopotential formalism. The total augmentation charge can be written as:

$$q_{nm}(r) = \int_0^{r_c} Q_{nm}(r)dr \tag{2.48}$$

The pseudopotential can be written as:

$$V^{USPP}(r) = V_{local}(r) + \sum_{nml} D_{nm}|\beta_n^l><\beta_m^l| \tag{2.49}$$

Here, $|\beta_n^l>$ is called as projector function. The projector function is strictly localised inside the core region.

$$|\beta_n> = \sum_m \frac{|\chi_m>}{<\chi_m|\Phi_n>} \tag{2.50}$$

And the D-function can be written as:

$$D_{nm} = <\Phi_n|\chi_m> + \epsilon_m q_{nm} \tag{2.51}$$

Muffin-tin approximation

Muffin-tin approximation divides the crystal structure into atomic spherical regions and the interstitial regions. Each lattice point is surrounded by a sphere of radius r_s, the potential within r_s is spherically symmetric and constant outside r_s [129].

$$V_{\text{mt}} = \begin{cases} V(r) & \text{when } r < r_s \\ \text{constant} & \text{when } r \geq r_s \end{cases} \tag{2.52}$$

Augmented plane wave (APW) method

The augmented plane wave (APW) method was first proposed by John C. Slater in 1937 [129]. The potential formulation is based on the "Muffin-tin" approximation. The constant potential in the interstitial region leads to plane wave solution of the Schrödinger's equation. Whereas, within the spherical regions surrounding the atoms, the wavefunctions are obtained by solving the Schrödinger's equations for free atoms. This can be expressed as follows:

$$\Phi_k(r) = \begin{cases} c_k exp(i\vec{k}.\vec{r}) & \text{when } r \geq r_s \\ \text{atomic function} & \text{when } r > r_s \end{cases} \tag{2.53}$$

The wavefunction must be continuous at the boundary of the spherical regions.

Linearised augmented plane wave (LAPW) method

O.K. Andersen suggested a linearized augmented plane wave (LAPW) method in 1975 [130]. Like APW method, Linearised augmented plane wave (LAPW) method partitions the crystal structure into the atomic and the interstitial regions. The approximate solutions of Schrödinger's equations are atom-like functions inside the spherical regions and smoothly varying plane-wave functions in the interstitial regions. The LAPW basis functions are composed of the atom-like functions that provide an adequate representation in the core region and the plane wave functions that enable efficient calculations for various geometries. Under high-pressure conditions, the outer-core electronic states are significantly affected. LAPW method allows incorporating the core and semi-core electrons into the calculations explicitly.

Projector Augmented Wave (PAW) method

The projector augmented wave (PAW) method is a suitable approximation for electronic structure calculations [131]. It combines the approaches of pseudopotentials and the linearized augmented plane wave (LAPW) method. The cutoff radius, R_{cut}, defines a sphere around the nucleus, called augmentation. The electronic wavefunctions within the augmentation sphere are written as partial wave expansions, whereas, outside the augmentation sphere, the electronic wavefunctions are described by the plane waves. The PAW method requires the transformation of the actual wavefunction, Φ^{ae}, in the augmented region to a pseudo wavefunction, Φ^{pseudo} with the help of the transformation operator $\hat{\zeta}$.

$$|\Phi^{pseudo}> = \hat{\zeta}|\Phi^{ae}> \tag{2.54}$$

The pseudo wavefunction is written as the linear combination of pseudo electronic orbitals, also called partial waves:

$$\Phi^{pseudo} = \sum_i c_i \phi_i^{pseudo} \tag{2.55}$$

Whereas the original wavefunction is written as the linear combination of actual electronic orbitals:

$$\Phi^{\mathrm{ae}} = \sum_i c_i \phi_i^{\mathrm{ae}} \tag{2.56}$$

The transformation operator is chosen such that, outside the augmentation sphere, the pseudo and original electronic orbitals must exactly be the same. Mathematical expression for the transformation operator is as follows:

$$\hat{\zeta} = 1 + \sum_i \left(|\phi_i^{\mathrm{ae}}> - |\phi_i^{\mathrm{pseudo}}> \right) <p_i| \tag{2.57}$$

Where p_i is the projector function that is strictly localised in the augmented region. It governs the characteristics of the pseudo wavefunction inside the core region. the projector functions are orthogonal to the pseudo wavefunction: $<p_i|\phi_j^{\mathrm{pseudo}}> = \delta_{i,j}$.

2.4.3   Cut off energy

For a crystalline structure, the Bloch theorem provides a way to expand the electronic wavefunctions into discrete plane-wave basis sets for each k-point value as in Eq. 2.43. Theoretically, the expansion of a wavefunction requires an infinitely large basis set. However, it is not computationally feasible. Note that the plane waves with higher kinetic energy values (lower wavelength) contribute to minor improvements and require much finer grid points in calculations. Therefore, it is recommended to truncate the basis set expansion by introducing a cutoff value for the kinetic energy. The kinetic energy for a plane-wave is expressed as Eq. 2.43 can be written as:

$$\mathrm{K.E} = \frac{\hbar^2}{2m}|k + G|^2 \tag{2.58}$$

The cutoff energy can be written as:

$$(\text{K.E})_{\text{cut}} = \frac{\hbar^2}{2m}|k + G_{\text{max}}|^2 \tag{2.59}$$

$(\text{KE})_{\text{cut}}$ represents a sphere in the reciprocal space that contains all the $|k + G|$ values used; the $|k + G|$ values lying outside the sphere are not taken into account.

For a reliable geometry optimization and computation of the system's properties, it is crucial to incorporate a larger basis set in the calculation, i.e., the chosen value of $(\text{KE})_{\text{cut}}$ should be large enough to prevent any truncation errors. It is often advised to increase the $(\text{KE})_{\text{cut}}$ value until the total energy is converged within the tolerance limits.

2.5 K-point Sampling

With the help of the Bloch theorem, the problem of an infinite periodic system is reduced to one unit cell. The solution of Schrödinger's equation is obtained for the values of k that are lying in the first Brillouin zone of the reciprocal lattice. The first Brillouin zone (BZ) is the unique smallest area near $G = 0$ in the reciprocal space of the lattice [107]. Due to periodicity, all the k-points of the entire space are mapped onto the first BZ. Therefore, sampling the BZ leads to the determination of the electronic states for the entire space just by solving the DFT equations for one unit cell. This leads to significant computational simplification.

Special k-points

To evaluate the electronic state of the system in the first BZ, the contributions from all the electrons in the unit cell are taken into account. The total value of a function $f(\vec{k})$ for the whole crystal can be evaluated from the integral: $\int_{BZ} d\vec{k} f(\vec{k})$. In order to calculate the integral with the help of a computer program, the integral is replaced with a weighted

sum over a finite number of k-values [132, 133], called as special k-points, that is:

$$\int_{BZ} d\vec{k} f(\vec{k}) = \frac{V_{\text{BZ}}}{\text{N}_k} \sum_n^{\text{N}_k} f(k_n) \qquad (2.60)$$

where, V_{BZ} is the volume of the BZ and N_k is the number of the special k-points.

Irreducible Brillouin zone(IBZ)

Irreducible Brillouin zone(IBZ) is the smallest area of space close to G=0 in the BZ with no two same k values. If the state of the system is known in the IBZ, the information about the whole BZ can be determined. The symmetry of a crystalline structure reduces the number of unique k-points. The whole BZ can be mapped into the IBZ by the following expression:

$$\sum_{\vec{k}_n \in BZ} f(\vec{k}_n) = \sum_{\vec{k}_n \in IBZ} f(w(k_n)\vec{k}_n) \qquad (2.61)$$

Where, $w(k_n)$ represents the weight of a k-point. Discretization over a dense mesh of special k-point of the integrand as shown in Eq. 2.60 is a crucial step in a computational study. This can be done with the following k-point sampling schemes:

1. Gamma only

2. Gamma-centered

3. Monkhorst and Pack

Gamma only

The center of the Brillouin zone is called the Gamma-point, where the coordinates of $\vec{k}$ are (0,0,0). In this scheme, only the center of the BZ is sampled.

Gamma-centered

In the Gamma-centered sampling scheme, a mesh of special k-point centered at the origin of the BZ is used to sample the whole BZ. Unlike the Gamma-only sampling method, the Gamma-centered scheme samples more than one value of the k-points.

Monkhorst and Pack

Monkhorst and Pack method provides a special technique to prepare the k-point mesh [134]. The special k-points are distributed uniformly in the whole BZ [135]. The special k-points are arranged in grids with equispaced fractional coordinates in the reciprocal space. The grid dimensions are generally specified by $k_x \times k_y \times k_z$, which means that there will be k_x points in one dimension, k_y points in the second dimension and k_z points in the third dimension of the BZ. The fractional coordinates of the selected k-points can be obtained from the following expression:

$$u_x = \frac{2x - k_x - 1}{2k_x} \tag{2.62}$$

where $x = 1, 2, \ldots, k_x$.

Similarly, the fractional coordinates for the other two directions, viz. u_y and u_z are obtained to create a uniform mesh of k-points having coordinates: (u_x, u_y, u_z).

After the determination of uniform k-mesh, the number of k-points is further reduced to unique points as in the irreducible Brillouin zone (IBZ) by applying the symmetry operations of the Bravais lattice. Then, the appropriate weighting for all the k-points is calculated. Finally, the discretization of the integrand corresponding to a specific function is performed as shown in Eq. 2.61.

2.6 *Ab-initio* thermodynamics

The calculations performed in the DFT realm give insights about a system's properties only at 0 K temperature. However, a system can behave in various manners depending on environmental conditions like temperature and pressure. To give reliable guidance to experiments through computational studies, one needs to determine the system's true behavior under the given experimental environmental conditions. In computational studies, the effects of finite temperature and pressure can be estimated with the help of *ab-initio* thermodynamics. *Ab-initio* thermodynamics uses the first-principles approach to determine the thermodynamic potentials like Gibb's free energy of the system. The larger system is divided into smaller subsystems that are essentially in equilibrium with one another. The macroscopic properties of the larger system are obtained by evaluating the subsystems individually and then combining them with the help of corresponding thermodynamic potentials, e.g., internal energy, Helmontz free energy, enthalpy, and Gibb's free energy. For a system with constant temperature and volume, the system equilibrates by minimizing Helmontz free energy: $F = U - TS$, whereas, if temperature and pressure are constant, then Gibb's free energy is minimized: $G = U + pV - TS$. G is also written as:

$$G = \sum_i N_i \mu_i \tag{2.63}$$

where μ_i is the chemical potential of ith species added to the system. It represents the amount of energy released or required to add or remove an atom to the system.

The free energies can be computed with the help of partition function, Z as shown below:

$$F = -k_B T \ln Z \tag{2.64}$$

and

$$G = -k_B T \ln Z + pV \tag{2.65}$$

Z is a function of macroscopic quantities like temperature, volume, pressure, energy, and composition. A general formula to calculate Z is written as:

$$Z = \sum_i \exp\left[\frac{\epsilon_i}{k_B T}\right] \tag{2.66}$$

This gives the probability of finding the system in ith microstate. The energy of a system at finite temperature can be obtained from adding the contributions from all the degrees of freedom such as translational, rotational, vibrational, configurational, and electronic energies, as shown below:

$$\epsilon_i = \epsilon_{i,trans} + \epsilon_{i,rot} + \epsilon_{i,vib} + \epsilon_{i,conf} + \epsilon_{i,ele} \tag{2.67}$$

This gives,

$$Z = \sum_i \exp\left[\frac{\epsilon_{i,trans}}{k_B T}\right] \times \sum_i \exp\left[\frac{\epsilon_{i,rot}}{k_B T}\right] \times \sum_i \exp\left[\frac{\epsilon_{i,vib}}{k_B T}\right]$$
$$\times \sum_i \exp\left[\frac{\epsilon_{i,conf}}{k_B T}\right] \times \sum_i \exp\left[\frac{\epsilon_{i,ele}}{k_B T}\right] \tag{2.68}$$

$$Z = z_{trans} \times z_{rot} \times z_{vib} \times z_{conf} \times z_{ele} \tag{2.69}$$

Thus, the partition function is obtained from the product of contributions from all the degrees of freedom.

2.6.1 Translational free energy

Let the momenta of particle in x, y, and z directions is represents by P_x, P_y, and P_z respectively. The kinetic energy is written as:

$$\text{K.E} = \frac{P_x^2 + P_y^2 + P_z^2}{2m} \tag{2.70}$$

where, m is the mass of particle. This gives the expression for translational partition function from Eq. 2.66, as follows:

$$z_{trans} = \frac{1}{h^3} \int_{-\infty}^{\infty} \int_{-\infty}^{\infty} \exp\left[-\frac{P_x^2 + P_y^2 + P_z^2}{2\mathrm{m}}\right] dP_x dP_y dP_z dx dy dz \tag{2.71}$$

This gives,

$$z_{trans} = \frac{V}{h^3} \int_{-\infty}^{\infty} \exp\left[-\frac{P_x^2}{2\mathrm{m}}\right] dP_x \int_{-\infty}^{\infty} \exp\left[-\frac{P_y^2}{2\mathrm{m}}\right] dP_y \int_{-\infty}^{\infty} \exp\left[-\frac{P_z^2}{2\mathrm{m}}\right] dP_z \tag{2.72}$$

The above equation is solved using gamma integrals and results to:

$$z_{trans} = V \left(\frac{2\pi \mathrm{m k_B} T}{h^2}\right)^{3/2} \tag{2.73}$$

The translational free energy is written with the help of the translational partion function calculated above. The translational free energy:

$$\mu_{trans} = \frac{1}{N} \left(-\mathrm{k_B} T \ln z_{trans} - pV\right) \tag{2.74}$$

Using Eq. 2.73 and ideal gas equation: $pV = N\mathrm{k_B}T$, we can rewrite above equation as:

$$\mu_{trans} = -\mathrm{k_B} T \ln \left[\left(\frac{2\pi m \mathrm{k_B} T}{h^2}\right)^{3/2} \frac{\mathrm{k_B} T}{p}\right] \tag{2.75}$$

2.6.2   Rotational free energy

The rotational kinetic energy of the particle is written as:

$$(\mathrm{K.E})_{rot} = \frac{1}{2I} \left(P_\theta^2 + \frac{P_\phi^2}{sin^2\theta}\right) \tag{2.76}$$

where I is the moment of inertia of the particle. The partition function can be written as:

$$z_{rot} = \frac{1}{h^2} \left(\int_{-\infty}^{\infty} \exp\left[-\frac{P_\theta^2}{2I}\right] dP_\theta \int_{-\infty}^{\infty} \exp\left[-\frac{P_\phi^2}{2I \sin^2\theta}\right] dP_\phi \int_0^\pi \sin\theta d\theta \int_0^{2\pi} d\phi \right) \quad (2.77)$$

Solving the above integrals, we get:

$$z_{rot} = \frac{8\pi^2 I k_B T}{h^2} \quad (2.78)$$

The rotational free energy can be written as:

$$\mu_{rot} = -k_B T \ln\left[\frac{8\pi^2 I k_B T}{h^2}\right] \quad (2.79)$$

2.6.3   Vibrational free energy

The energy of various vibrational modes under harmonic approximation can be written as:

$$(E_n)_{vib} = \sum_{i=1}^{N} \left(n_i + \frac{1}{2}\right) \hbar\omega \quad (2.80)$$

The partion function for discrete energy levels is written as:

$$z_{vib} = \sum_n \exp\left[\frac{-E_n}{K_B T}\right] \quad (2.81)$$

$$z_{vib} = \sum_n \exp\left[\frac{\sum_{i=1}^{N} \left(n_i + \frac{1}{2}\right) \hbar\omega}{k_B T}\right] \quad (2.82)$$

$$z_{vib} = \prod_{i=1}^{N} \left(\sum_n \exp\left[\frac{\left(n_i + \frac{1}{2}\right) \hbar\omega}{k_B T}\right] \right) \quad (2.83)$$

$$= \prod_{i=1}^{N} \left(\exp\left[-\frac{\hbar\omega}{2k_B T}\right] + \exp\left[-\frac{3\hbar\omega}{2k_B T}\right] + \ldots \right) \quad (2.84)$$

This gives,

$$z_{vib} = \left(\frac{\exp\left[-\hbar\omega/2k_BT\right]}{1 - \exp\left[-\hbar\omega/k_BT\right]} \right)^N \tag{2.85}$$

The vibrational free energy is written as:

$$\mu_{vib} = \frac{N\hbar\omega}{2} + k_BT\ln\left[1 - \exp\left[-\frac{\hbar\omega}{k_BT}\right]\right] \tag{2.86}$$

2.6.4 Electronic energy

The elerctronic energy is majorly estimated from the total DFT energy of the molecule and spin degeneracy term:

$$\mu_{elec} = E^{DFT}(gas) - k_BT\ln J \tag{2.87}$$

where J represents the spin degenracy of the electrons.

2.6.5 configurational energy

The configurational partition function is written as:

$$z_{conf} = \frac{1}{\sigma} \tag{2.88}$$

where, σ represents the symmetry number. σ is equal to 1 for a heteroatomic gas, whereas it is equal to 2 for a homoatomic gas. The free energy related to configuration is equal $-k_BT\ln\sigma$

2.6.6 Chemical potential of a gas

The chemical potential of a system in gaseous phase can be written with the help of Eq. 2.63 as:

$$\mu_{gas}(T, p) = \frac{G}{N} = \frac{-k_B T \ln Z + pV}{N} \tag{2.89}$$

where N is the total number of molecules of the gas. Using the relations by Eq. 2.75, 2.79, 2.86, and 2.87, μ_{gas} can be written as:

$$\mu_{gas}(T, p) = -k_B T \ln \left[\left(\frac{2\pi m k_B T}{h^2} \right)^{3/2} \frac{k_B T}{p} \right] - k_B T \ln \left[\frac{8\pi^2 I k_B T}{h^2} \right]$$
$$+ \frac{N\hbar\omega}{2} + k_B T \ln \left[1 - \exp \left[-\frac{\hbar\omega}{k_B T} \right] \right] + E^{DFT}(gas) - k_B T \ln J - k_B T \ln \sigma \tag{2.90}$$

2.6.7 Free energy of lattice

In solids, the translational free energy and the rotational free energy do not contribute to the total energy. The vibrational free energy is calculated from the harmonic approximation is given by Eq. 2.86. Therefore, the total Gibb's free energy at finite temperature is written as:

$$G(T, p) = E^{DFT} + \frac{\hbar\omega}{2} + k_B T \ln \left[1 - \exp \left[-\frac{\hbar\omega}{k_B T} \right] \right] \tag{2.91}$$

2.7 Genetic Algorithm (GA)

Genetic algorithm (GA) is a robust search technique that uses the fundamental idea of "survival of the fittest"[136, 137, 138]. Inspired by Charle Darwin's theory of evolution, GA selects the fittest individuals from a large population; uses the crossover and mutation methods, as in the reproduction process; produce new individuals that receive their characteristics from the initially selected parents; and added to the next generation population. The process of selection, crossover, and mutation continues iterating depending on the convergence criterion. Eventually, a population of the fittest individuals is achieved.

Genetic algorithm is a popular theory and being practiced since the 1970s. The powerful search mechanism of the GA is used in numerous applications, including telecommunication, finance, and materials science. In materials science, GA is mainly used to determine the most stable spatial arrangement of a given number of atoms in the form of clusters. Clusters' properties can significantly vary from their bulk counterparts because of differences in the coordination number of atoms in the bulk and clusters. In a cluster study, determining the ground state cluster structure is a very challenging and crucial piece of work. We have used cascade genetic algorithm (cGA) as implemented in FHI-aims computer program package. cGA uses the results of previous steps to perform the next step. It finds the most stable cluster structure (global minimum) by exploring the potential energy surface (PES) [139]. The process of finding out the global minimum includes five main phases:

1. Creation of a random pool of a large number of candidate structures: Initial population

2. Selection of parents with the help of a fitness function for reproduction and generation of new population

3. Crossover of parents to produce the offsprings

4. Mutation of individual offsprings to bring the modifications

5. Termination of the iterations after a specific convergence criterion is satisfied.

2.7.1   Initial Population

Initially, a large pool of candidate solutions to a particular problem is designed. In the case of geometry optimization of a cluster, various possible atomic arrangements are randomly chosen to form an initial population. cGA first pre-scans the whole Potential energy surface to find out the most suitable candidate structures with the help of classical force fields. The pre-scanning is done in order to create a more reliable initial guess that facilitates the further search process of the global minimum with respect to the total energy. As the initial population of candidate structures is created randomly, it

can incur a substantial computational cost if the local minima scanning is done through DFT. Therefore, using the inexpensive classical force fields enables the pre-scanning of the PES at a much lower computational cost and speeds up the search process without compromising the computational accuracy.

2.7.2   Selection of parents

The cluster structures are locally optimised with the classical force field in the pre-scanning procedure explained above. Now, the clusters in the initial pool are selected pairwise to mate and produce the new generation of the structures. This is done as explained below: There is a fittness function, f_n associated with each candidate cluster structure, identified by index n.

$$f_n = \frac{\epsilon_n}{\sum \epsilon_n} \tag{2.92}$$

where ϵ is the relative total energy of individual candidate cluster. ϵ_n for nth cluster can be written as:

$$\epsilon_n = \frac{\mathrm{E_{max}} - E_n}{\mathrm{E_{max}} - \mathrm{E_{min}}} \tag{2.93}$$

Where, $\mathrm{E_{max}}$ and $\mathrm{E_{min}}$ respectively denote the maximum and the minimum total energies of the clusters in the population at a given iteration step. It is clear from the above equation that the cluster with lower total energy values possesses higher fitness and vice versa.

The probability of selecting the clusters (often called parents) to form the next generation population depends on the value of the fitness function; the higher the fitness of an individual parent, the higher are the chances of it mating with another parent.

2.7.3   Crossover

There are many ways in which the selected pair of parents can crossover and make a child. The parent clusters are first reoriented about the origin of their geometries before mating.

The different crossover scheme are explained here:

Let cluster A and cluster B denote the selected parents, each consisting of N number of atoms. For an even N, N/2 atoms are taken from each parent to form the offspring. The x, y, z coordinates of the atoms in a given cluster are taken from the geometry file. A plane at $z = z_A$ is chosen in the geometry of cluster A such that it divides the total number of atoms into two halves. Similarly, a suitable $z = z_B$ plane is chosen for cluster B. Now, the parents' selection of atoms is made so that N/2 atoms are taken from cluster A that are above $z = z_A$ plane, and N/2 atoms are taken from cluster B that are below $z = z_B$ plane. In the case of the odd value of N, an extra atom is taken from the parent, which possesses a higher fitness value. The two fragments are then assembled and form a new cluster structure. In case the atoms in the assembled unit are closer than the threshold distance, the two parts are moved away along the z-axis until the threshold distance is maintained among the atoms.

Another crossover scheme is much similar to the "cut and splice" technique of Deaven and Ho. Here, the atoms having positive z values are taken from cluster A and those having negative z values are taken from cluster B. The two parts are then spliced to form a child. The process may produce children with different stoichiometries. However, only those children are selected for the next generation population with the same stoichiometries as the parents.

In another crossover technique, one type of atom is taken from cluster A, and another type of atom is taken from cluster B and combined to make the child.

2.7.4   Mutation

After the new population is formed through selection and crossover, the mutation is done to modify a generation's individuals further. Mutation can be performed by moving the two combining parts along the axis of crossover. This kind of mutation is carried out when the atoms of the combining parts are too close. The other method of mutating the

child is to interchange the spatial coordinates of two atoms. The mutation is performed to improve the newly formed cluster structures' fitness so that the probability of selection for the reproduction can be increased manifold.

2.7.5   Convergence

The condition of convergence is that the process of crossover and mutation produces the new populations that are energetically and structurally similar to the previous populations, i.e., the cGA search mechanism does not produce any new cluster geometries. Once the convergence is reached, the iteration terminates with a new generation of structures that include the global minima. It can also terminate after the completion of a pre-specified number of iterations.

Therefore, cGA is a robust global optimization technique that scans the PES and determines the global minimum structure for a given geometry, along with numerous structures that are energetically closer to the global minimum.

2.8   Molecular dynamics

Molecular dynamics (MD) is a computational tool to analyze a molecular system's evolution with time. MD provides the methods to study the motion of atoms and molecules under external parameters like temperature and pressure [140]. The methods of MD are widely used to study the structure and dynamics of various complex systems. The fundamental of any MD simulation lies in Newtonian mechanics. The MD simulations solve Newton's equations of motion to elucidate the dynamics of a system.

$$\mathrm{F}_I = \mathrm{m}_I a_I = \mathrm{m}_I \frac{d^2 R_I}{dt^2} \tag{2.94}$$

The above equation depicts Newton's second law of motion. Here, F_I represents the instantaneous force acting on a particle having mass m and instantaneous position R. Also, the force can be expressed as a gradient of potential energy:

$$F_I = \nabla_I U(R_1, R_2, \ldots R_N) = \frac{\partial U(R_1, R_2, \ldots R_N)}{\partial R_I} \tag{2.95}$$

U is the potential energy of the system. Combining eq.21 and 22, we get:

$$\frac{\partial U(R_1, R_2, \ldots R_N)}{\partial R_I} = m_I a_I \tag{2.96}$$

The velocity and position of the particle are calculated using standard numerical integration methods.

$$v_I(t) = \frac{1}{m_I} \int \frac{\partial U(R_1, R_2, \ldots R_N)}{\partial R_I} dt + v_0 \tag{2.97}$$

$$R_I(t) = \int v_i(t) dt + R_0 \tag{2.98}$$

Here, v_0 and R_0 are respectively the initial velocities and initial position of the particle. If the initial state of the system is known, the trajectory of particles at every time step can be easily determined by the gradient of the interatomic potential. The initial positions of the particles are usually obtained from the molecular structure. Whereas the distribution of velocities is generally determined from the distribution functions, like the Boltzmann distribution function or Gaussian distribution function, that determine the velocity of a particular particle at a given temperature. The particles' trajectory at each time step so obtained is useful in calculating various transport properties of the material like ion diffusion and equilibrium of the system.

Interatomic potentials: The potential energy function $U(R_1, R_2 \ldots R_N)$ govern the interactions among all the particles of the system. The interatomic potentials are an

essential prerequisite for an MD simulation to run. A force field consists of a set of equations defining the interatomic potentials. In classical MD, various empirical and semi-empirical force fields define the interatomic potentials, e.g., CHARMM, Lennard-Jones, Morse, and Born-Mayer. These force fields depend on a set of parameters that need to be optimized to match the experimental data for a specific system. The choice of a suitable forcefield depends on many factors like accuracy, computational time, and transferability. However, the available force fields do not necessarily depict the new complex systems correctly. There is no universal form of the force fields. One formulation of potentials that works well for a particular system may not yield the other system's desired results. Also, they do not always ensure the transferability of the interatomic bonds under varying temperature conditions.

2.8.1 *Ab Initio* Molecular Dynamics

In *Ab Initio* molecular dynamics simulations, there is no need for such force fields. The interatomic potentials are calculated "on the fly" from the electronic structure calculations. Here, the motion of particles is governed classically by Newton's equations of motion. Whereas the interatomic potentials are determined quantum mechanically. Therefore, AIMD is one parameter-free approach that facilitates the study of the materials for which the parameter formulation is not so straightforward. This method has revolutionized the theoretical studies of new complex solids. AIMD uses the well-known Born Oppenheimer or adiabatic approximation, where the motion of nuclei and electrons are treated separately. The nuclei being much heavier than the electrons, are considered classical masses. At each time-step, the nuclei move, whereas the electrons are assumed to be in their stationary ground states. The instantaneous forces on the nuclei are obtained from the Hellmann-Feynman theorem, also called the "force theorem" [141]:

$$F_I = -\frac{\partial \mathrm{E}}{\partial R_I} \tag{2.99}$$

Here, F_I represents the force experienced by a nucleus positioned at point R_I. E is the energy of the system that can be expressed as the expectation value of hamiltonian:

$$E = <\Psi|\hat{H}|\Psi> \tag{2.100}$$

Hence,

$$F_I = -\left(<\frac{d\Psi}{dR_I}|\hat{H}|\Psi> + <\Psi|\frac{d\hat{H}}{dR_I}|\Psi> + <\Psi|\hat{H}|\frac{d\Psi}{dR_I}> \right) \tag{2.101}$$

According to adiabatic approximation, the electrons are assumed to be in their ground state. Therefore, the differential of the electronic wavefunction with respect to the position of the nucleus is zero. Thus, using Eq. 2.99, Eq. 2.101 reduces to:

$$F_I = - <\Psi|\frac{d\hat{V}_{\text{ext}}}{dR_I}|\Psi> - <\Psi|\frac{dE_{II}}{dR_I}|\Psi> \tag{2.102}$$

$$F_I = - \int d^3 r n(r) \frac{d\hat{V}_{\text{ext}}}{dR_I} - \frac{dE_{II}}{dR_I} \tag{2.103}$$

The above equation is the well known force theorem. Thus, the instaneous force acting on the nuclei is independent of the kinetic energy and the exchange correlation functional. It is explicitly calculated from the ground state density of electrons. However, this formulation requires that the electrons remain in their ground state while the nuclei move. The force is calculated at each time step from the above relation, and the nuclei are advanced to the next time step(t→t+Δt), where the new coordinates for the phase space are calculated classically.

2.8.2   Integration algorithms

The positions and momenta of the nuclei at time step $t + \Delta t$ are calculated by integrating the equations of motions with the help of standard numerical integration methods. There
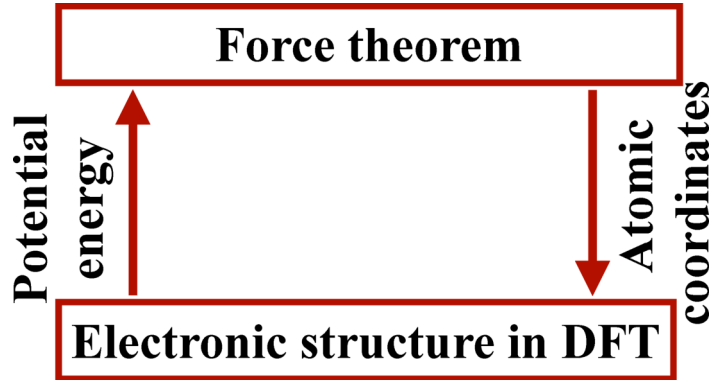
Figure 2.4: scahematic diagram of workflow of *ab-initio* molecular dynamics (AIMD)

are various numerical integration methods, viz., verlet algorithm, leapfrog algorithm, velocity-verlet algorithm. The velocity-verlet algorithm is the most widely used method. The velocity-verlet method is Taylor's series expansion of position and velocity. The formula for the position and velocity is expressed as follows:

$$R(t + \Delta t) = R(t) + \Delta t v(t) + \frac{1}{2}(\Delta t)^2 a(t) \tag{2.104}$$

$$v(t + \Delta t) = v(t) + \frac{1}{2}\Delta t[a(t) + a(t + \Delta t)] \tag{2.105}$$

2.8.3   Ensembles

An ensemble is a collection of many samples of a given system that are replicas of one another regarding their macroscopic properties but may vary in the microscopic states. The average of a particular observable can be calculated with the help of the ensemble average, as given below:

$$< A >_{\text{ensemble}} = \int \int \rho(r^{\text{N}}, p^{\text{N}}) A(r^{\text{N}}, p^{\text{N}}) dr^{\text{N}} dp^{\text{N}} \tag{2.106}$$

where A is an observable; r and p denote the position and momentum of the system. $\rho(r^{\text{N}}, p^{\text{N}})$ represents the probability density, that can be calculated from the partition

function method as shown below:

$$\rho(r^{\mathrm{N}}, p^{\mathrm{N}}) = \frac{\exp\left[-\mathrm{H}(r^{\mathrm{N}}, p^{\mathrm{N}})/\mathrm{k_B}T\right]}{\int\int dr^{\mathrm{N}}dp^{\mathrm{N}}\exp\left[-\mathrm{H}(r^{\mathrm{N}}, p^{\mathrm{N}})/\mathrm{k_B}T\right]} \tag{2.107}$$

The denominator in the above equation represents the partition function.

Therefore, calculating the ensemble average of a quantity requires evaluating all the possible states of a system.

Ergodic hypothesis

According to the ergodic hypothesis, "if a system is allowed to evolve for a sufficiently long time, it will pass through all the possible states". That means calculating average over a large ensemble and over a long period are equivalent. The hypothesis can be explained with the following expression:

$$< \mathrm{A} >_{\mathrm{ensemble}} = < \mathrm{A} >_{\mathrm{time}} \tag{2.108}$$

The time average can be written as:

$$< \mathrm{A} >_{\mathrm{time}} = \lim_{\tau\to\infty} \frac{1}{\tau} \int_{t=0}^{\tau} A(r^{\mathrm{N}}(t), p^{\mathrm{N}}(t))dt \tag{2.109}$$

The idea of the MD simulations is based on the ergodic hypothesis. The above axiom requires that the time limit should be indefinite. However, practical simulations are fixed in time. Therefore, it is usually advised to sample the phase space as much as possible. The MD simulations can be carried out in many ensemble conditions, i.e., microcanonical, canonical, grand canonical ensembles.

Microcanonical (NVE) ensemble

When the total number of particles (N), volume of the lattice (V), and energy of the system (E) are kept constant throughout the simulation, MD is carried out in a microcanonical ensemble. Here, the system is completely isolated with no heat or matter exchange with the surroundings.

Canonical (NVT) ensemble

In the canonical ensemble, the total number of particles (N), volume of the cell (V), and temperature (T) are constant thermodynamic parameters. Here the system is kept in contact with an infinite heat reservoir. However, the exchange of particles is completely restricted. The temperature control in the isothermal MD simulations is done with the help of thermostats. Various thermostats follow different algorithms to exchange energy with the system in order to keep the temperature conserved. The examples of thermostat algorithms include "velocity scaling", "Anderson's thermostat", "Berendsen's thermostats", "Langevin's thermostat", and "Nose-Hoover thermostats".

Velocity rescaling method: Isokinetic thermostat

The velocity-rescaling algorithm starts from a random set of initial velocities for the particles. The randomly selected values of the velocities are then scaled to the appropriate outcomes for the desired temperature by the following expression:

$$\frac{3}{2}k_B T = \frac{1}{2}Mv^2 \qquad (2.110)$$

Where M is the mass of the particle, k_B, T is the desired temperature, and v is the velocity of a particle.

The velocities of all the particles are rescaled after a specific number of time-steps by

multiplying with a factor $\sqrt{T/T(t)}$. where $T(t)$ is the instantaneous temperature. The velocity-rescaling method may slightly deviate from the canonical ensemble conditions depending on the number of time steps after which the velocities are rescaled.

Velocity rescaling method: Berendsen thermostat

In Berendsen thermostat approach, the temperature is altered by coupling the system with a heat bath maintained at temperature T_0 [142]. The velocities are rescaled by multiplying them with a factor given below:

$$\lambda = \sqrt{1 + \frac{\Delta t}{\tau}\left(\frac{T(t)}{T_0} - 1\right)} \tag{2.111}$$

Δt is the time-step of MD simulation, and $T(t)$ is the instantaneous temperature. τ represents the coupling constant that determines the coupling quality between the heat bath and the system.

Stochastic collision method: Anderson's thermostat

Anderson's thermostat maintains the temperature to the desired value by coupling the system to a heat bath [140]. The coupling is done with the help of stochastic collisions that act on the randomly chosen particles after a few time steps. Each stochastic collision changes the momentum of one particle. In between the two successive collisions, the system evolves according to the usual equations of motion. The Poisson's distribution gives the probability of a collision occurring in the time interval between t and $t + \delta$t:

$$P(t, \nu) = \nu \exp\left[-\nu t\right] \tag{2.112}$$

ν represents the collisions' frequency that determines the coupling between the system and heat bath. The collisions affect one particle at a time, and the new momentum value for this particle is determined from the Boltzmann distribution. The change in momentum

of the particle is added to the equations of motions at the instant of the collisions, and the equation of motions is solved normally for all the particles at other times.

Extended system method: Nose-Hoover thermostat

In the extended system approach to preserve the canonical ensemble in an MD simulation, the system is coupled to a heat bath where an additional degree of freedom corresponding to the heat bath is added to the actual equations of motion [143, 144, 145]. The additional degree of freedom, S is assumed to have a mass "Q" associated with it.

The variables in the extended phase space are scaled as per the following relations:

$\tilde{dt} = dt/S$;

$\tilde{q} = q$;

$\tilde{p} = p/S$;

$\dot{\tilde{q}} = S\dot{q}$ and

$\dot{\tilde{p}} = \dot{p}$

Here, q and p are the coordinates of phase space in the real system. $\tilde{q}$ and $\tilde{q}$ denote the coordinates in the extended system. Lagrangian in the extended system can be written as:

$$L_{\text{ext}} = \sum_I^N \frac{1}{2} M_I \dot{\tilde{q}}_I^2 - U(\tilde{q}) + \frac{1}{2} Q\dot{S}^2 - g k_B T \ln S \qquad (2.113)$$

This gives,

$$L_{\text{ext}} = \sum_I^N \frac{1}{2} M_I S^2 \dot{q}_I^2 - U(q) \frac{1}{2} Q\dot{S}^2 - g k_B T \ln S \qquad (2.114)$$

Here, the first term is the kinetic energy of the particles; the second term is the potential energy; the third and fourth terms respectively denote the kinetic energy and potential energy of the additional entity S. g is the degree of freedom, which is one more than the real system's usual degree of freedom. The logarithmic term in the potential energy ensures the canonical behavior of the extended system.

The hamiltonian for the extended system is written as:

$$H_{\text{ext}} = \sum_I^N \frac{p_I^2}{2M_I S^2} + U(q) + \frac{p_S^2}{2Q} + g k_{\text{B}} T \ln S \qquad (2.115)$$

where, p_S is the momentum corresponding to S.

The system evolves through the following equations of motion:

$$\frac{dq_I}{dt} = \frac{\partial H_{\text{ext}}}{\partial p_I} \qquad (2.116)$$

$$\frac{dp_I}{dt} = -\frac{\partial H_{\text{ext}}}{\partial q_I} \qquad (2.117)$$

$$\frac{dS}{dt} = \frac{\partial H_{\text{ext}}}{\partial p_S} \qquad (2.118)$$

$$\frac{dp_S}{dt} = -\frac{\partial H_{\text{ext}}}{\partial S} \qquad (2.119)$$

Grandcanonical (μ,V,T)ensemble

When the system has constant chemical potential (μ), volume of the cell (V), and temperature (T), it is said to be in grandcanonical ensemble. Here, the system is coupled to an infinite heat reservoir with which it can exchange of heat as well matter.

Chapter 3

Role of charged defects in the dehydrogenation of complex metal hydrides at realistic conditions

Introduction

Complex metal hydrides are very suitable materials for the storage of molecular hydrogen [28, 29, 30, 31, 32]. NaAlH$_4$ is a prototypical system that is widely studied for the application of hydrogen storage [42]. The release of hydrogen takes place via the following reactions [28]:

$3NaAlH_4 \rightarrow NA_3AlH_6 + 2Al + 3H_2$

$NA_3AlH_6 \rightarrow 3NaH + Al + 1.5H_2$

$NaH \rightarrow Na + H_2$

The hydrogen release in the first step is 3.7 wt.%. Whereas, in the second step, 1.9 wt.% hydrogen is released. The dissociation of NaH is possible only at very high temperatures. Hence, the overall hydrogen release capacity of NaAlH$_4$ is 5.6 wt.%. Therefore, it is a suitable candidate material for small scale energy applications. However, in NaAlH$_4$ H-

atoms are strongly bonded with the Al-atom in a tetrahedron, Al-atom is placed at the tetrahedron center. The strong covalent bonding between the Al-atom and the H-atom makes hydrogen release possible only at higher temperatures. In addition to this, the dehydrogenation reactions proceed with very sluggish kinetics. High dissociation temperatures and slow reaction kinetics are the two significant challenges that inhibit the realization of alanates' practical applications.

Alanates have attracted much research attention in the recent past due to their lightweight and high hydrogen storage capacity [29, 33, 34, 30]. With decades of extensive research, several methods have been found to improve the hydrogen release environmental conditions and the reaction kinetics [50, 43, 51, 45, 52, 44, 53, 47, 146]. One such way is using the appropriate catalysts. The release of hydrogen from such materials at moderate temperatures is possible only in the presence of an apt catalyst. Transition metal(TM) atoms have partially filled d-orbitals in the valence shell. Therefore, they tend to attract more and more hydrogen atoms [147, 148, 24]. As a result, the bond between Al-atoms and H-atoms slackens [27, 43, 44, 45, 46, 47, 48, 49]. Various TM atoms have been explored for their catalytic activity in the past. However, understanding the mechanism of dehydrogenation at the microscopic level is equally important.

It is usually believed that the hydrogen-related defects, viz., hydrogen-vacancy, and hydrogen-interstitial defects play a vital role in the catalyzed dehydrogenation mechanism of $NaAlH_4$ [53, 42, 47]. Therefore, it is crucial to determine the most prominent H-related defects in the system. The most stable defects under the given circumstances are the majorly present defects. In the theoretical studies, the defects' relative stability is determined from the formation energy of the respective defects. However, the formation energies calculated from the DFT methodology [112] provides insights that are valid only at 0 K temperature. The material is operational at room temperature and moderately higher temperatures. To capture the most stable defect configuration at the operating environmental conditions, the inclusion of the effects of temperature and partial pressure

of hydrogen into the formation energy calculations is vital [149].

This chapter has emphasized the role of temperature and pressure on the relative stability of the charged H-related defects in the bulk NaAlH$_4$. We have duly added the effects of temperature and pressure with the methods of *ab initio* thermodynamics. We have shown that the most stable defect configurations change significantly with the inclusion of environmental effects. DFT alone gives the incorrect stable defect states at the operational temperature conditions for such materials. The inclusion of thermodynamic parameters is necessary to capture the stability of defects in such materials. Further, we have theoretically investigated the role of various TM atoms on the dehydrogenation mechanism of NaAlH$_4$. We have thoroughly studied the dehydrogenation mechanism, thereby sorting out the most appropriate dopant atoms to enhance the dehydrogenation reaction conditions.

3.1 Formation energy of defects

The vacancy and interstitial defects are induced in the bulk 96-atom supercell of NaAlH$_4$, i.e., Na$_{16}$Al$_{16}$H$_{64}$. The supercell size is chosen to minimize the defect-defect interactions due to the crystal structure's periodic nature. The supercell size is increased until the defect is stabilized, and there is no interaction of the defect with its periodic image. The formation energy of a charged defect can be calculated from the following expressions [150, 151]:

The formation energy for the hydrogen-vacancy $[V_H]^q$ defect:

$$E([V_H]^q) = E[(Na_{16}Al_{16}H_{63})]^q - E[(Na_{16}Al_{16}H_{64})]^0 + \frac{1}{2}E_{H_2} + q(\mu_e + VBM + \Delta) \quad (3.1)$$

The formation energy for the hydrogen-interstitial $[I_H]^q$ defect:

$$E([I_H]^q) = E[(Na_{16}Al_{16}H_{65})]^q - E[(Na_{16}Al_{16}H_{64})]^0 - \frac{1}{2}E_{H_2} + q(\mu_e + VBM + \Delta) \quad (3.2)$$

The first two terms in the right-hand sides of Eq. 3.1 and Eq. 3.2 represent the differences in the ground state energies of the defected supercell and the pristine supercell. E_{H_2} is the ground state energy of H_2 molecule. q is the charge on the system. μ_e is the chemical potential of an electron. It is also called the defect charging energy, i.e., the energy required to induce a charge into the system. VBM is the valence band maximum, and ΔV represents a difference in core levels of the defected and pristine supercells. The relative stability of various defect configurations, viz. $[V_H]^{-1,0,+1}$ and $[I_H]^{-1,0,+1}$ via formation energy calculations. The formation energy of these defect states is plotted as a function of μ_e, which is varied within the bandgap of the material from valence band maximum (VBM) to conduction band minimum (CBm). Figure 3.1 shows the plot of formation energy ΔG Vs μ_e. It is clear from the plot that the neutral defects have formation energy,
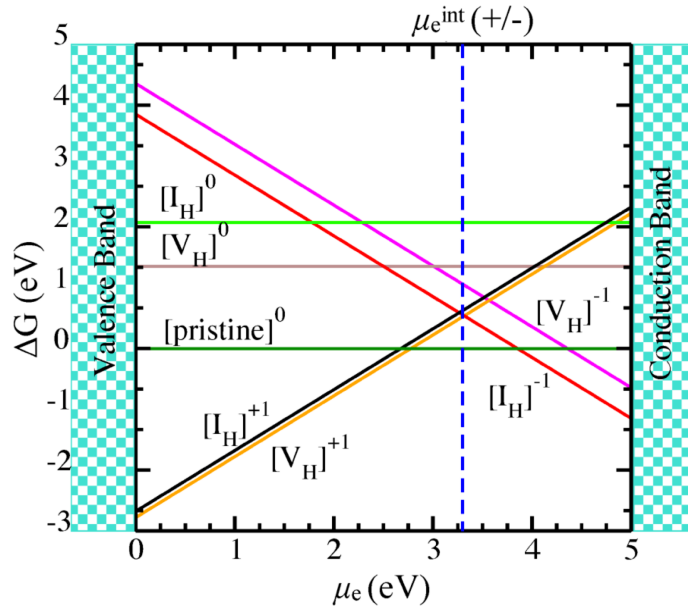
Figure 3.1: The plot representing formation energy of charged H-related defects as a function of chemical potential of electron, μ_e. μ_e is varied from valence band maximum(VBM) to conduction band minimum (CBm) within the band gap of NaAlH$_4$. The vertical dashed line represents the intrinsic transition state.

$\Delta G > 0$. Therefore, neutral defects are not stable in the bulk of NaAlH$_4$. However, the positively charged defects are stable near the valence band, and the negatively charged

defects are stable near the conduction band. $[V_H]^{+1}$ is the most stable defect state near
the valence band, whereas $[I_H]^{-1}$ is the most stable defect state near the conduction band.

Transition state: The value of μ_e at which the positive and negative defects have similar
formation energy is called the transition state. It is often termed as the intrinsic Fermi
energy. In Figure 3.1 the dashed vertical line represents Fermi level. The presence of ex-
trinsic defects in the system change value Fermi level. The n-type extrinsic point defects
shift the value of μ_e^{int} toward conduction band whereas the p-type defects shift μ_e^{int} value
toward valence band.

3.2 *Ab-initio* thermodynamics

The formation energies in the plot shown in Figure 3.1 are calculated from DFT. Hence,
it is correct only at 0 K. To understand the stability trend of the defect states at real
experimental conditions, we have incorporated the temperature and pressure-dependent
terms in the above expressions with the help of *ab initio* thermodynamics. The expression
of defect states' formation energy with the inclusion of *ab initio* thermodynamics on top
of DFT calculations is given in Eq. 3.3 [150, 151, 152]:

$$\Delta G(T, p_{H_2}) = \Delta E_f(T) - \frac{x}{2}\mu_{H_2}(T, p_{H_2}) + q(\mu_e + \text{VBM} + \Delta) \tag{3.3}$$

Here, ΔG is written as a function of temperature and partial pressure of hydrogen.
$\Delta E_f(T)$ is the difference in free energies of the defected and pristine supercells. The
free energy at temperature T is obtained by adding lattice vibration energy (phonons) to
the DFT energy.

$$\Delta E_f(T) = [F(T)_{\text{defected}}]^q - [F(T)_{\text{pristine}}]^0 \tag{3.4}$$

$$F(T) = F(T)^{\text{phonon}} + E^{\text{DFT}} \tag{3.5}$$

$F(T)^{\text{phonon}}$ is the energy of lattice vibrations or phonons, calculated from the package PHONOPY for the 96-atom supercells. The energy of phonon is written as [153]:

$$F(T)^{\text{phonon}} = \frac{1}{2}\sum_i h\nu_i + k_B T \sum_i \ln\left[1 - \exp\left[-\frac{h\nu_i}{k_B T}\right]\right] \tag{3.6}$$

In the second term in Eq. 3.3, x represents the type of the defect. For $[I_H]^q$ defects, x equals -1 whereas for $[V_H]^q$, x equals +1. $\mu_{H_2}(T, p_{H_2})$ represents the chemical potential of hydrogen which is written as a function of temperature, T and partial pressure p_{H_2}. μ_{H_2} is obtained by adding the tempertaure and pressure dependent terms, viz. translational kinetic energy, rotational kinetic energy, and vibrational free energy to the ground state energy. The expression of $\mu_{H_2}(T, p_{H_2})$ is expressed as [152]:

$$\begin{aligned}
\mu_{H_2}(T, p_{H_2}) = &-k_B T \ln\left[\left(\frac{2\pi m}{h^2}\right)^{\frac{3}{2}}(k_B T)^{\frac{5}{2}}\right] + k_B T \ln p_{H_2} - k_B T \ln\left[\frac{8\pi^2 I k_B T}{h^2}\right] \\
&+ \frac{h\nu_{HH}}{2} + k_B T \ln\left[1 - \exp\left[-\frac{h\nu_{HH}}{k_B T}\right]\right] + E^{\text{DFT}}(H_2) - k_B T \ln J + k_B T \ln \sigma
\end{aligned} \tag{3.7}$$

Here, K_B, h, m, and I respectively the Boltzmann constant, Planck's constant, the mass of the H_2 molecule, and moment of inertia of the H_2 molecule. ν_{HH} is the vibrational frequency of H-H the bond. The first two terms combined represent the translational kinetic energy; the second term represents the rotational kinetic energy; the third and fourth terms combined are the vibrational energy for the H_2 molecule. $\frac{h\nu_{HH}}{2}$ represents the zero-point energy of vibration. $E^{\text{DFT}}(H_2)$ is the ground state energy calculated from DFT.

3.3   Effect of environment on the stability of defects

The Figure 3.2 shows the plot of formation energy of charged H-related defects as a function of μ_e at 0 K and 300 K. The plot at 0 K is also shown in Figure 3.1. Here, it
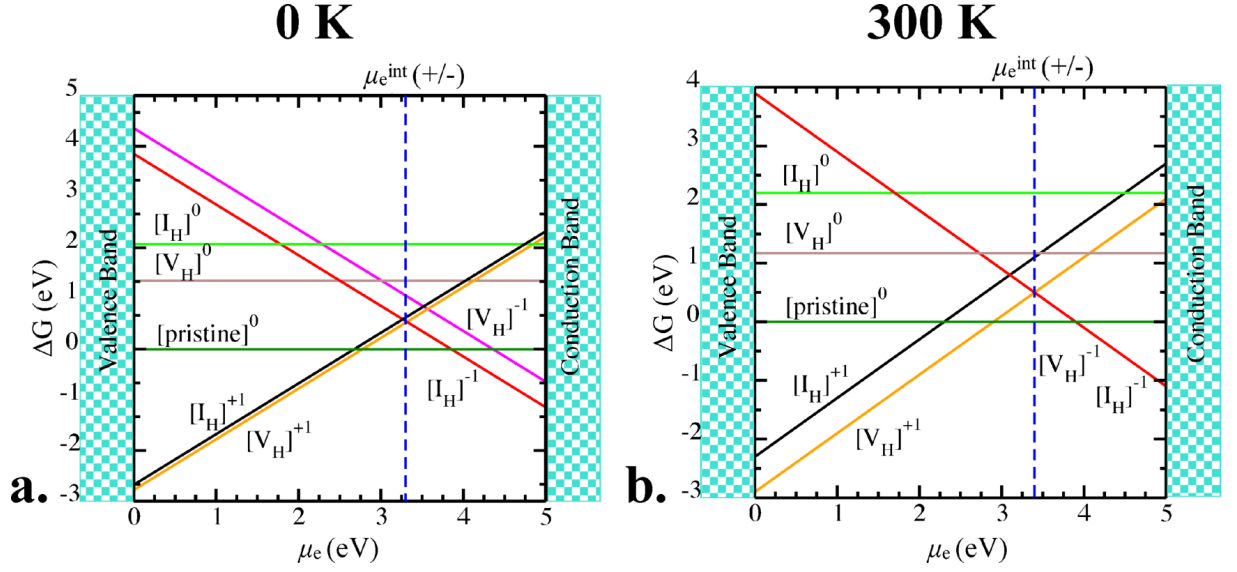
Figure 3.2: The variation of formation energy of charged H-related defects at (a.) 0 k and (b.) 300 K with μ_e.

is shown to clearly analyse the effect of temperature on the stable defect states. At 0 K, $[I_H]^{-1}$ is the most stable defect configuration. However, if the temperature is increased to 300 K, the two defect states, viz. $[I_H]^{-1}$ and $[V_H]^{-1}$ have exactly the same formation energies for all the values of μ_e. Therefore, the stability of defects depend highly on the environmental conditions.

3.3.1   Phase diagrams

To analyze the effect of temperature T and pressure p_{H_2} simultaneously, we have plotted the 3-dimensional phase diagrams at various temperatures. In Figure 3.3, 3-dimensional phase plots are shown at temperatures 50 k, 200 K, 300 K, and 400 K. On x-axis, $\Delta\mu_H$ values are varied in accordance with the p_{H_2} values ranging from 10^{-5} to 1 atm at a given temperature T. On y-axis, μ_e is varied from VBM to CBm. On the z-axis, ΔG values for the defects are plotted. Note that here we have shown the 2-dimensional projections of the 3-dimensional phase diagrams. Therefore, only the most negative values of ΔG (which correspond to the most stable defects) are visible. At 50 K temperature $[I_H]^{-1}$
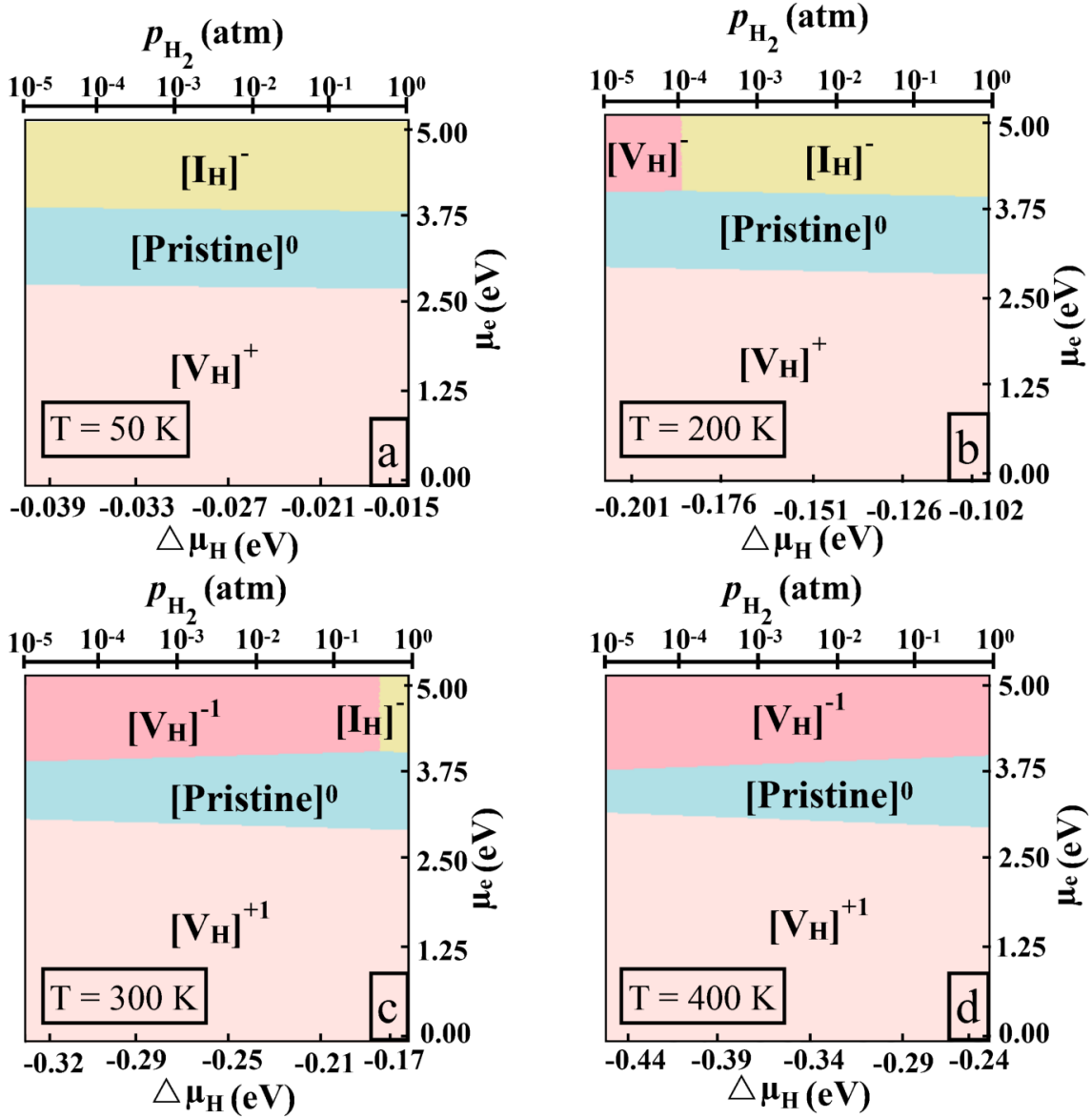
Figure 3.3: 3-D Phase diagrams representing the stability of defect configurations at 50 K, 200 K, 300 K, and 400 K. $\Delta\mu_H$ represents the chemical potential of hydrogen, which is varied according to partial pressure of hydrogen values and shown on the x-axis. On the y-axis, chemical potential of electron (μ_e) values are shown, which are varied from VBM to CBm. On the z-axis, the values of formation energy (ΔG) of defects is obtained. We have shown the projections of most negative values of ΔG on the x-y plane. The colored regions shown represent the most stable defect configurations.

is the most stable defect state at μ_e values near conduction band, for all the values of p_{H_2}. However, as the temperature is increased to 200 K, the $[V_H]^{-1}$ defect state becomes

the most stable for some values of p_{H_2}. When the temperature is raised to 400 K, the stable defect configurations change. $[V_H]^{-1}$ is the most stable defect configuration at all the values of p_{H_2}. This shows that the predicted defect states change drastically on the inclusion of temperature and pressure terms in the formation energy calculations.

3.3.2 Concentration of defects
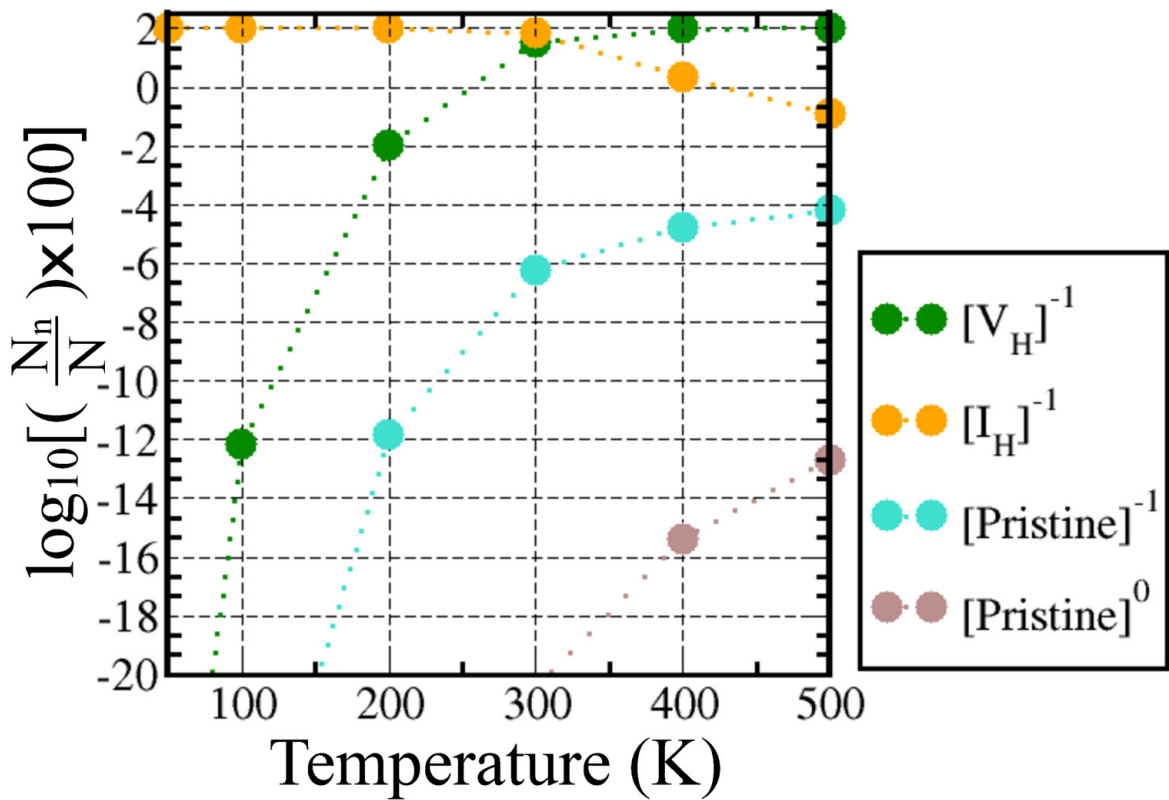
Figure 3.4: Logarithm of percentage concentration of defects plotted as a function of temperature.

To further validate our findings, we have calculated the concentration of H-related defects in the bulk of NaAlH$_4$ supercells. Due to the large size of the supercells, there are no interactions among the defects' periodic images. Therefore, defects can be assumed to follow Fermi-Dirac statistics [154, 150]. For N number of total defect sites, let us assume

that there are N_n number of one type of the defect with ΔG_n formation energy and N_m number of another type of the defect with ΔG_n formation energy are present in the lattice. Using Fermi-Dirac statistics, we can write:

$$
\begin{aligned}
N_n &= (N - \Sigma_{n \neq k} N_k)\frac{1}{1 + \exp[\frac{\Delta G_n}{k_B T}]} \\
N_m &= (N - \Sigma_{m \neq k} N_k)\frac{1}{1 + \exp[\frac{\Delta G_m}{k_B T}]}
\end{aligned}
\tag{3.8}
$$

Combining the above two equation, we get:

$$
\frac{N_n}{N_m} = \exp\left[\frac{\Delta G_m - \Delta G_n}{k_B T}\right]
\tag{3.9}
$$

Rearranging the terms in above equation, the concentration of any one type of defect can be written as:

$$
C_n = \frac{N_n}{N} = \frac{\exp[-\frac{\Delta G_n}{k_B T}]}{1 + \Sigma_m \exp[-\frac{\Delta G_m}{k_B T}]}
\tag{3.10}
$$

Fig 3.4 shows the variation of defect concentration as a function of temperature at a fixed p_{H_2} value, i.e., 1 atm. The concentration of defects changes significantly with the increase in temperature. From 0 K to 300 K, $[I_H]^{-1}$ has the maximum concentration, whereas, above 300 K $[V_H]^{-1}$ has the maximum concentration. Therefore, the concentration of defects exhibits the same trend as stability.

3.4   Transition metal atom doping

Transition metal atoms are the most appropriate catalysts for the enhancement of dehydrogenation reaction conditions in the alanates. TM atoms have partially filled d-orbitals, due to which they tend to loosen the strong Al-H bonds in the alanates; thus, they facilitate dehydrogenation mechanism [155, 24, 147]. To study the catalytic effects of TM

atoms in NaAlH$_4$, we have doped various TM atoms (Ti, Sc, Cd, Zn, Ni, and Pd) in the bulk of NaAlH$_4$. The selection of the most suitable TM atom dopant depends mainly on three factors. First, the dopant's stability at the chosen site is an important factor, which determines the possibility of inducing the defect at realistic experimental conditions. The stability of a dopant is estimated from the defect formation energy calculations. This also gives insights on the appropriate defect configurations for a given dopant, i.e., the preferred lattice site and the charge state. Second, the catalytic activity depends on the ability of the TM atom to loosen the Al-H bonds; however, the TM-H bonds should not be strong to ensure the easy release of the hydrogen. Third, change in the formation energy of the intrinsic defects in the presence of dopants. It is usually believed that the mechanism of catalyzed dehydrogenation reaction involves the self-diffusion of the intrinsic defects, such as $[I_H]^q$ and $[V_H]^q$ [49, 45, 47]. The self-diffusion of a defect depends on its concentration, which is directly related to the defect's stability in the material. Thus, the suitable TM atom dopants increase the intrinsic defects' stability by lowering their ΔG values. From Eq. 3.3 it is clear that ΔG is directly proportional to Fermi level. Therefore, the favorability of the dopant depends on the shift in Fermi level.

3.4.1 Stability of the dopants

We have doped various TM atoms, viz., Ti, Sc, Cd, Zn, Ni, and Pd, at two metallic sites in the material, i.e., Na and Al. The formation energy for the substitutional defect configurations, $[TM_{Na}]^q$ and $[TM_{Al}]^q$ in the 96-atom supercell Na$_{16}$Al$_{16}$H$_{64}$ is calculated from the following formulae:

$$[\Delta G(TM_{Na})]^q = [E(Na_{15}Al_{16}H_{64}TM)]^q - [E(Na_{16}Al_{16}H_{64})]^0$$
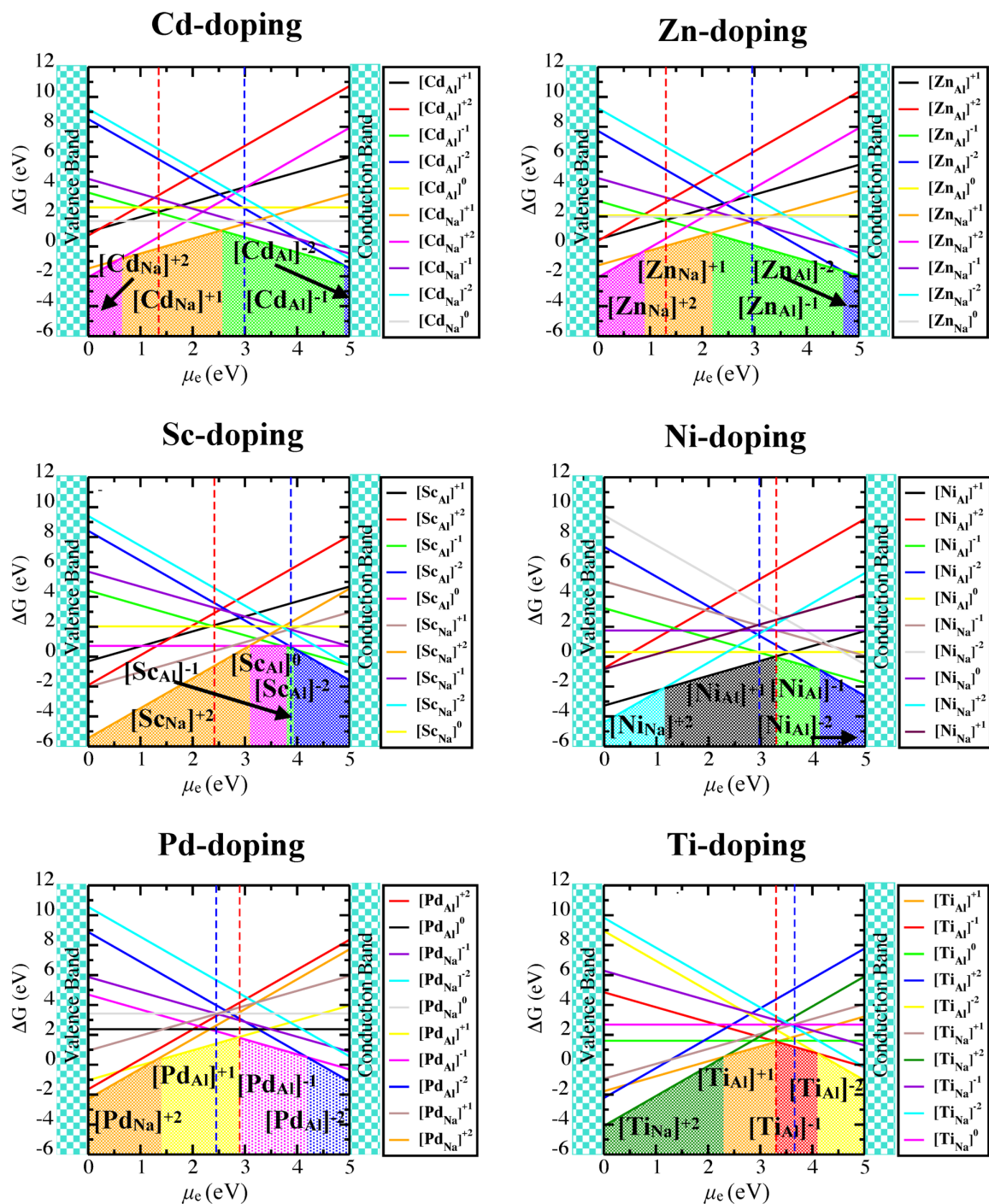$$+ E^{DFT}(Na) - E^{DFT}(TM) + q(\mu_e + VBM + \Delta)$$

(3.11)

Figure 3.5: The formation energy of Transition metal atom doping as a function of chemical potential of electron. Colored regions show the stable configurations for doping $[TM_{Na}]^q$ represents a TM atom repacing a Na-atom, whereas $[TM_{Al}]^q$ represents a Al atom replacing a Al-atom.

$$[\Delta G(TM_{Al})]^q = [E(Na_{16}Al_{15}H_{64}TM)]^q - [E(Na_{16}Al_{16}H_{64})]^0$$

$$+E^{DFT}(Al) - E^{DFT}(TM) + q(\mu_e + VBM + \Delta)$$

(3.12)

Here, $[E(Na_{15}Al_{16}H_{64}TM)]^q$ is the total energy of the 96-supercell where a TM atom is substituted at the site of Na-atom, whereas, $[E(Na_{16}Al_{15}H_{64}TM)]^q$ is the energy of the supercell with a TM atom sustituted at Al-site. $[E(Na_{16}Al_{16}H_{64})]^0$ is the total energy of the neutral pristine supercell. Thus, the first two terms in Eq. 3.11 and Eq. 3.12 represent the difference in the total energies of the defected and pristine supercells. $E^{DFT}(Na)$, $E^{DFT}(Al)$, and $E^{DFT}(TM)$ respectively are the DFT energies of the Na-atom, the Al-atom and the TM atom. The last term represents the energy of inducing charge. The formation energies for all the possible charged defect configurations is calculated and plotted as a function of chemical potential of electron μ_e which is varied from VBM to CBm. Figure 3.5 depicts the stability of various TM atoms at the lattice sites of Al-atom and Na-atom. The observed trend in the stability of different charged states of the doping can be explained based on electronic configurations of the TM atoms, Na-atom, and Al-atom. Cadmium (Cd) has the electronic configuration, $[Kr]4d^{10}5s^2$, it has fully filled 4d-orbital and has two electrons in the valence shell. Therefore, Cd's valence shell contains one more electron than that of Na and one less electron than that of Al. When Cd is substituted at Na-site, it becomes a donor level impurity and is expected to be stable in +1 charged state or in the neutral state, i.e., $[Cd_{Na}]^{+1}$ and $[Cd_{Na}]^0$. Whereas, if Cd replaces Al, it behaves like an acceptor impurity and is expected to be stable in -1 charged state or in the neutral state, i.e., $[Cd_{Al}]^{-1}$ and $[Cd_{Al}]^0$. This explains the stability of the charged defect configurations $[Cd_{Na}]^{+1}$ near valence band and $[Cd_{Al}]^{-1}$ near conduction band in the system. The electronic configuration of zinc (Zn) is $[Ar]\,3d^{10}\,4s^2$. Therefore, like Cd, Zn has two valence electrons ahead of a fully filled d-orbital. Zn behaves as a donor impurity and is stable in the +1 charged state when replacing Na. While it behaves as an acceptor impurity, stable in the -1 charged state when replacing Al. Hence, $[Zn_{Na}]^{+1}$ is the most stable defect state near valence band, whereas, $[Zn_{Al}]^{-1}$ is the most stable defect state near

conduction band. The electronic configuration of scandium (Sc) is $[Ar]3d^14s^2$. It is clear that Sc has two more electrons than Na in the valence shell. Therefore, $[Sc_{Na}]^{+2}$ is the most favorable defect state near valence band. Sc has the same number of electrons as Al in the valence shell. This clearly explains the favorability of $[Sc_{Al}]^0$ state. However, here we observe that various charged states are stable depending on the value of μ_e. Similar is the case with Nickel (Ni) having electronic configuration $[Ar]3d^84s^2$, Palladium (Pd: electronic configuration $[Kr]4d^{10}$), and Titanium (Ti: electronic configuration $[Ar]3d^24s^2$). This situation arises when the dopant atom exhibits multiple valencies.

3.4.2   Structural distortion due to doping
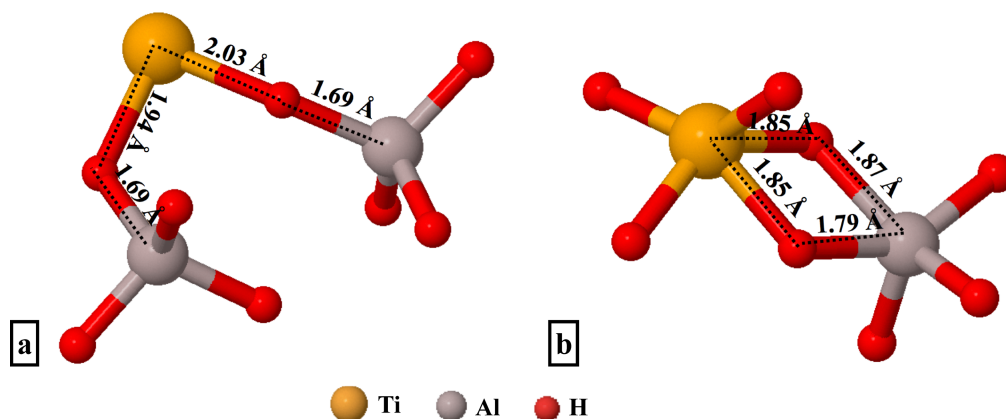
Figure 3.6: Distortion created in the geometry of the alanate by the dopant TM atoms at (a.) Na-site and (b.) Al-site.

Figure 3.6 represents the elongated bond lengths for Al-H bonds after doping with Ti-atom at the site of Na-atom and Al-atom.

TM atoms have partially filled d-orbitals due to which they tend to make bonds with the H-atoms, which results in the loosening of the Al-H bonds and easy release of hydrogen. The average equilibrium bond length of the Al-H bonds in $NaAlH_4$ is 1.64 Å. Doping with TM atoms increases this bond length. We have shown the Al-H and TM-H bond lengths after doping in the Table 3.1. The distortion in the Al-H bonds depends highly on the

electronic configurations of the TM dopants. For the case of Zn and Cd, the structure is
not distorted at all, and there is negligible interaction between dopant and the H-atom. A
reasonable explanation for this may be that Cd and Zn atoms have fully filled d-orbitals
in their valence shells; thus, there is no share of electrons possible with the other atoms.
Hence, there is no interaction, and the geometry remains undistorted even after doping.

Type of dopants	Bond length (Å)	
	Al-H	**TM-H**
Cd_{Al}	1.65	1.79
Cd_{Na}	1.65	2.46
Zn_{Al}	1.65	1.62
Zn_{Na}	1.65	2.40
Sc_{Al}	1.65	1.92
Sc_{Na}	1.70	2.09
Ni_{Al}	1.81	1.51
Ni_{Na}	1.72	1.75
Pd_{Al}	1.65	1.63
Pd_{Na}	1.72	1.86
Ti_{Al}	1.79	1.84
Ti_{Na}	1.69	1.94

Table 3.1: Table of bond lengths for the bonds between Al and H as well as for the bonds
between TM and H after doping.

3.4.3 Shift in the transition state $\epsilon(+/-)$ due to the presence of TM dopants

Charge neutrality condition: the charge-neutrality condition governs the concentration of charged defects in a system

$$\sum_i q_i \times C_i - n_e + n_h = 0 \tag{3.13}$$

Here, q_i and C_i respectively denote the charge and concentration of ith defect, thus $\sum_i q_i \times C_i$ is the total charge induced in the system due to all defects. n_e and n_h respectively

Type of dopants	$\Delta\mu_e$ (eV)	
	T=0 K	T=300 K
Cd_{Al}	-1.99	-2.07
Cd_{Na}	-0.30	-0.38
Zn_{Al}	-2.02	-2.10
Zn_{Na}	-0.38	-0.46
Sc_{Al}	-0.97	-1.05
Sc_{Na}	0.54	0.46
Ni_{Al}	-0.05	-0.13
Ni_{Na}	-0.37	-0.45
Pd_{Al}	-0.43	-0.51
Pd_{Na}	-0.83	-0.91
Ti_{Al}	0.00	-0.08
Ti_{Na}	0.27	0.19

Table 3.2: Table of $\Delta\mu_e = \epsilon(+/-) - \mu_e^{int}$ in (eV) values at temperatures 0 K and 300 K for various doping configurations. TM_{Al} and TM_{Na} denote TM doped at position of Al and Na respectively where TM = Cd, Zn, Sc, Ni, Pd, Ti.

represent the concentration of free electrons in the conduction band and free holes in the valence band. $NaAlH_4$ is a wide bandgap material. In wide bandgap materials, the concentration of free electrons and holes is nearly zero, i.e., $n_e = n_h \simeq 0$. Therefore, to fulfill the charge neutrality condition, defects with opposite charges are induced in a system. That is why the energy levels corresponding to the defect states are found within the bandgap region.

Transition state: The transition state is defined as Fermi energy's position (or chemical potential of the electron) where the most stable positive and negative defect states have the same ΔG values. When there are no extrinsic defects in the system, the transition state is determined from the intrinsic defects, i.e., $[V_H]^q$ and $[I_H]^q$ defects. It is denoted by the symbol $\mu_e^{int}(+/-)$. In Figure 3.2, $\mu_e^{int}(+/-)$ are shown by the dashed vertical lines. At 0 K the value of $\mu_e^{int}(+/-)$ is 3.32 eV, whereas at 300 K the value shifts to 3.40 eV. Inducing extrinsic defects, such as dopants, in the system shifts the value of the transition state (μ_e) either toward the valence band or toward the conduction band. It is clear from

Eq. 3.1 and Eq. 3.2 that the formation energy of intrinsic H-related defects is directly
proportional to μ_e. Hence, the presence of dopants affects the stability of H-related
defects. The dopants that shift the value of μ_e more toward the right decrease the ΔG
values for the H-related defects, hence increase the stability of the defect. As mentioned
earlier, the dehydrogenation process depends on the diffusion of H-related defects, the
defects with more concentration diffuse more through the system. The concentration of
the defects is, in turn, dependent on its stability. Therefore, the dopants that lower H-
related defects' formation energy by shifting the value of μ_e toward the right are considered
the suitable dopants for improving the hydrogen desorption kinetics of the given material.
We have shown the shift in transition states, i.e., $\Delta\mu_e = \epsilon(+/-) - \mu_e^{int}$ at 0 K and 300 K
temperatures for all the doping configurations in Table 3.2.

Based on the three factors discussed above, we infer that Ti and Sc are the most suitable
dopants for enhancing the hydrogen desorption kinetics and dissociation temperature
conditions in $NaAlH_4$.

Here, we can conclude that the environmental condition, i.e., temperature and pressure,
have an indispensable effect on the relative stability of the H-related defects in complex
metal hydrides. Ti and Sc are the most suitable dopants for improving the reaction
kinetics in $NaAlH_4$.

Chapter 4

Electrochemical reduction of CO_2 to CO

Introduction

With the continuous exploitation of fossil fuels for more than a century, the CO_2 content in the atmosphere has reached a dangerous level. Global warming and other extreme weather events due to climate change result from increased CO_2 concentration. Therefore, it has become essential to take the necessary step toward lowering the amount of greenhouse gas [156, 157, 54, 158].

The chemical reduction of CO_2 to other vital industrial products is considered a promising way of reducing the CO_2 content while producing useful industrial feedstocks [54, 57, 19, 20, 58, 55]. In the electrochemical reduction (ECR) process, the reaction's product depends on the electrolyte and electrode materials. Therefore, it is a simple process where the final product's flexibility is achieved with little effort [54, 55, 56, 57]. The ECR of CO_2 is carried out in a two-chamber electrochemical cell, where the cathode and anode materials are kept immersed in the electrolyte material. The reduction of CO_2 and evolution of CO occurs on the surface of the cathode material. Thus, the cathode

acts as an electrocatalyst. CO_2 molecule is thermodynamically very stable; therefore, the reduction of CO_2 requires very high efficiency of the electrocatalyst. Besides, the reduction potential of hydrogen evolution reaction (HER) is similar to the ECR of CO_2 to CO. The electrocatalyst must also exhibit a high product selectivity. The significant challenges in applying an electrocatalyst to practical applications are achieving high Faradaic efficiency and high product selectivity [59, 65, 21, 60]. It has been suggested in the past that alloys of Cu with Pd, In, and Sn exhibit significant Faradaic efficiency [61, 62, 63, 64]. Experimentally, it is found that the Cu-In-O nanocomposites exhibit much improved Faradaic efficiency and suppress the competing HER, thereby show excellent product selectivity. It is found that the point defects, i.e., oxygen-vacancies, play a vital role in enhancing the catalytic activity of the Cu-In-O nanocomposites.

In this chapter, We validate the experimental findings from the DFT calculations. We first model the Cu-In-O systems with the cascade genetic algorithm techniques [139] to depict the experimentally synthesized materials. We then find out the most suitable site for the evolution of CO to understand the mechanism of ECR on the surface of the electrocatalyst. Next, we find out the reaction enthalpy with DFT energy calculations for different concentrations of V_O defects. Finally, we theoretically confirm the high selectivity of the electrocatalyst material due to the presence of In-atoms.

4.1   Stable structures

We use the cascade genetic algorithm to find out the minimum energy structures from a wide range of clusters $Cu_xIn_yO_z$. x and y are varied according to the experimental compositions of Cu and In atoms. For 90% Cu, 10% In; 80% Cu, 20% In; and 70% Cu, 30% In compositions and the cluster compositions respectively are $Cu_{19}In_1$; $Cu_{18}In_2$; and $Cu_{17}In_3$. To determine the stable structures in the environment of oxygen, the number of oxygen-atoms, z, is optimized to the maximum number that can be accommodated in
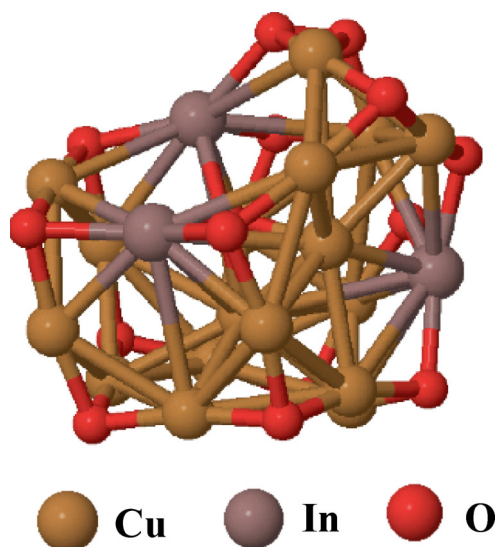
Figure 4.1: Minimum energy configuration for $Cu_{17}In_3O_{15}$ cluster depicting the 70% Cu, 30% In composition.

the clusters. Figure 4.1 represents the stable structure for $Cu_{17}In_3O_{15}$ obtained after the energy minimisation through cascade genetic algorithm.

4.2 Mechanism of electrochemical reduction (ECR)

The elementary steps involved in the ECR of CO_2 to CO on the surface of the electrocatalyst are as follows [19, 20, 58]:

Firstly, the molecule of CO_2 gets adsorbed on the electrocatalyst's surface and the linear molecule of CO_2 bends.

Secondly, it accepts an electron and a proton to form an intermediate compound, COOH*.

$$CO_2^* + H^+ + e^- \rightarrow COOH^* \tag{4.1}$$

The reaction is energy-intensive. The enthalpy of formation of the intermediate compound is referred to as the energy barrier for the process of ECR.

In the next step, COOH* accepts one more pair of an electron and a proton to dissociate

into CO and H$_2$O.

$$COOH^* + H^+ + e^- \rightarrow CO + H_2O \tag{4.2}$$
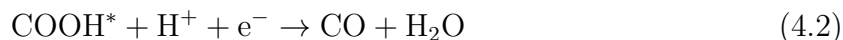
Finally, the CO molecule evolves from the surface of the electrocatalyst.

To theoretically understand the mechanism of formation of CO from CO$_2$ and to investigate the role of defects on the catalytic activity of the nanocomposite, we have induced various point defects, viz., oxygen-vacancy (V$_O$), copper-vacancy (V$_{Cu}$), and one (V$_O$) with one (V$_{Cu}$) defects.

4.3   Favorable site for CO evolution
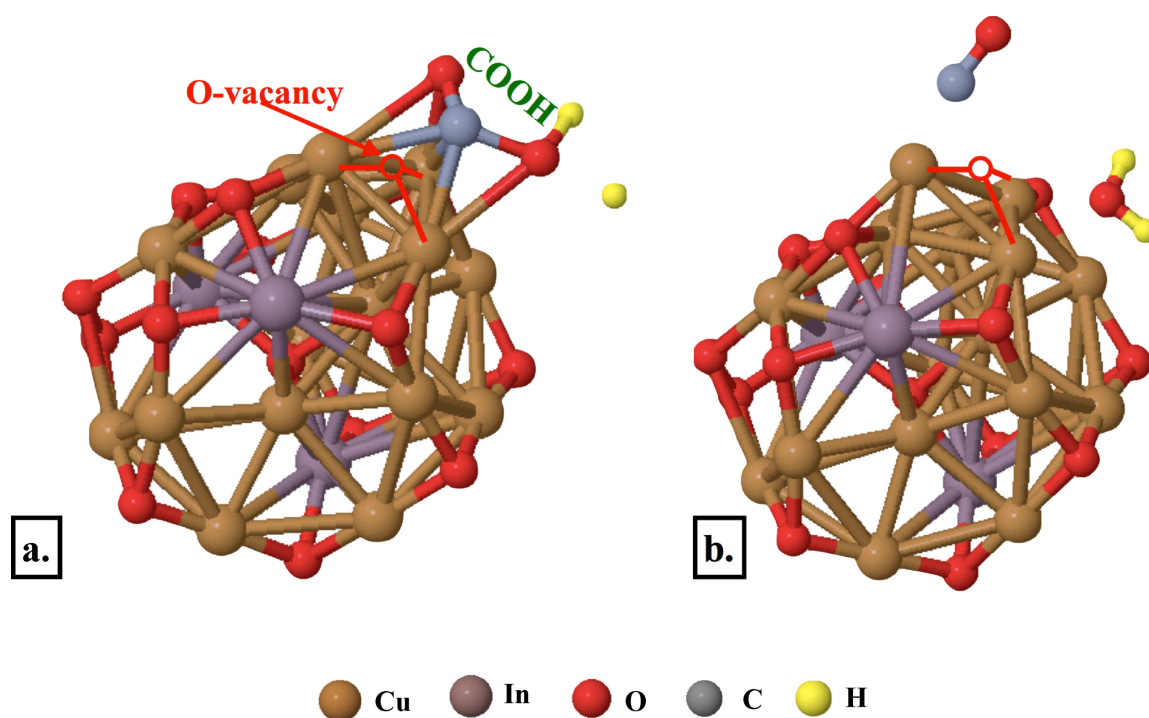
Figure 4.2: Cu$_{17}$In$_3$O$_{15}$ clusters with (a.) COOH adsorbed on the site of V$_O$ defect before optimization, and (b.) CO and H$_2$O desorbed from the cluster after optimization.

The dissociation of COOH into CO and H$_2$O is an exothermic process. It occurs spontaneously in the presence of an H-atom. To determine the favorable site for the evolution of the final product of the ECR, we adsorb COOH group along with H-atom at various

sites, viz., Cu, In, O, V_O, and V_{Cu}. We find that the CO molecules are formed only in the vicinity of V_O defects. The same is depicted in Figure 4.2.

Figure 4.2a represents the adsorption of COOH on the surface of $Cu_{17}In_3O_{15}$ clusters near the V_O defect site. Figure 4.2b represents the formation of CO and H_2O molecules at the preferred site, i.e., V_O-site after the optimization.

In addition to this, we observe that pristine Cu-In-O composites and the one with V_{Cu} defects fail to catalyze the formation of CO. Therefore, we conclude that V_O defects are crucial for the catalytic activity of the Cu-In-O electrocatalysts.

Figure 4.3: Reaction enthalpies for the ECR process on top of $Cu_{17}In_3O_{15}$ cluster with (a.) one V_O defect and (b.) two V_O defects.

4.4 Enthalpy of reaction in the presence of oxygen vacancies

As mentioned earlier, the process of ECR proceeds with two main steps. The first step, i.e., the formation of -COOH compound is an endothermic process; the reaction enthalpy of this step determines the ECR proce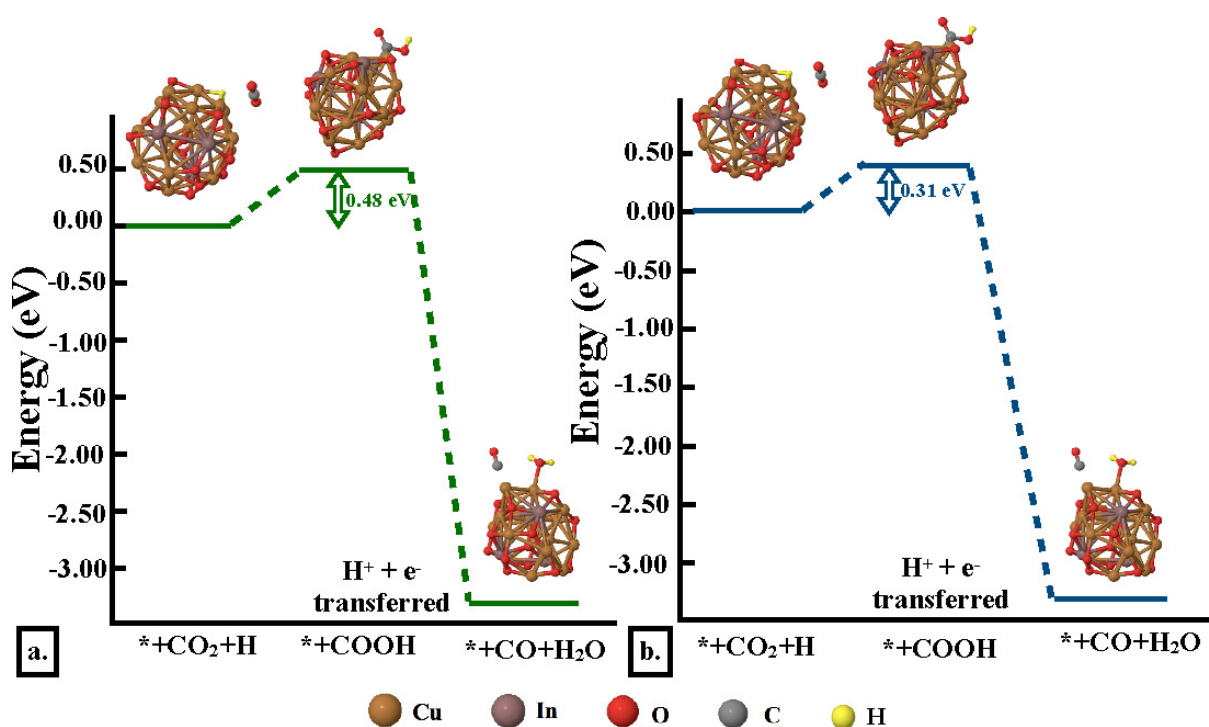ss's ease. To confirm the role of V_O defects in enhancing the catalytic activity of the nanocomposite, we determine the reaction enthalpy for the formation of COOH on the surface of $Cu_{17}In_3O_{15}$ clusters with one and two V_O defects.

Figure 4.3 shows the reaction mechanism along with the reaction enthalpy for the ECR process on the $Cu_{17}In_3O_{15}$ clusters with one and two V_O defects. We find that the reaction enthalpy for forming an intermediate compound, COOH, is 0.48 eV in the case of one V_O defect, whereas the value of reaction enthalpy decreases to 0.31 eV when there are two V_O defects present in the cluster. The decrease in reaction enthalpy with the increase in oxygen vacancies concentration ensures that the high catalytic activity of Cu-In-O nanocomposites is primarily due to V_O defects. The lower value of the reaction enthalpy in the case of two V_O defects is attributed to the extra electrons added to the clusters due to the vacancies, which facilitate the process of COOH formation, hence, energetically simplifies the whole process of ECR.

## 4.5 Role of In-atoms in supressing the hydrogen evolution reaction

Similar reduction potential of ECR and HER

By definition, the reduction potential is the amount of energy released/absorbed when an element gains/loses one electron.

Hydrogen evolution reaction (HER) can be written as:

$2H^+ + 2e^- \rightarrow H_2$

Theoretically, the reduction potential of the above reaction can be calculated from the difference in Gibb's free energies of H_2 molecule and 2 H^+-ions plus 2 electrons. The standard value of the reduction potential of the HER is -0.0 V (vs. SHE) [159]. On the other hand, the standard potential for the Electrochemical Reduction (ECR) of CO_2 to CO:

$CO_2 + 2H^+ + 2e^- \rightarrow CO + H_2O$ is -0.1 V (vs. SHE) [160].
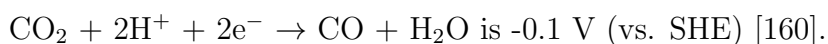
Therefore, we can say that the reduction potential of ECR and HER are nearly similar; hence, HER is a competetive reaction. We adsorb H-atom on the Cu-site and In-site, in the $Cu_{17}In_3O_{15}$ cluster to explain the high selectivity of the proposed nanocomposite. We find that the adsorption enthalpy for a single H-atom on the Cu-site is 0.93 eV. In comparison, the adsorption of an H-atom on the In-site requires 1.77 eV energy. Therefore, the HER process is expected to be much more difficult on the In-site than the Cu-site. Hence, the suppression of the competing HER process is mainly due to In-atoms' presence in the system. Hence, we can conclude that the presence of In-atoms in the system leads to the HER's suppression. Hence, it enhances the product selectivity of the Cu-In-O nanocomposites.

Hence, we can conclude that the Cu-In-O nanocomposites' high catalytic activity is largely because of the presence of oxygen vacancies in the system. Whereas, the high selectivity of the proposed nanocomposites is mainly due to the In-atoms.

Chapter 5

Mechanical and diffusional properties of solid ionic conductors for all-solid-state batteries

Introduction

Solid-state Li-ion batteries are a promising technology for energy storage applications. There is a fear of thermal runaway and explosions in the conventional Li-ion batteries due to the flammable liquid electrolyte materials, which hinders their realization at a large scale [79, 22]. Solid electrolyte materials have numerous advantages over conventional liquid electrolyte materials. Solid electrolytes eliminate the risk of battery explosion and make the battery design compact [80, 81]. However, to employ a solid material for the electrolytic application has several challenges. Two significant challenges are to achieve mechanical stability [86] and high ionic conductivity [90, 91, 92].

The charging and discharging of an electrochemical cell involves the migration of ions from one electrode to the other via electrolyte material. In a Li-ion cell, Li-ions are the mobile ions, which facilitate the cycling process. During charging, Li-ions move from cathode

to anode through the electrolyte; in this process, the Li-ions de-intercalate the cathode material and intercalates the anode material. As a result, the volumes of electrode materials change [161, 162, 163]. The electrolyte material must maintain physical contact with the expanding and contracting electrodes to ensure the cell's proper functioning. In the conventional liquid electrolyte case, there is no loss of contact between the electrolyte and the electrode. However, to replace the liquid electrolyte with a solid-state electrolyte material, maintaining physical contact is a significant challenge. The solid electrolyte exerts pressure on the expanding electrodes, which results in the fracturing of the electrode and the electrolyte material [163]. This leads to the formation of dendrites, which is the primary cause of shorter battery life. Therefore, the solid electrolyte material is expected to be mechanically fit to avoid such situations.

On the other hand, the current density of an electrochemical cell highly depends on Li-ion's movement through the electrolyte materials. Liquid electrolyte materials offer a less dense channel for the ions' flow; hence, they exhibit higher ionic conductivity. Whereas, in the case of solid electrolytes, to achieve a high ionic conductivity is another challenge. There are two major classes of candidate electrolyte materials, viz. oxides and sulfides. Sulfides exhibit much higher ionic conductivity than the oxide materials because of the high polarizability of the S^{2-} ions. In addition, sulfide electrolytes are more mechanically appropriate than oxide materials because of much softer Li-S bonds than Li-O bonds. In this chapter, we have calculated the mechanical properties of various sulfide materials, viz. Li_3PS_4, $Li_4P_2S_6$, $Li_{10}GeP_2S_{12}$, Li_6PS_5Cl, Li_6PS_5Br, and Li_6PS_5I. Further, we have investigated the role of halide doping in improving the mechanical properties of the materials. Next, we have compared the diffusional properties of the materials mentioned above to choose the most suitable material for the electrolytic applications. Finally, we have elucidated the role of point defects, i.e., Li-vacancy(V_{Li}) on such materials' ionic conductivity. Our results reveal that point defects play a vital role in enhancing the electrolyte materials' mechanical and diffusional properties.

5.1 Mechanical Properties

Mechanical properties are essential to determine the response of material toward external force. The electrolyte materials must be elastic enough toward the force exerted by expanding electrodes to prevent the fracturing and loss of contact. The most important mechanical properties are the formability and elastic moduli [84, 105]. The formability of a material is directly related to its ductility. The material should be ductile enough to ensure its formability and mechanical stability under given circumstances. The ductility is estimated from Pugh's criterion, which states that a material exhibits ductile behavior if the ratio of bulk modulus of elasticity to shear modulus of elasticity, B/G is greater than 1.75 else, the material is brittle [164]. Besides, the bulk and Young's moduli of elasticity are very crucial parameters to predict the elastic behavior of the material in contact with expanding and contacting electrode materials.

The elastic moduli can be determined from the coefficients of elasticity depending upon the crystal structure of the solid-state material. The coefficients of elasticity are constant of proportionality between the stress and the strain. As written in generalised Hook's law:

$$\sigma_{\text{ij}} = \sum_{\text{kl}} C_{\text{ijkl}} \epsilon_{kl} \tag{5.1}$$

In the tensor form, generalised Hook's law can be expressed as:

$$
\begin{bmatrix}
\sigma_{\text{xx}} & \sigma_{\text{xy}} & \sigma_{\text{xz}} \\
\sigma_{\text{yx}} & \sigma_{\text{yy}} & \sigma_{\text{yz}} \\
\sigma_{\text{zx}} & \sigma_{\text{zy}} & \sigma_{\text{zz}}
\end{bmatrix}
=
\begin{bmatrix}
C_{\text{xxxx}} & C_{\text{xxyy}} & C_{\text{xxzz}} & C_{\text{xxxz}} & C_{\text{xxyz}} & C_{\text{xxxy}} \\
C_{\text{yyxx}} & C_{\text{yyyy}} & C_{\text{yyzz}} & C_{\text{yyxz}} & C_{\text{yyyz}} & C_{\text{yyxy}} \\
C_{\text{zzxx}} & C_{\text{zzyy}} & C_{\text{zzzz}} & C_{\text{zzxz}} & C_{\text{zzyz}} & C_{\text{zzxy}} \\
C_{\text{xzxx}} & C_{\text{xzyy}} & C_{\text{xzzz}} & C_{\text{xzxz}} & C_{\text{xzyz}} & C_{\text{xzxy}} \\
C_{\text{yzxx}} & C_{\text{yzyy}} & C_{\text{yzzz}} & C_{\text{yzxz}} & C_{\text{yzyz}} & C_{\text{yzxy}} \\
C_{\text{xyxx}} & C_{\text{xyyy}} & C_{\text{xyzz}} & C_{\text{xyxz}} & C_{\text{xyyz}} & C_{\text{xyxy}}
\end{bmatrix}
\begin{bmatrix}
\epsilon_{\text{xx}} & \epsilon_{\text{xy}} & \epsilon_{\text{xz}} \\
\epsilon_{\text{yx}} & \epsilon_{\text{yy}} & \epsilon_{\text{yz}} \\
\epsilon_{\text{zx}} & \epsilon_{\text{zy}} & \epsilon_{\text{zz}}
\end{bmatrix}
\tag{5.2}
$$

Here, σ_{ij} and ϵ_{kl} respectively denote the second rank stress and strain tensors. The indices i, j, k, and l represent the x, y, and z-axes; the first index represents the axis normal to the plane that experiences the stress and the second index represents the direction of stress. The coefficient C_{ijkl} is a fourth rank tensor. The stress and strain tensors are symmetric, i.e., $\sigma_{ij} = \sigma_{ji}$ and $\epsilon_{kl} = \epsilon_{lk}$. As a result the nine elements of the tensors reduce to six elements. The indices for x,y, and z-axes are replaced by numarical indices with the help of Voigt notation: xx=1; yy=2; zz=3; xz=4; yz=5; and xy=6.

$$
\begin{bmatrix} \sigma_1 \\ \sigma_2 \\ \sigma_3 \\ \sigma_4 \\ \sigma_5 \\ \sigma_6 \end{bmatrix} = \begin{bmatrix} C_{11} & C_{12} & C_{13} & C_{14} & C_{15} & C_{16} \\ C_{21} & C_{22} & C_{23} & C_{24} & C_{25} & C_{26} \\ C_{31} & C_{32} & C_{33} & C_{34} & C_{35} & C_{36} \\ C_{41} & C_{42} & C_{43} & C_{44} & C_{45} & C_{46} \\ C_{51} & C_{52} & C_{53} & C_{54} & C_{55} & C_{56} \\ C_{61} & C_{62} & C_{63} & C_{64} & C_{65} & C_{66} \end{bmatrix} \begin{bmatrix} \epsilon_1 \\ \epsilon_2 \\ \epsilon_3 \\ \epsilon_4 \\ \epsilon_5 \\ \epsilon_6 \end{bmatrix}
\tag{5.3}
$$

Due to the symmetry, $C_{ij} = C_{ji}$, the number of independent elastic coefficients reduce from 36 to 21. The elastic coefficients can be determined from the above written equation via direct method within the framework of density functional theory. The number of independent coefficients further reduces due to the symmetry of the crystal structure. Further, elastic moduli are obtained from the coefficients depending upon the geometry of the crystalline system. Here, we have discussed the mechanical properties, viz., elastic moduli, and ductility of various materials based on their geometry. First, the elastic properties of Li_3PS_4 crystal that has orthorhombic geometry are discussed. Then, $Li_4P_2S_6$: hexagonal crystal structure is explained. Next, $Li_{10}GeP_2S_{12}$: tetragonal crystal structure and finally, Li_6PS_5X (X=Cl, Br, I): cubic crystal structures are explained.

5.1.1 Li_3PS_4: Orthorhombic crystal structure

Li_3PS_4 crystallizes into orthorhombic geometry when the composition is 25% Li_2S and
75% P_2S_5. For the orthorhombic crystal systems, the number of independent elastic
constants reduces to 9 because of the crystal structure's symmetry. The elastic constants,
viz. C_{11}, C_{22}, C_{33}, C_{44}, C_{55}, C_{66}, C_{12}, C_{13}, and C_{23} are sufficient to completely determine
the elastic properties of Li_3PS_4.

Table 5.1 shows the values of elastic constants for Li_3PS_4 crystal structure obtained using
the DFT calculations.

Elastic constants	Values in GPa
C_{11}	28.979
C_{22}	35.996
C_{33}	45.623
C_{44}	11.362
C_{55}	8.368
C_{66}	11.391
C_{12}	11.026
C_{13}	18.043
C_{23}	15.082

Table 5.1: Table of elastic constants for Li_3PS_4 crystal structure.

The expressions for the elastic moduli, i.e., shear modulus (G), bulk modulus (B) and
Youngs modulus (E) for orthorhombic crystal structure is given as:

$$G = \frac{1}{15}(C_{11} + C_{22} + C_{33} - C_{12} - C_{13} - C_{23})$$

$$+\frac{1}{5}(C_{44} + C_{55} + C_{66}) \tag{5.4}$$

$$B = \frac{1}{9}(C_{11} + C_{22} + C_{33}) + \frac{2}{9}(C_{12} + C_{13} + C_{23}) \tag{5.5}$$

$$E = \frac{9BG}{3B + G} \tag{5.6}$$

5.1.2 $Li_4P_2S_6$: Hexagonal crystal structure

Like Li_3PS_4, $Li_4P_2S_6$ is also composed of Li_2S-P_2S_5. It crystallizes into hexagonal geometry when the composition of constituents is 20% Li_2S and 80% P_2S_5. The elastic properties of a hexagonal crystal structure are adequately defined with the help of 5 independent elastic constants,viz. C_{11}, C_{12}, C_{13}, C_{33}, C_{44}. The values of elastic constants are shown in Table 5.2. The elastic moduli, viz. shear modulus (G), bulk modulus (B)

Elastic constants	Values in GPa
C_{11}	87.364
C_{12}	23.805
C_{13}	11.433
C_{33}	53.008
C_{44}	16.749

Table 5.2: Table of elastic constants for $Li_4P_2S_6$ crystal structure.

and Youngs modulus (E) are calculated with the help of the following expressions:

$$G = \frac{1}{30}(C_{11} + C_{12} + 2C_{33} - 4C_{13}$$

$$+12C_{44} + 12C_{66}) \tag{5.7}$$

$$B = \frac{1}{9}(2C_{11} + 2C_{12} + 4C_{13} + C_{33}) \tag{5.8}$$

$$E = \frac{9BG}{3B + G} \tag{5.9}$$

5.1.3 $Li_{10}GeP_2S_{12}$: Tetragonal crystal structure

$Li_{10}GeP_2S_{12}$ is the super-ionic conductor with tetragonal geometry. For the tetragonal crystal structure, 6 independent elastic constants, viz. C_{11}, C_{12}, C_{13}, C_{33}, C_{44}, and C_{66} are calculated to determine the elastic properties. Table 5.3 represents the calculated elastic constants for the $Li_{10}GeP_2S_{12}$ crystal structure. For the tetragonal geometry, the

Elastic constants	Values in GPa
C_{11}	40.124
C_{12}	23.960
C_{13}	9.675
C_{33}	41.145
C_{44}	8.196
C_{66}	15.877

Table 5.3: Table of elastic constants for $Li_{10}GeP_2S_{12}$ crystal structure.

elastic moduli may be calculated as per following expressions:

$$G = \frac{1}{30}(4C_{11} - 2C_{12} + 2C_{33} - 4C_{13}$$

$$+12C_{44} + 6C_{66}) \tag{5.10}$$

$$B = \frac{1}{9}(2C_{11} + 2C_{12} + C_{33} + 4C_{13}) \tag{5.11}$$

$$E = \frac{9BG}{3B + G} \tag{5.12}$$

5.1.4 Li_6PS_5X (X = Cl, Br, I): Cubic crytal structures

Li_6PS_5Cl, Li_6PS_5Br, and Li_6PS_5I are highly conducting argyrodite type crystal structures.
The elastic properties of cubic crystals are determined from only three independent elastic
coefficients, viz. C_{11}, C_{12}, and C_{44}. The three elastic coefficients are written in Table 5.4.
The elastic moduli for a cubic system can be calculated with the help of following formulae:

Elastic constants	Li_6PS_5Cl (GPa)	Li_6PS_5Br (GPa)	Li_6PS_5I (GPa)
C_{11}	43.047	44.210	41.831
C_{12}	22.426	20.088	18.250
C_{44}	-4.564	-101.841	-0.965

Table 5.4: Table of elastic constants for Li_6PS_5Cl, Li_6PS_5Br and Li_6PS_5I crystal structures.

$$G = \frac{1}{2}(C_{11} - C_{12}) \tag{5.13}$$

$$B = \frac{1}{3}(C_{11} + 2C_{12}) \tag{5.14}$$

$$E = \frac{9BG}{3B + G} \tag{5.15}$$

5.1.5   Elastic Moduli

Material	G (GPa)	B (GPa)	E (GPa)	B/G
$Li_{10}GeP_2S_{12}$	11.659	23.112	29.942	1.98
Li_3PS_4	10.654	22.100	25.537	2.07
$Li_4P_2S_6$	24.991	35.675	60.780	1.43
Li_6PS_5Cl	10.310	29.299	27.682	2.84
Li_6PS_5Br	12.061	28.138	31.700	2.33
Li_6PS_5I	11.790	26.110	30.742	2.21

Table 5.5: Table of elastic moduli, i.e., shear modulus (G), bulk modulus (B) and Young's modulus (E) of elasticity and Pugh's ratio for various crystalline materials.

The elastic moduli, i.e., shear modulus (G), bulk modulus (B) and Young's modulus (E) of elasticity are calculated for various materials using the formulae explained above. The ealstic moduli and the bulk modulus to shear modulus ratio are shown in the Table 5.5. The values of Young's modulus and bulk modulus for sulfide crystals are much smaller than the oxide crystals. This can be attributed to the softer Li-S bonds in sulfide materials as compared to the Li-O bonds in oxides. Lower values of E and B make the sulfide electrolyte materials mechanically more feasible. All the sulfide materials considered here have B/G value greater than 1.75 except $Li_4P_2S_6$. That means, except $Li_4P_2S_6$, all the considered sulfide materials follow Pugh's criterion of ductility, thus exhibit the ductile behaviour. Therefore, the candidate materials are mechanically stable and appropriate for the electrolytic application. $Li_4P_2S_6$ exhibits higher values of elastic moduli as well as brittle behaviour based on Pugh's criterion. The decreasing order of the ductility in the pristine crystalline materials, as can be drawn from Table 5.5, is $Li_6PS_5Cl>$ $Li_6PS_5Br >$

$Li_6PS_5I > Li_3PS_4 > Li_{10}GeP_2S_{12} > Li_4P_2S_6$. With this trend, we may say that argyrodite type crystal structures are mechanically the most suitable SSEs whereas, the $Li_4P_2S_6$ crystal structure is the least suitable one. The higher order of ductility in cubic Li_6PS_5Cl, Li_6PS_5Br, and Li_6PS_5I may be attributed to higher electron affinity of halogens. The presence of halogen atoms in the crystal lattice may further soften the Li-S bond thereby making it more ductile. This can further be varified by doping less ductile materials with the halides by inducing them at interstitial sites as point defects.

5.1.6   Halide doping

We have doped Cl, Br, and I atoms at the interstitial sites in less ductile materials, viz. Li_3PS_4 and $Li_4P_2S_6$ to understand the effect of doping in improving the elastic properties of these materials. The values of elastic moduli for differently doped Li_3PS_4 and $Li_4P_2S_6$ crystal structures are enlisted in Table 5.6. It can be inferred from the table that by

Dopant	G (GPa)	B (GPa)	E (GPa)	B/G
Li_3PS_4				
Cl	7.519	13.859	19.102	1.84
Br	6.422	15.598	16.942	2.42
I	8.991	15.598	22.625	1.73
$Li_4P_2S_6$				
Cl	14.716	24.496	36.782	1.66
Br	11.1976	24.599	29.167	2.19
I	9.595	19.123	24.660	1.99

Table 5.6: Table of elastic moduli for doped crystal structures

doping with halides (Cl, Br, and I) the elastic properties of materials can be significantly improved. We see that Youngs modulus of elasticity of Li_3PS_4 and $Li_4P_2S_6$ has reduced considerably after doping. In addition, the value of B/G has also increased. $Li_4P_2S_6$ crystal structure, according to Pugh's criterion, is a brittle material in its pristine form. However, doping with Cl, Br, and I increases the values of B/G ratio significantly. Doping

$Li_4P_2S_6$ with Br and I convert this material from brittle to ductile, thereby, making it mechanically a suitable material for SSE applications. This is probably due to the higher electron affinity of the dopant atoms which leads to the softening of Li-S bond.

5.2   Diffusional Properties

Current density of an electrochemical cell highly depends on the movement of ions through the electrolyte. Therefore, ionic mobility through the bulk of a material is a decisive parameter for the SSE applications. The ionic mobility is estimated from the diffusional characteristics of the material. Molecular dynamics simulations provide the trajectory of each atom in the system as a function of time. From this trajectory, many diffusional properties, like tracer diffusivity, tracer conductivity, jump diffusivity and activation barrier etc. may be determined. First of all, the displacement of each Li-ion from their respective mean positions can be determined as a fuction of time. The mean displacement of Li-ions averaged over a span of time may provide an insight into the ionic mobility at a given temperature.   Figure 5.1 shows the mean displacement of diffusing Li-ions averaged over 20 ps at 600 K. It can be seen from the bar graph that the maximum mean displacement of Li-ions occurs in $Li_{10}GeP_2S_{12}$ crystal. Hence, $Li_{10}GeP_2S_{12}$ crystal should be the most conducting material among various crystal structures considered in this study. Note that the Li-ions in $Li_7P_3S_{11}$ crystal as well as in the argyrodite crystals, i.e., Li_6PS_5Cl and Li_6PS_5Br also show a significant amount of displacements. This indicates that these materials should also possess high ionic conductivities.

5.2.1   Tracer Diffusivity

Tracer diffusivity is commonly used parameter to characterize the ion mobility. It is defined as:

$$D^* = \lim_{t \to \infty} [\frac{1}{2dt}(\frac{1}{N}\sum_{i=1}^{N}([r_i(t + t_0)] - [r_i(t_0)])^2)] \qquad (5.16)$$
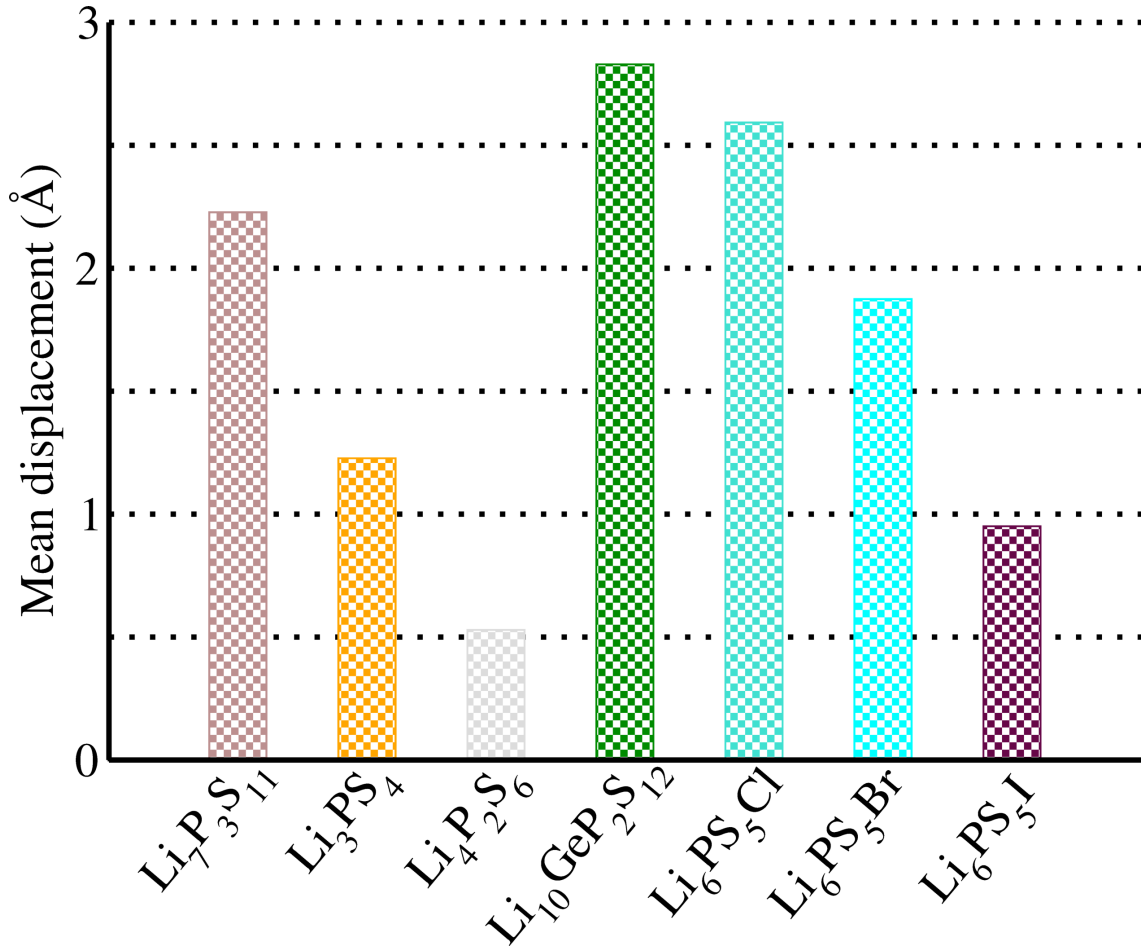
Figure 5.1: Mean displacement of Li-ions through the bulk of various materials.

where $r_i(t + t_0)$ is the spatial position of the ion with index i at a given time t, whereas, t_0 may be referred to the starting time. N is the total number of diffusing ions and d is the dimensionality of diffusion which is set equal to 3 for all the materials studied in this work. Note that the term in brackets denote the mean square displacement (MSD). MSD of the ions plotted as a function of time is used to determine the tracer diffusivity. The MSD data is fitted to a straight line. If the slope of the fitted line is denoted by m, Eq. 5.16 can be rewritten as:
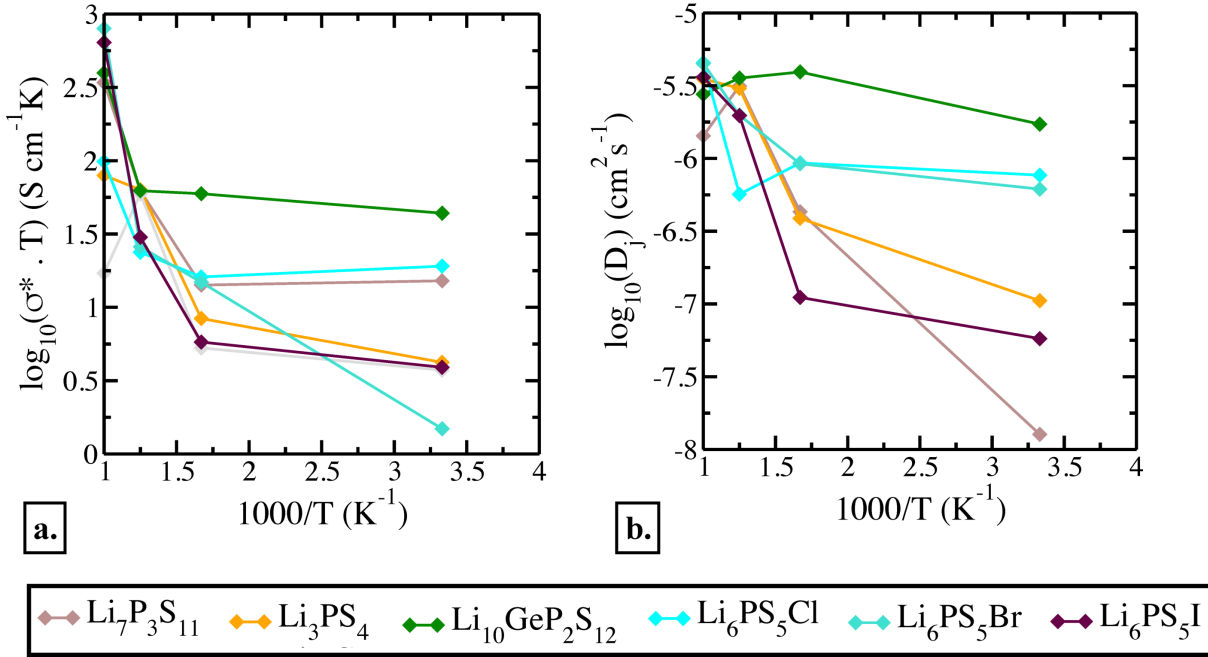
$$6D^* = m \tag{5.17}$$

Figure 5.2: (a.) tracer conductivity (b.) jump diffusivity as a function of temperature for various crystalline materials.

5.2.2 Tracer conductivity

Further, the tracer conductivity can be calculated from tracer diffusivity using the well-known Nernst-Einstein relation. The expression for tracer conductivity may be written as [165, 166]:

$$\sigma^* = \frac{\mathrm{ne}^2\mathrm{z}^2}{\mathrm{k_B}T}\mathrm{D}^*$$

(5.18)

where n is the diffusing particle density, e the elementary charge, z the ionic charge, $\mathrm{k_B}$ the Boltzmann's constant and T is the absolute temperature.

Figure 5.2 (a) shows the logarithm of tracer ionic conductivity multiplied by the respective temperatures as a function of temperature. It can be seen clearly from the plot that amongst all the materials considered in this study, $Li_{10}GeP_2S_{12}$ exhibits the maximum tracer ionic conductivity at an extensive range of temperatures. So, based on diffusional properties, $Li_{10}GeP_2S_{12}$ seems to be the most suitable material.

5.2.3 Jump diffusivity

The other important quantity to affect the macroscopic diffusion is jump diffusivity, D_j. In a crystal, the migration of ions mainly occurs by hopping of diffusing ions from one lattice site to the other. The hopping steps are generally referred to as the elementary jump processes. During this process, an ion has to migrate through the crystal structure framework's energy landscape. Therefore, such hops are considered to be the rate-limiting steps in the migration of ions through crystal structure[167]. Jump diffusivity is a measure of the number of jumps occurring between different lattice sites. It is defined as:

$$D_j = \lim_{t \to \infty} [\frac{1}{2Ndt}(\sum_{i=1}^{N}([r_i(t + t_0)] - [r_i(t_0)]))^2] \tag{5.19}$$

It can be seen from the expressions of tracer diffusivity and jump diffusivity that jump diffusivity is the measure of the displacement of the center of mass of all the diffusing ions. In contrast, tracer diffusivity takes into account the displacement of individual ions. If on average, there is no cross-correlation between displacements of different particles at different times, D_j and D^* become equivalent. Figure 5.2 (b) shows the variation of jump diffusivity with temperature for various crystalline materials. It can be inferred from the figure that $Li_{10}GeP_2S_{12}$ shows the maximum jump diffusivity at and near room temperature. So, we can say that $Li_{10}GeP_2S_{12}$ has the maximum hopping of ions between the lattice sites, thus the maximum migration of ions through the bulk material. In this regard, $Li_{10}GeP_2S_{12}$ is the most suited material with the highest hopping rate as well as the highest tracer conductivity.

5.2.4 Effect of Li-vacancy defects

Further, to understand the effect of point defects on the ionic conductivities of such materials, we have induced a single vacancy of Li-ions (V_{Li}) into the bulk materials. In a

crystalline system, ions' migration is mainly dominated by the elementary jumps between the lattice sites. Thus, the presence of vacant sites is expected to increase the rate of such jump processes. In the presence of V_{Li} defects, the diffusion mainly occurs by V_{Li} exchanging sites with the neighboring Li-ions, thus, increasing the ionic conductivity. In Table 5.7, we have shown the tracer diffusivity D^* and tracer conductivity σ^* at 600 K for various materials with and without V_{Li} defects. We can see that the values of tracer conductivities increase in the presence of point defects. Thus, we can infer that ionic conductivity can significantly be increased by inducing point defects in such materials. The increase in conductivity values in the presence of V_{Li} defects is mainly attributed to the increased number of vacant lattice sites which neighboring Li-ions can jump to. However, the resultant ionic conductivities depend on other factors also, like the number of vacancies relative to the total number of Li-ions in the cell. That is why the amount by which ionic conductivity increases is different for all the materials. For example, in the case of Li_3PS_4, one unit cell contains 12 Li-ions; therefore, inducing one vacancy in the cell results in more increase in the conductivity value as compared to $Li_{10}GeP_2S_{12}$, which has 20 Li ions per cell. However, our calculations are limited to 20 ps simulation time, which can be the possible reason for the little decrease in the value of ionic conductivity for $Li_{10}GeP_2S_{12}$ material.

5.2.5 Jump diffusion pathways and density of Li-ions

The observed trend of ionic conductivities can be explained by the thorough analysis of ionic densities inside the bulk materials and the Li-ions' jump-diffusion pathways during the diffusion process. Here, the two characteristics for all the materials as mentioned above are explained comprehensively. The role of V_{Li} defects in enhancing the diffusion is analyzed.

Material	D* (cm^{2}s^{-1})	σ^* (Scm^{-1})
$Li_7P_3S_{11}$	0.44e-07	2.37e-02
$(Li_7P_3S_{11})_v$	1.28e-07	4.25e-02
Li_3PS_4	2.43e-08	1.40e-02
$(Li_3PS_4)_v$	8.60e-08	4.54e-02
$Li_4P_2S_6$	1.49e-08	0.89e-02
$(Li_4P_2S_6)_v$	0.95e-07	5.19e-02
$Li_{10}GeP_2S_{12}$	1.52e-07	9.92e-02
$(Li_{10}GeP_2S_{12})_v$	1.47e-07	9.08e-02
Li_6PS_5Cl	0.38e-07	2.69e-02
$(Li_6PS_5Cl)_v$	0.71e-07	4.81e-02
Li_6PS_5Br	0.35e-07	2.47e-02
$(Li_6PS_5Br)_v$	0.71e-07	4.82e-02
Li_6PS_5I	0.14e-07	0.96e-02
$(Li_6PS_5I)_v$	0.54e-07	3.58e-02

Table 5.7: Table of tracer diffusivity and tracer conductivity for various materials with and without V_{Li} at 600 K.

$Li_7P_3S_{11}$

Figures 5.3 and 5.4 respectively represent the density and jump-diffusion pathways for pristine $Li_7P_3S_{11}$ crystal structure and the one with V_{Li} defect in the bulk material. Figures 5.3 (a) and 5.4(a) respectively represent the Li-ion densities in the pristine and defective bulk materials. The brown regions represent the higher densities of Li-ion, while the blue regions represent the lower densities of Li-ions. We can see that as the temperature increases, the brown, as well as the blue regions, expand to cover the whole lattice. This indicates that at lower temperatures, the ions vibrate about their mean positions and very few movements to the other lattice sites, whereas at higher temperatures, the ions vibrate about their mean positions and frequent movements to the neighboring sites. This may be attributed to the sufficient thermal energy available to the Li-ions at moderately higher temperatures so that they can easily cross the energy barrier between two lattice sites. The jump-diffusion pathways near room temperature show no noticeable hopping of Li-ion to the neighboring sites. However, in the presence of point defects like V_{Li}, the jump rate increases significantly near the room temperature as well as at moderately
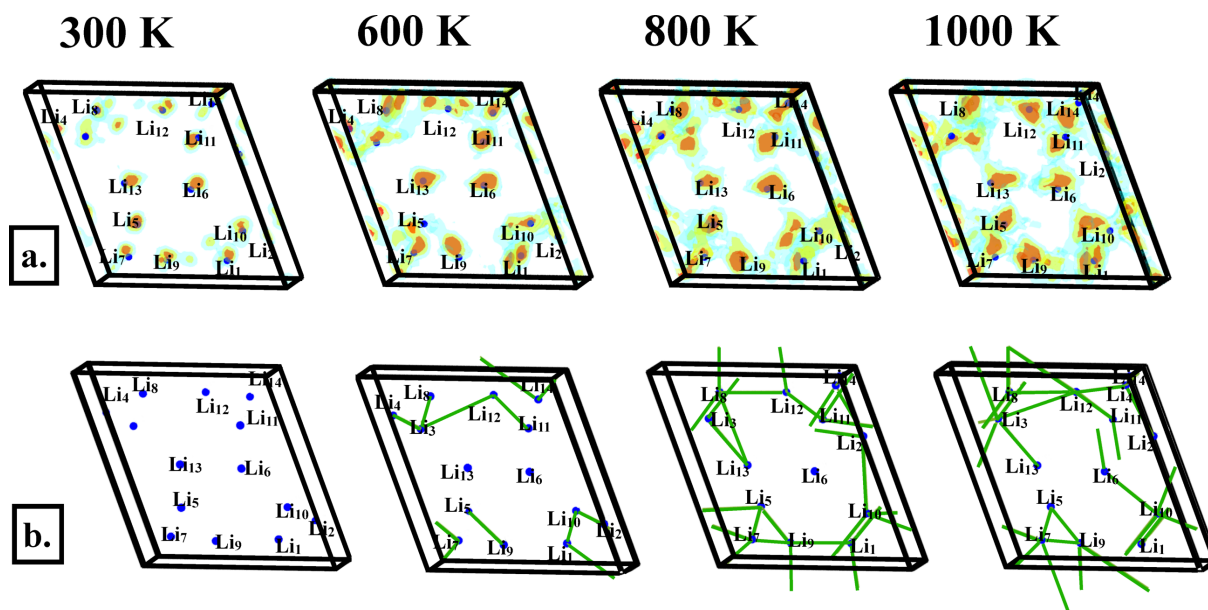
Figure 5.3: (a.) density and (b.) jump diffusion pathways for $Li_7P_3S_{11}$ crystal structure at 300 K, 600 K, 800 K, and 1000 K temperatures.
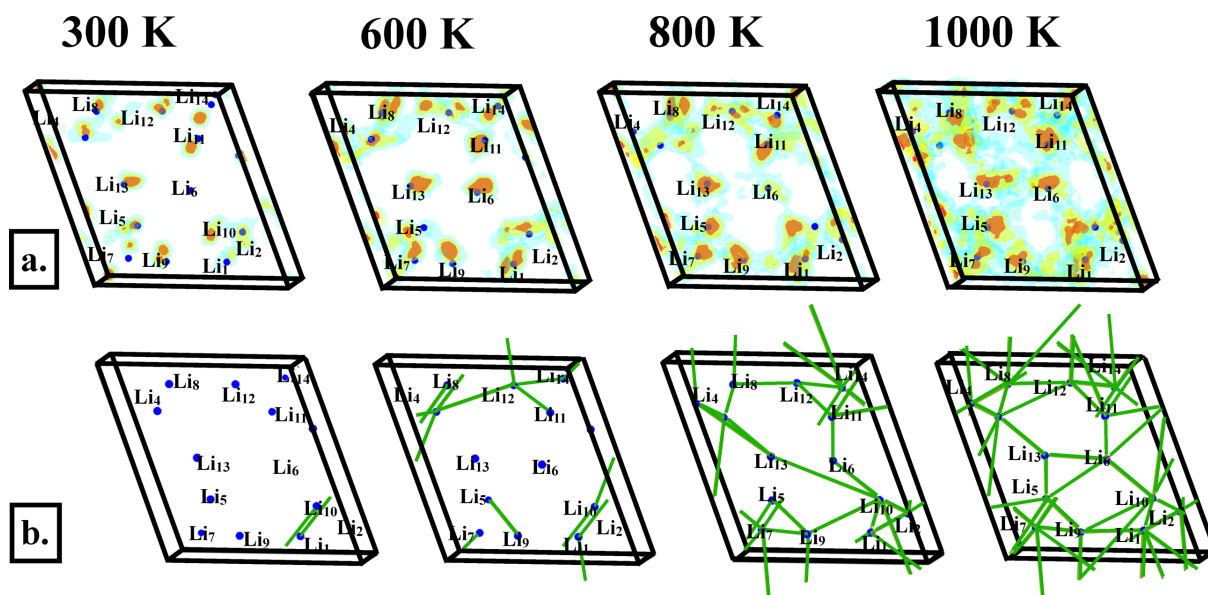

Figure 5.4: (a.) density and (b.) jump diffusion pathways for $Li_7P_3S_{11}$ crystal structure with one V_{Li} defect at 300 K, 600 K, 800 K, and 1000 K temperatures.

higher temperatures. This indicates that V_{Li} defect plays a vital role in enhancing the

diffusion of through Li-ions $Li_7P_3S_{11}$ crystal structure. Also, the higher ion-conductivity

in this system may be attributed to the 3-dimensional diffusion of Li-ions by hopping
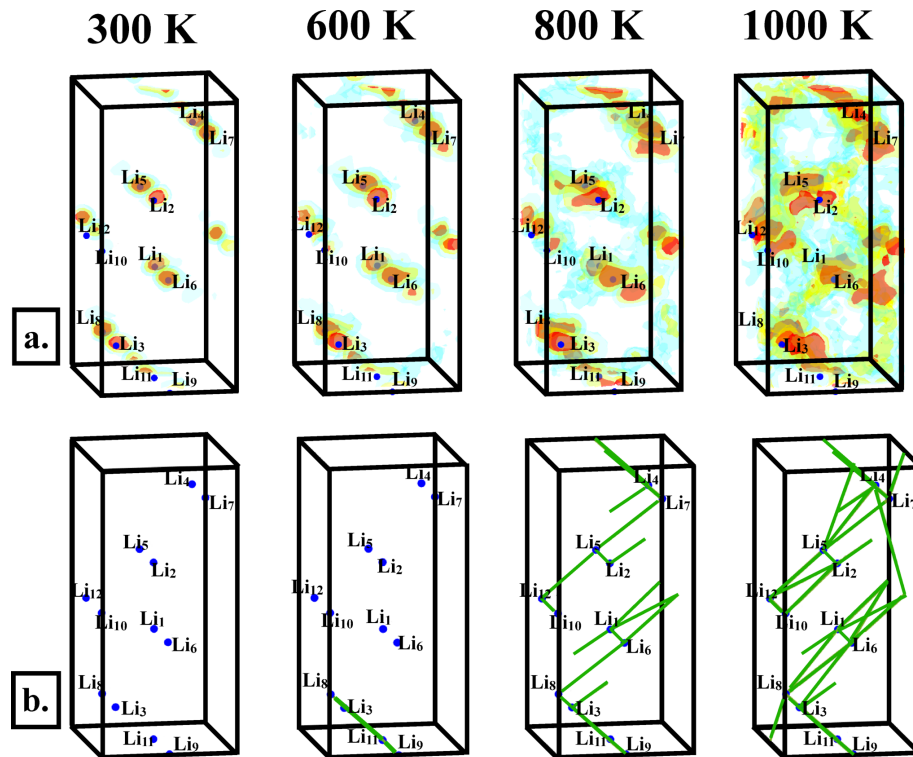from one lattice site to the other.

Li$_3$PS$_4$

Figure 5.5: (a.) density and (b.) jump diffusion pathways for Li$_3$PS$_4$ crystal structure at
300 K, 600 K, 800 K, and 1000 K temperatures.

Figures 5.5 and 5.6 respectively represent the density of mobile Li-ions as well as jump
diffusion pathways for the Li-ions in pristine Li$_3$PS$_4$ crystal structure and the one with
V$_{Li}$ defect. Figures 5.5 (a) and 5.6 (a) show the density of Li-ions in the bulk materials
with and without V$_{Li}$ defect. As explained in the previous section, the brown regions
represent the higher density regions while blue regions are the lower density regions. At
temperatures near and moderately higher than room temperature, there is enough ther-
mal energy available to the Li-ions to vibrate about their (meta)stable positions. This
can be seen from the localisation of Li-ion density around their lattice sites. However, as
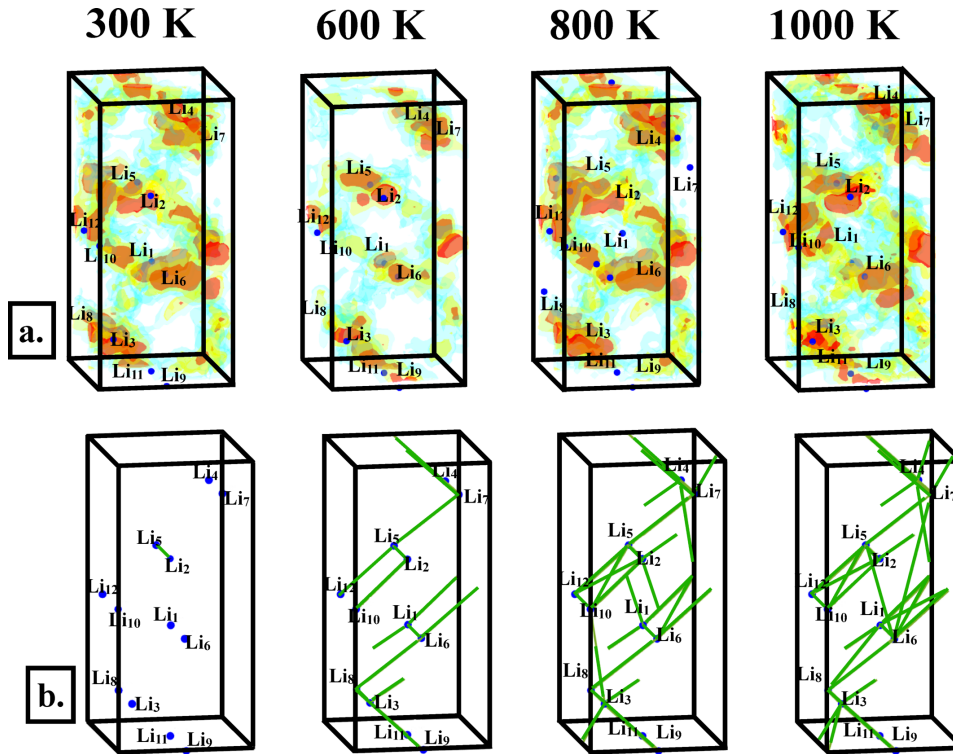
Figure 5.6: (a.) density and (b.) jump diffusion pathways for Li_3PS_4 crystal structure with one V_{Li} at 4b-position at 300 K, 600 K, 800 K, and 1000 K temperatures.

temperature increases, they get sufficient thermal energy which increases the amplitude of vibration with frequent jumps to the neighbouring sites. The jump diffusion pathways at different temperatures depict that Li-ions follow a zig-zag path while migrating through the bulk material.The zig-zag path followed by the ions eases the three dimensional diffusion of Li-ion in this material. We see that in pristine Li_3PS_4 there is no hopping of Li-ions between different lattice sites at room temperature and the Li-ions only vibrate about their (meta)stable positions. The density plot at 300 K depicts the same. However, in the presence of V_{Li} defect, there is a finite jump rate even at room tempertaure. V_{Li} defect lowers the energy barrier between two neighbouring lattice sites which facilitates the elementary jump process among various lattice sites even at moderate temperatures.
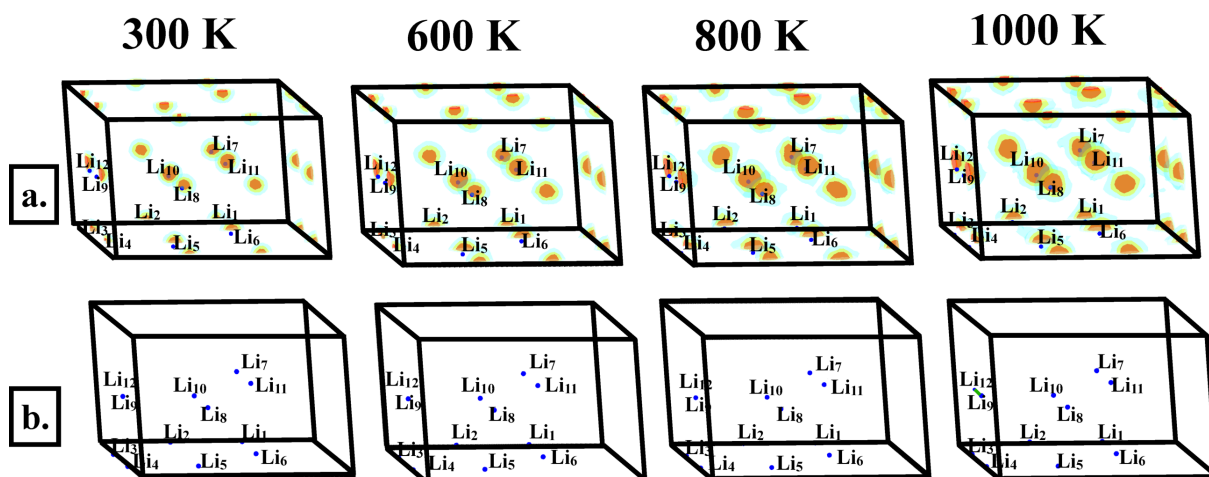
Figure 5.7: (a.) density and (b.) jump diffusion pathways for $Li_4P_2S_6$ crystal structure at 300 K, 600 K, 800 K, and 1000 K temperatures.

$Li_4P_2S_6$

Figures 5.7 and 5.8 respectively show the Li-ion densities and jump diffusion pathways in pristine and defected $Li_4P_2S_6$ crystal structure. The ion density as well as jumps plots for pristine $Li_4P_2S_6$ show that there is no noticable movement of ions through the bulk. The ions only vibrate about their mean positions. Very small jump rate even at very higher temperature indicates that this material has large energy barrier for the jump process to take place. However, the presence of V_{Li} defect in the material helps in lowering the energy barrier. Thus, the jump rate is relatively higher in the defected system. The significantly increased migration of Li-ion in presence of V_{Li} defect can be clearly seen in Figure 5.8 (a) and (b).

Li_6PS_5Cl

Figures 5.9 and 5.10 respectively, show the density of Li-ions as well as jump-diffusion pathways for pristine Li_6PS_5Cl crystal structure and the one with V_{Li} defect at various temperatures. The high Li-ion densities at sites other than the lattice sites indicate the large movement of ions through the bulk material. The ions vibrate about their mean
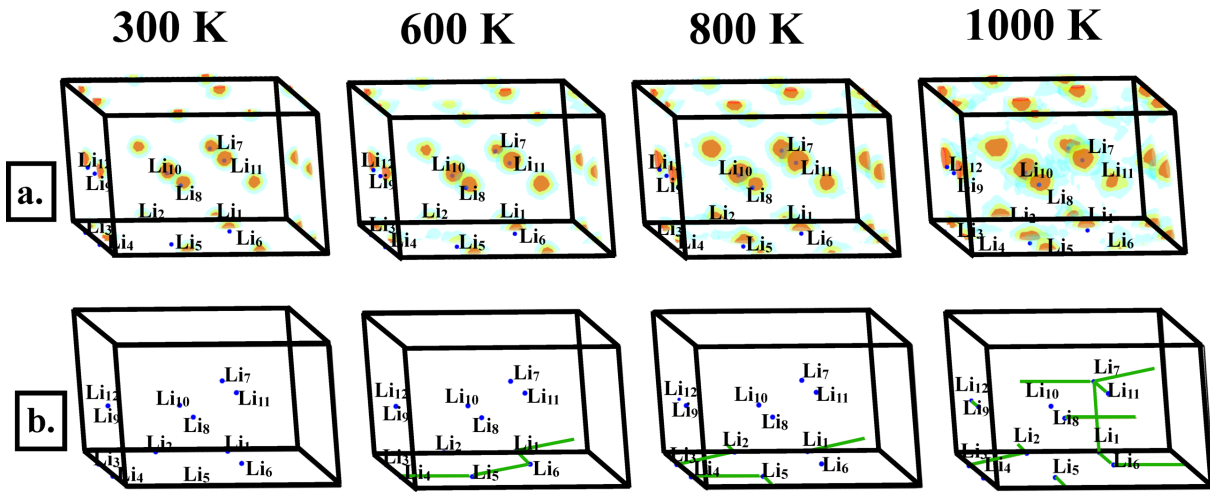
Figure 5.8: (a.) density and (b.) jump diffusion pathways for $Li_4P_2S_6$ crystal structure with one V_{Li} at 300 K, 600 K, 800 K, and 1000 K temperatures.

position with occasional hops to the neighboring sites near room temperature. However, in Figure 5.9 (b), we can see that the Li-ions form cage-like structures while hopping from one lattice-site to another. At moderate temperatures, the motion of Li-ions is confined within the cages. These are generally referred to as intra-cage jumps. This keeps the density of Li-ions localized to small areas. The number of back-and-forth jumps is large. Thus, the intra-cage jumps contribute very less toward the overall migration of the Li-ions through the bulk. The inter-cage jumps are very less in number and are the rate-limiting steps in the diffusion process. In Figure 5.9 (b), the inter-cage jumps are shown by dashed lines. We can see that the inter-cage jumps appear only at higher temperatures near 1000 K. That is why, despite having higher values of jump diffusivities, such materials practically show less ion-mobility. In the presence of point defects like V_{Li}, the rate of inter-cage jumps drastically increases, as shown in Figure 5.10 (b). Therefore, it can be inferred that point defects are crucial in such materials for the macroscopic Li-ion diffusion.
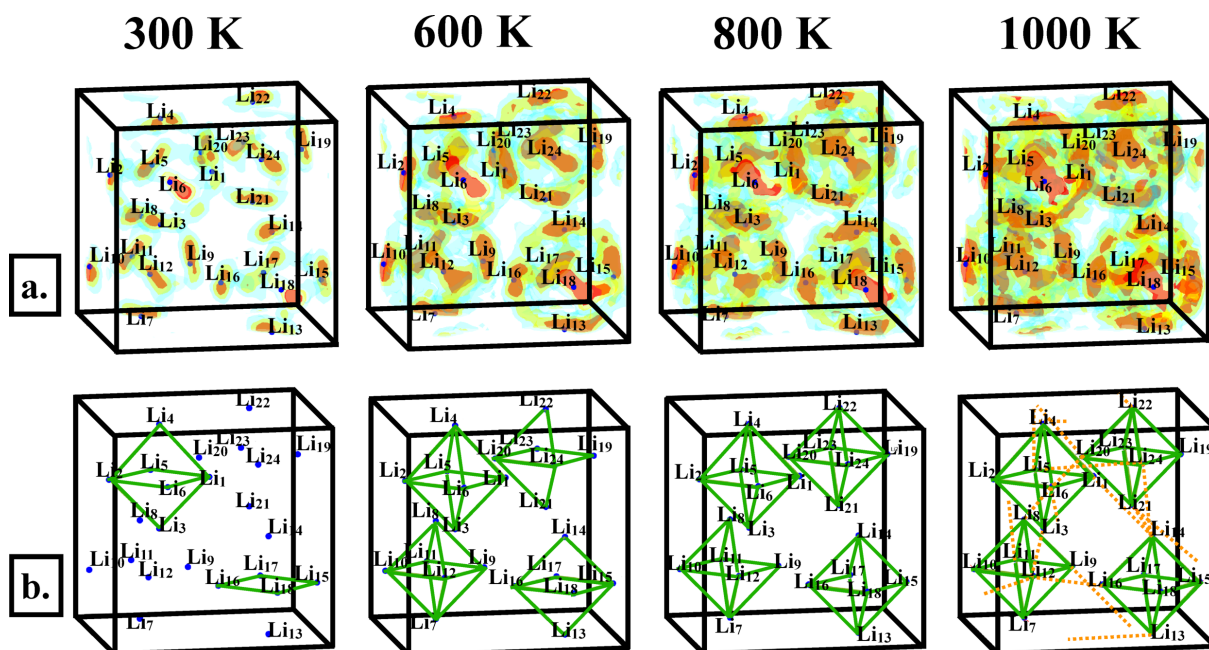
Figure 5.9: (a.) density and (b.) jump diffusion pathways for Li_6PS_5Cl crystal structure at 300 K, 600 K, 800 K, and 1000 K temperatures.
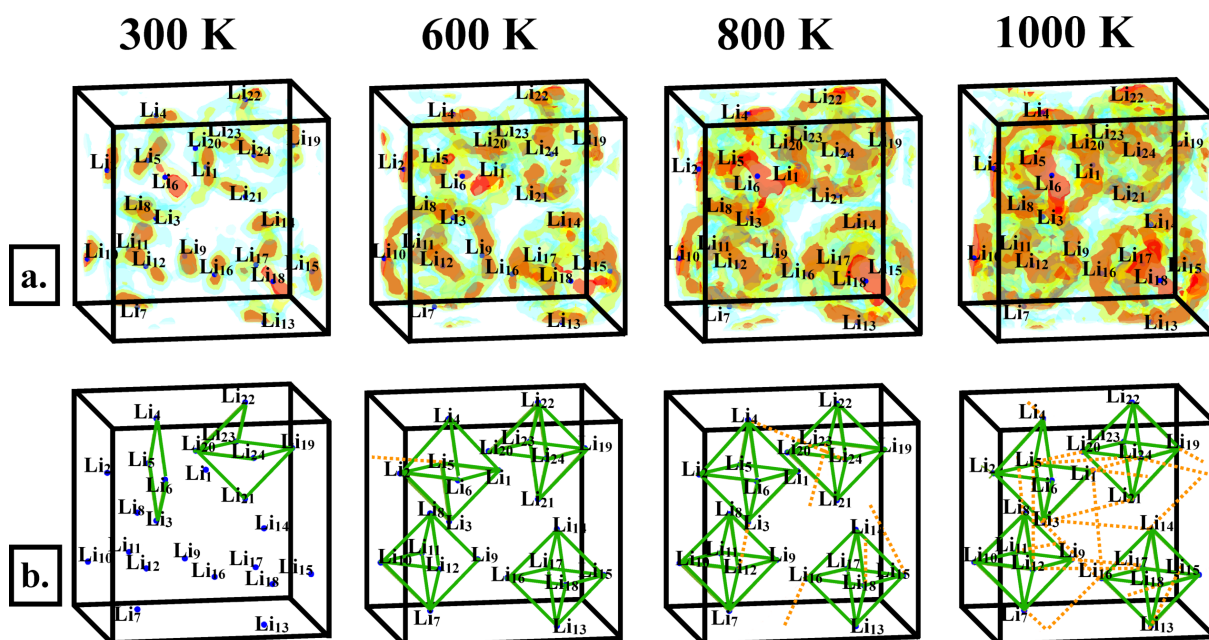
Figure 5.10: (a.) density and (b.) jump-diffusion pathways for Li_6PS_5Cl crystal structure with one V_{Li} at 300 K, 600 K, 800 K, and 1000 K temperatures.

Figure 5.11: (a.) density and (b.) jump diffusion pathways for Li_6PS_5Br crystal structure at 300 K, 600 K, 800 K, and 1000 K temperatures.
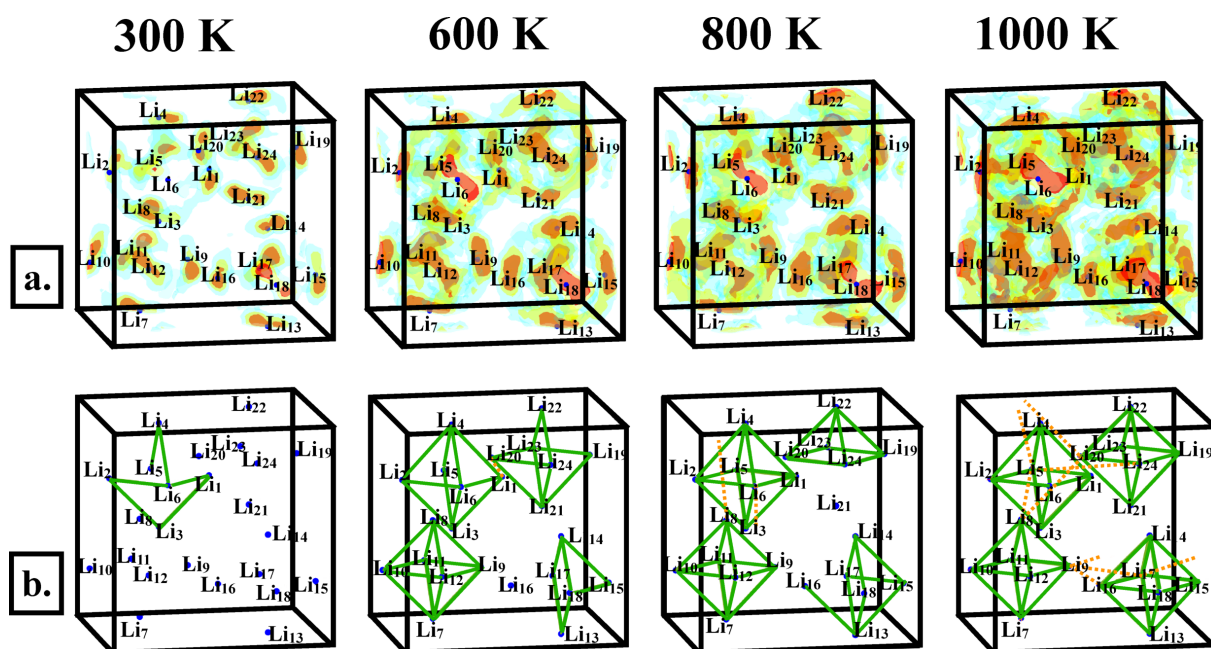
Figure 5.12: (a.) density and (b.) jump diffusion pathways for Li_6PS_5Br crystal structure with one V_{Li} at 300 K, 600 K, 800 K, and 1000 K temperatures.

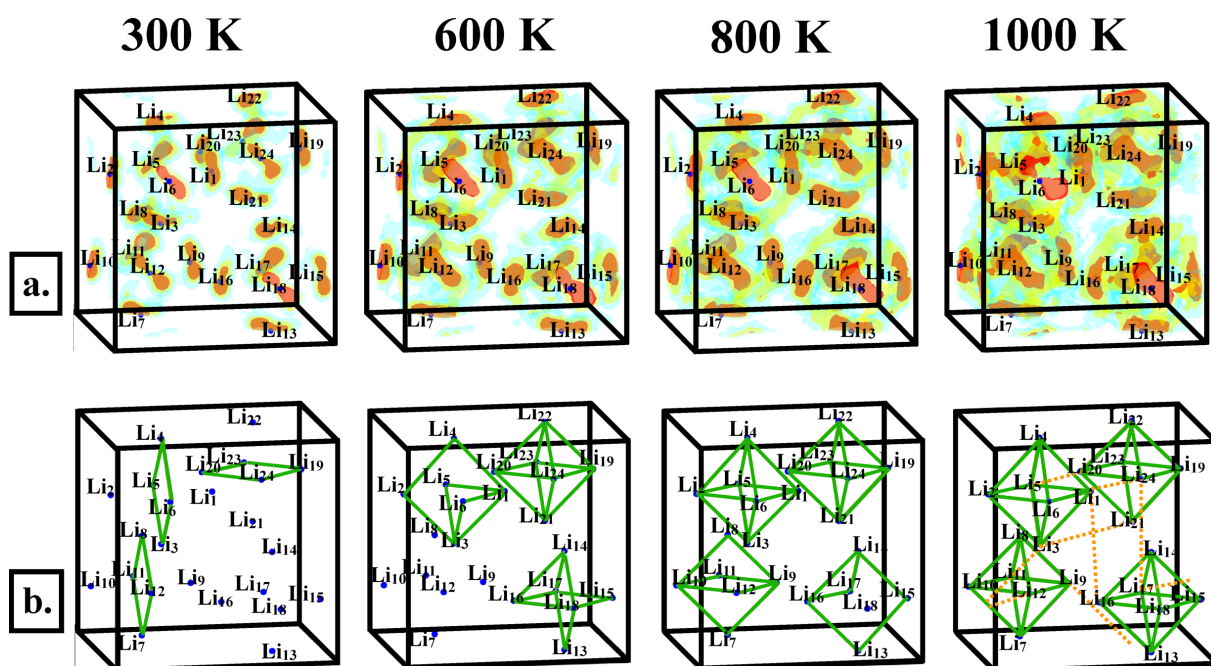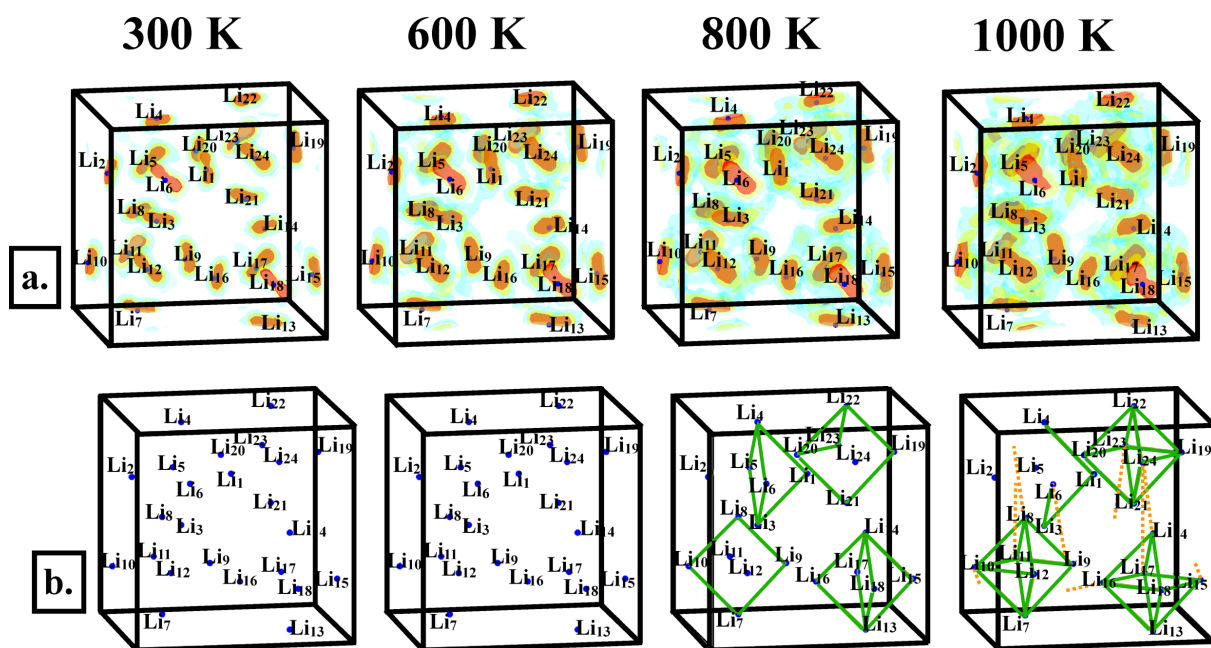Figure 5.13: (a.) density and (b.) jump diffusion pathways for Li_6PS_5I crystal structure at various temperatures.

Figure 5.14: (a.) density and (b.) jump diffusion pathways for Li_6PS_5I crystal structure with one V_{Li} at various temperatures.
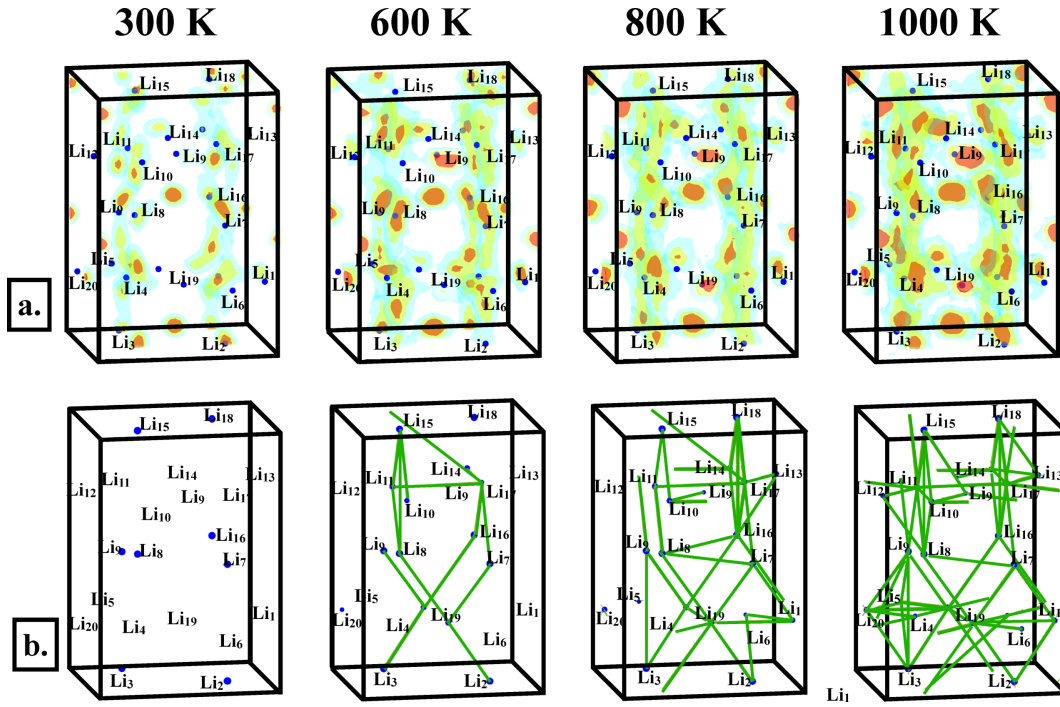
Figure 5.15: (a.) density and (b.) jump diffusion pathways for $Li_{10}GeP_2S_{12}$ crystal structure at various temperatures.

Li_6PS_5Br

Figures 5.11 and 5.12 respectively depict the variation of density of Li-ions and jump-diffusion pathways in pristine and defected Li_6PS_5Br crystalline material with temperature. The finite density between lattice sites indicates diffusion of ions even at room temperature, similar to Li_6PS_5Cl. With the increase in temperature, there is a drastic increase in the jump rates. However, these jumps take place within the cage-like pathways formed by the mobile Li-ions. Hence, the intercage jumps do not occur below 1000 K. However, in the presence of V_{Li} defects, the intercage jumps occur at 800 K. Hence, for this material, the V_{Li} defects play an important role in enhancing the diffusional properties.

Li_6PS_5I

Similar to other members of Li_6PS_5X (X=Cl, Br, I), the Li-ions in Li_6PS_5I form the cage-like pathways while migrating through the bulk material. However, here, we can
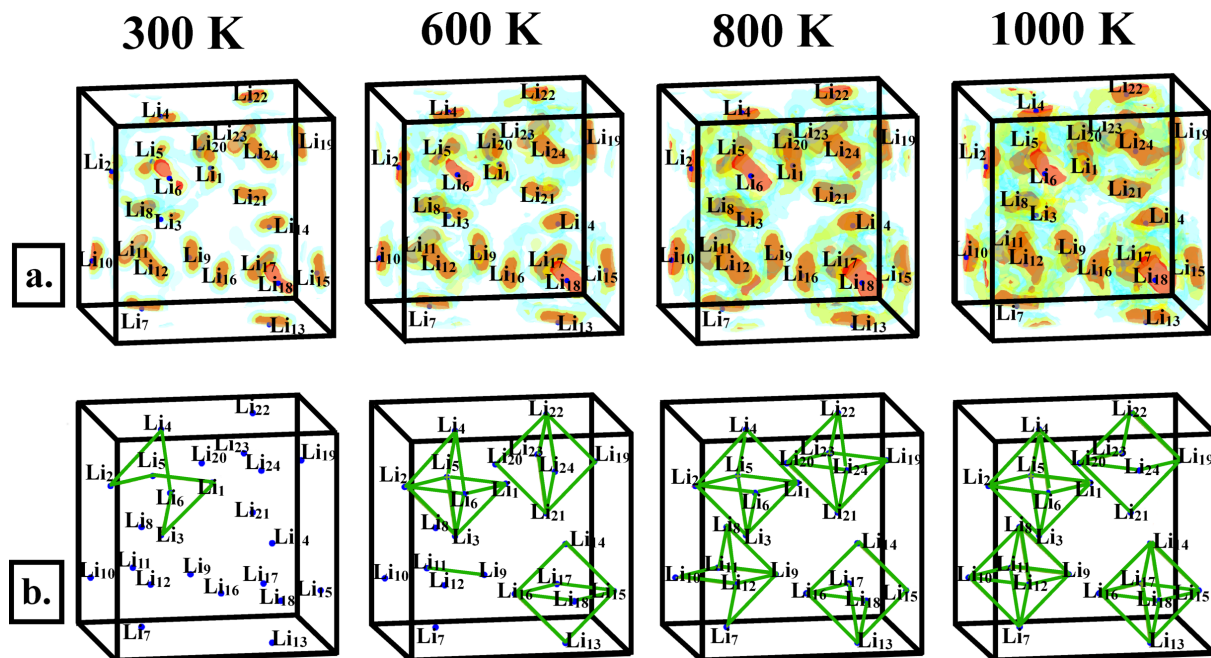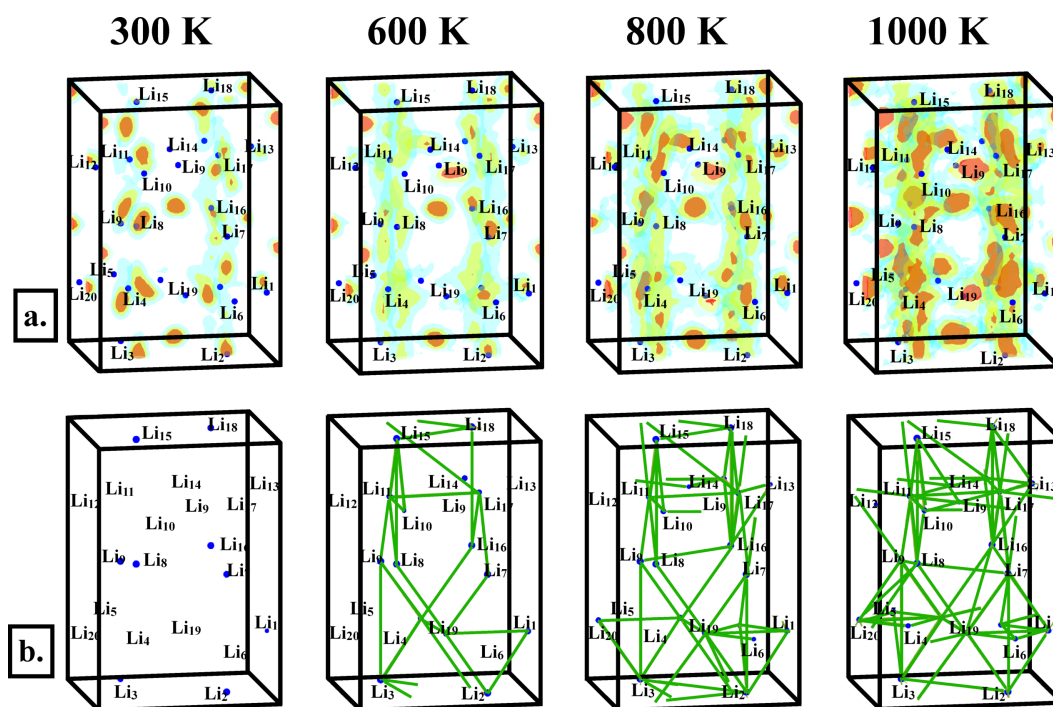
Figure 5.16: (a.) density and (b.) jump diffusion pathways for $Li_{10}GeP_2S_{12}$ crystal structure with one V_{Li} at various temperatures.

see relatively much fewer jump rates at all temperatures. The presence of V_{Li} defect increases the inter-cage as well as intra-cage jump processes. Therefore, we may infer that the diffusional properties of Li_6PS_5I can be significantly improved by inducing point defects.

$Li_{10}GeP_2S_{12}$

Figures 5.15 and 5.16 show the density of mobile Li-ions and jump diffusion pathways for $Li_{10}GeP_2S_{12}$ crystal structure with and without V_{Li} at various temperatures. Unlike most of the materials, the density plot at 300 K shows that the Li-ions in $Li_{10}GeP_2S_{12}$ migrate throughout the bulk of the material in addition to vibrating about their mean position even at room temperature. On increasing the temperature, one may observe a significant increase in density of Li-ions in between any two lattice sites, indicating migration of Li-ions through hopping among the lattice sites. Li-ions follow a specific path and are

seen to move forward. The number of back-and-forth jumps is less in this case. Thus, there is less disparity in the jump diffusivity and tracer diffusivity. Therefore, the jumps shown in the figure contribute to the overall migration of Li-ions through the bulk. Thus, the tracer conductivity is relatively higher than the other materials. Figure 5.16 depicts that on inducing the V_{Li} defects in the crystal structure, the jump rate among various lattice sites may be enhanced further.

Here, we can conclude that the sulfide crystalline materials are mechanically suitable for solid-state batteries' electrolytic applications. The halide dopants can further improve the elasticity and mechanical stability of such materials. $Li_{10}GeP_2S_{12}$ exhibits the highest ionic conductivity among the various materials discussed here. Lithium vacancy significantly improves the ion mobility in such materials.

Chapter 6

Conclusion

The thesis aimed to identify the role of advanced solid-state materials in renewable energy applications. Also, to understand the effects of crystal defects in enhancing the desired properties of the materials.

Chapter 1 has emphasized the need to shift to renewable energy sources by mentioning the unpreventable drawbacks of continued utilization of fossil fuels for more than a century. We have given a detailed introduction of alternative approaches to fulfilling the energy requirements while reducing fossil fuel burning and controlling CO_2 content in the atmosphere.

Firstly, we have explained hydrogen storage technology that uses advanced solid-state materials. Hydrogen is a clean energy source, and its abundance in the atmosphere makes it a promising alternative to fossil fuels. Hydrogen has high diffusivity. Therefore, the practical utilization of hydrogen energy requires safe and cost-effective storage and delivery medium. Conventional hydrogen-storage methods are energy-intensive and unsafe. Consequently, it is crucial to store hydrogen in solid-state materials. The prerequisites of a hydrogen-storage material include high gravimetric and volumetric density, reversible storage, and fast hydrogen release kinetics at moderate temperatures.

Secondly, we have introduced the method of chemical reduction of CO_2 to CO, a crucial

industrial feedstock. It is a method that lowers the greenhouse gas concentration in the atmosphere and simultaneously provides vital precursors for the synthesis of highly valued chemicals. Electrochemical reduction (ECR) of CO_2 requires the solid-state materials as an electrocatalyst. An electrocatalyst in the ECR process is the cathode material on which CO_2 reduces to form various other compounds. The product formed highly depends on the electrocatalyst. ECR of CO_2 to CO and hydrogen evolution reaction have similar value of reduction potential. Therefore, the electrocatalyst is required to exhibit high product selectivity. Various solid-state electrocatalyst materials have been explored and investigated to tune their properties to enhance product selectivity and Faradaic efficiency.

Finally, we have explained the Li-ion batteries as a next-generation energy storage technology. Li is the lightest metal element. Thus Li-ion batteries exhibit the highest energy density and power a wide range of electronic devices and automobiles. However, the use of volatile liquid electrolytes poses serious safety issues—the possibility of an explosion in a short circuit limits Li-ion batteries' realization into heavy vehicular applications. Replacing the liquid electrolytes with solid-state electrolyte materials eliminates the risk of thermal runaway and improves the battery design. Advanced solid-state materials for electrolytic applications have gained much research attention in the recent past. The critical requirements for a candidate material are appropriate mechanical properties and high ionic conductivity.

Efficient hydrogen energy usage, conversion of CO_2 to vital industrial precursors, and solid-state Li-ion batteries are paths toward sustainable development. These modern technologies require suitable solid-state materials for their realization into practical applications. Computational materials science provides an efficient way to explore such materials and predict various properties.

In chapter 2, we have elaborated the theoretical methodologies used in this thesis. We have carried out the computational experiments using a well-established theory, density func-

tional theory (DFT), along with the methods of ab-initio thermodynamics. DFT is based on the fact that the electronic ground state density can determine all the ground-state and excited-state properties of a system. The approach of and Kohn makes DFT an exact theory for the interacting system of many electrons. Hohenberg-Kohn theorem states that electrons' ground state density uniquely determines the external potential acting on the electrons, and the exact ground state density is obtained by minimizing the total energy. The energy is written as a functional of density; however, there is no known way to write kinetic energy as an explicit functional of density. This problem is solved by Kohn-Sham ansatz, where a fully interacting system of electrons is replaced with an auxiliary system of noninteracting electrons. The kinetic energy is written as a function of electronic orbitals. All the interaction terms of electron-electron correlation are taken care of separately in the exchange-correlation functional. In Kohn-Sham DFT, various exchange-correlational functionals are used to determine a many-body interacting system's electronic structure. The functionals with increasing order of accuracy and computational cost are LDA (local density approximation, GGA (generalized gradient approach), and hybrid functionals. Ground-state electronic structure calculations are carried out with the help of DFT. The system's properties at realistic environmental conditions can be determined with the help of ab-initio thermodynamics techniques. Further, the dynamical properties like diffusional properties can be determined with molecular dynamics (MD) simulations. MD simulations provide the trajectory of the particles as a function of time by solving the equations of motion at each time step. In classical MD simulations, the interatomic forces at every time step are calculated from the available forcefields. Whereas, in ab-initio molecular dynamics (AIMD) simulations, no forcefield is required. The forces are calculated "on the fly" from the electronic structure calculations.

In chapter 3, we elucidate the effect of temperature and pressure on the charged defects in $NaAlH_4$, a prototypical system that is widely studied for hydrogen storage applications. Complex metal hydrides are a promising class of hydrogen storage materials with high

storage capacity. $NaAlH_4$ is one such complex metal hydride where hydrogen is found strongly bonded to the central Al atoms. The release of hydrogen takes place at relatively higher temperatures. Also, the dehydrogenation reactions proceed with sluggish kinetics. The release of hydrogen at practically feasible environmental conditions is possible only in the presence of a suitable catalyst. Transition metal (TM) atoms are widely considered for this purpose because of their high catalytic activity. The hydrogen release mechanism from the catalyzed $NaAlH_4$ involves diffusion of intrinsic hydrogen-related defects, viz., hydrogen-vacancy $[V_H]^q$ and hydrogen-interstitial $[I_H]^q$ defects. We have determined the relative stability of charged H-related defects as a function of the electron's chemical potential, μ_e. The stability of defects is estimated from the formation energy calculations first carried out with the DFT. We infer that $[V_H]^{+1}$ defect is the most stable defect for μ_e values near the valence band, whereas $[I_H]^{-1}$ exhibits the maximum stability for μ_e values near the conduction band. However, the values of formation energy obtained from the DFT predict the stability of defects only at 0K. The properties of a system vary significantly under different environmental conditions. Therefore, it is crucial to determine the defects' stability at the operational temperature and pressure conditions. We have incorporated the effects of temperature and partial pressure of hydrogen with ab-initio thermodynamics. Here, we have added the free energy of lattice vibrations at a given temperature to the supercell's energy obtained from DFT. Besides, the partial pressure of hydrogen and temperature effects is duly incorporated in hydrogen's chemical potential where translational, rotational, and vibrational energies of molecular hydrogen are added to the DFT energy. By adding the effects of temperature and pressure, we observe that the most stable defect states completely switch. At 0 K, the most stable defect state near conduction band minimum (CBm) is $[I_H]^{-1}$, whereas, on increasing the temperature to room temperature and above, the most stable defect state shifts to $[I_H]^{-1}$. The concentration of defects calculated as a function of temperature at a constant value of μ_e at CBm, confirms the above findings. $[I_H]^{-1}$ defect state shows the maximum concentration below

300 K. In contrast, $[V_H]^{-1}$ defect state shows the maximum concentration above 300 K. Thus, it is very crucial to add the effects of temperature and pressure while capturing the stability of defects in such materials. DFT alone fails to predict the most stable defect configurations in these materials, the inclusion of temperature and pressure is essential. Further, we investigate the effect of TM atom doping on the hydrogen desorption kinetics of $NaAlH_4$. We dope various TM atoms, viz., Cd, Zn, Pd, Ti, Ni, and Sc at the lattice sites of Na and Al-atoms. The selection of the best suited TM atom for catalytic actions is based on three main factors. Firstly, the stability of the dopant, which is estimated from the formation energy calculations. The stability of a dopant at a given site predicts whether it is practically possible to induce the defect on the lattice site or not—secondly, the distortion in the crystal structure due to TM atom dopants. Thirdly, the change in the stability of intrinsic H-related defects after doping. Based on these factors, Ti and Sc are the most appropriate dopants for improving the environmental conditions and hydrogen desorption kinetics.

Chapter 4 explains the role of oxygen-vacancies in enhancing the catalytic activity of Cu-In-O nanocomposite for electrochemical reduction (ECR) of CO_2 to CO. The ECR of CO_2 to CO is a process widely accepted to lower the CO_2 concentration in the atmosphere while producing useful industrial precursors. The process of ECR takes place in an electrochemical cell where the cathode material works as an electrocatalyst. Cu-In-O nanocomposites are experimentally found to have very high catalytic activity and high selectivity against the competing hydrogen evolution reaction (HER). We first model the Cu-In-O composites with a well-established code cascade genetic algorithm (GA) to depict the experimentally synthesized nanocomposites. We then investigate the role of oxygen vacancies (V_O) on the catalytic activity of the modeled system. We have calculated the reaction enthalpy for the conversion of CO_2 to CO with DFT energy calculations for different concentrations of V_O defects. Our results reveal that on increasing the V_O defect concentration, the reaction enthalpy decreases from 0.48 eV to 0.31 eV.

Further, we theoretically explain the high selectivity of Cu-In-O composites by analyzing molecular hydrogen evolution at various sites in the modeled system. We observe that hydrogen evolution at the site of Indium is impossible spontaneously. Therefore, we conclude that Indium assists in suppressing the competing HER and enhancing the Cu-In-O electrocatalysts' product selectivity.

Chapter 5 describes the mechanical and diffusional properties of various sulfide materials for the electrolytic applications in all-solid-state batteries. Solid-state batteries are the future of upcoming energy storage technologies. In solid-state batteries, the conventional liquid electrolyte materials are replaced with solid-state materials, eliminating the risk of thermal runaway and making the battery design compact. While cycling, the volume of the electrode materials changes due to lithiation and de-lithiation processes. The candidate solid electrolyte material must maintain physical contact with the expanding and contracting electrode materials to ensure the battery's proper functioning. Therefore, the appropriate mechanical properties of the materials are the prerequisites for electrolytic applications. The material must be elastic enough to prevent the loss of contact without fracturing. The materials' mechanical stability is estimated from the ductility. According to Pugh's criterion of ductility, a material is ductile if the ratio of bulk modulus to shear modulus of elasticity (B/G) is greater than 1.75, the material is ductile. We calculate the elastic moduli of various candidate materials, viz., Li_3PS_4, $Li_4P_2S_6$, $Li_{10}GeP_2S_{12}$, and Li_6PS_5X (X = Cl, Br,and I). The B/G ratio of all the materials mentioned above is found out to be greater than 1.75 except for $Li_4P_2S_6$. Therefore, all the materials except $Li_4P_2S_6$ are mechanically stable and fit for electrolytic applications. We have done halide doping in the bulk of non-ductile material. We observe that the values of the B/G ratio increase after doping, and the material becomes ductile. In addition to this, the material becomes more elastic. Hence, we conclude that halide doping significantly improves the mechanical properties of the solid-state electrolyte materials.

Further, we investigate these materials' diffusional properties to select the best-suited

material for the application in solid-state electrolytes. We have carried out the ab-initio molecular dynamics (AIMD) simulations at various temperatures to obtain the trajectories of the Li-ions as a function of time. At first, we get an idea of the highly conducting materials using the mean displacement of Li-ions from their equilibrium positions within a simulation period of 20 ps. We observe that the maximum mean displacement is obtained for $Li_{10}GeP_2S_{12}$. Then, we calculate the tracer diffusivity and jump diffusivity of all the materials from mean square displacements as a function of temperature. We see that $Li_{10}GeP_2S_{12}$ exhibits the highest values of diffusivities at room temperature and moderately higher temperatures. We explain the observed trend of ionic mobilities in the materials with the jump-diffusion pathways and density of mobile Li-ions. A thorough investigation of diffusion pathways and densities through the bulk materials justifies the highest values of diffusivities for $Li_{10}GeP_2S_{12}$. Finally, we examine the effect of Li-vacancies, V_{Li} on the ionic conductivities of such materials. We find that the ionic conductivities increase significantly in the presence of V_{Li} defects.

Bibliography

[1] S. Niaz, T. Manzoor, and A. H. Pandith, "Hydrogen storage: Materials, methods and perspectives," *Renewable and Sustainable Energy Reviews*, vol. 50, pp. 457–469, 2015.

[2] M. Aneke and M. Wang, "Energy storage technologies and real life applications–a state of the art review," *Applied Energy*, vol. 179, pp. 350–377, 2016.

[3] W. Xiao, W. G. Dunford, and A. Capel, "A novel modeling method for photovoltaic cells," in *2004 IEEE 35th Annual Power Electronics Specialists Conference (IEEE Cat. No. 04CH37551)*, vol. 3, pp. 1950–1956, IEEE, 2004.

[4] R. Chenni, M. Makhlouf, T. Kerbache, and A. Bouzid, "A detailed modeling method for photovoltaic cells," *Energy*, vol. 32, no. 9, pp. 1724–1730, 2007.

[5] R. W. Miles, G. Zoppi, and I. Forbes, "Inorganic photovoltaic cells," *Materials today*, vol. 10, no. 11, pp. 20–27, 2007.

[6] S. Priya, "Modeling of electric energy harvesting using piezoelectric windmill," *Applied Physics Letters*, vol. 87, no. 18, p. 184101, 2005.

[7] Z. Glasnovic and J. Margeta, "The features of sustainable solar hydroelectric power plant," *Renewable energy*, vol. 34, no. 7, pp. 1742–1751, 2009.

[8] P. P. Edwards, V. Kuznetsov, and W. I. David, "Hydrogen energy," *Philosophical Transactions of the Royal Society A: Mathematical, Physical and Engineering Sciences*, vol. 365, no. 1853, pp. 1043–1056, 2007.

[9] M. Momirlan and T. Veziroglu, "Current status of hydrogen energy," *Renewable and sustainable energy reviews*, vol. 6, no. 1-2, pp. 141–179, 2002.

[10] H. Li, Z. Wang, L. Chen, and X. Huang, "Research on advanced materials for li-ion batteries," *Advanced materials*, vol. 21, no. 45, pp. 4593–4607, 2009.

[11] V. Etacheri, R. Marom, R. Elazari, G. Salitra, and D. Aurbach, "Challenges in the development of advanced li-ion batteries: a review," *Energy & Environmental Science*, vol. 4, no. 9, pp. 3243–3262, 2011.

[12] F. Zhang, P. Zhao, M. Niu, and J. Maddy, "The survey of key technologies in hydrogen energy storage," *International Journal of Hydrogen Energy*, vol. 41, no. 33, pp. 14535–14552, 2016.

[13] T. A. Strobel, K. C. Hester, C. A. Koh, A. K. Sum, and E. D. Sloan Jr, "Properties of the clathrates of hydrogen and developments in their applicability for hydrogen storage," *Chemical physics letters*, vol. 478, no. 4-6, pp. 97–109, 2009.

[14] V. V. Struzhkin, B. Militzer, W. L. Mao, H.-k. Mao, and R. J. Hemley, "Hydrogen storage in molecular clathrates," *Chemical reviews*, vol. 107, no. 10, pp. 4133–4151, 2007.

[15] H. Lee, J.-w. Lee, D. Y. Kim, J. Park, Y.-T. Seo, H. Zeng, I. L. Moudrakovski, C. I. Ratcliffe, and J. A. Ripmeester, "Tuning clathrate hydrates for hydrogen storage," in *Materials For Sustainable Energy: A Collection of Peer-Reviewed Research and Review Articles from Nature Publishing Group*, pp. 285–288, World Scientific, 2011.

[16] M. Hirscher, B. Panella, and B. Schmitz, "Metal-organic frameworks for hydrogen storage," *Microporous and mesoporous materials*, vol. 129, no. 3, pp. 335–339, 2010.

[17] H. W. Langmi, J. Ren, and N. M. Musyoka, "Metal–organic frameworks for hydrogen storage," in *Compendium of Hydrogen Energy*, pp. 163–188, Elsevier, 2016.

[18] E. Ashby, G. Brendel, and H. Redman, "Direct synthesis of complex metal hydrides," *Inorganic Chemistry*, vol. 2, no. 3, pp. 499–504, 1963.

[19] K. Malik, N. K. Bajaj, and A. Verma, "Effect of catalyst layer on electrochemical reduction of carbon dioxide using different morphologies of copper," *Journal of CO2 Utilization*, vol. 27, pp. 355–365, 2018.

[20] K. P. Kuhl, E. R. Cave, D. N. Abram, and T. F. Jaramillo, "New insights into the electrochemical reduction of carbon dioxide on metallic copper surfaces," *Energy & Environmental Science*, vol. 5, no. 5, pp. 7050–7059, 2012.

[21] S. Rasul, D. H. Anjum, A. Jedidi, Y. Minenkov, L. Cavallo, and K. Takanabe, "A highly selective copper–indium bimetallic electrocatalyst for the electrochemical reduction of aqueous co2 to co," *Angewandte Chemie*, vol. 127, no. 7, pp. 2174–2178, 2015.

[22] J. B. Goodenough and Y. Kim, "Challenges for rechargeable li batteries," *Chemistry of materials*, vol. 22, no. 3, pp. 587–603, 2009.

[23] A. Züttel, "Materials for hydrogen storage," *Materials today*, vol. 6, no. 9, pp. 24–33, 2003.

[24] S. Bhattacharya, C. Majumder, and G. Das, "Hydrogen storage in ti-decorated bc4n nanotube," *The Journal of Physical Chemistry C*, vol. 112, no. 45, pp. 17487–17491, 2008.

[25] P. J. Hall and E. J. Bain, "Energy-storage technologies and electricity generation," *Energy policy*, vol. 36, no. 12, pp. 4352–4355, 2008.

[26] I. Hadjipaschalis, A. Poullikkas, and V. Efthimiou, "Overview of current and future energy storage technologies for electric power applications," *Renewable and sustainable energy reviews*, vol. 13, no. 6-7, pp. 1513–1522, 2009.

[27] B. Bogdanovic and M. Schwickardi, "Ti-doped alkali metal aluminium hydrides as potential novel reversible hydrogen storage materials1," *Journal of alloys and compounds*, vol. 253, pp. 1–9, 1997.

[28] T. Ichikawa, N. Hanada, S. Isobe, H. Leng, and H. Fujii, "Mechanism of novel reaction from linh2 and lih to li2nh and h2 as a promising hydrogen storage system," *The Journal of Physical Chemistry B*, vol. 108, no. 23, pp. 7887–7892, 2004.

[29] B. Sakintuna, F. Lamari-Darkrim, and M. Hirscher, "Metal hydride materials for solid hydrogen storage: a review," *International journal of hydrogen energy*, vol. 32, no. 9, pp. 1121–1140, 2007.

[30] F. Schüth, B. Bogdanovic, and M. Felderhoff, "Light metal hydrides and complex hydrides for hydrogen storage," *Chemical communications*, vol. 20, pp. 2249–2258, 2004.

[31] S. Bhattacharya, G. Wu, C. Ping, Y. Feng, and G. Das, "Lithium calcium imide [li2ca (nh) 2] for hydrogen storage: structural and thermodynamic properties," *The Journal of Physical Chemistry B*, vol. 112, no. 36, pp. 11381–11384, 2008.

[32] S. Bhattacharya, Z. Xiong, G. Wu, P. Chen, Y. Feng, C. Majumder, and G. Das, "Dehydrogenation mechanism of monoammoniated lithium amidoborane [li (nh3) nh2bh3]," *The Journal of Physical Chemistry C*, vol. 116, no. 16, pp. 8859–8864, 2012.

[33] L. Schlapbach and A. Züttel, "Hydrogen-storage materials for mobile applications," in *Materials For Sustainable Energy: A Collection of Peer-Reviewed Research and Review Articles from Nature Publishing Group*, pp. 265–270, World Scientific, 2011.

[34] S. Orimo, Y. Nakamori, J. R. Eliseo, A. Züttel, and C. M. Jensen, "Complex hydrides for hydrogen storage," *Chemical Reviews*, vol. 107, no. 10, pp. 4111–4132, 2007.

[35] K. Maeda and K. Domen, "New non-oxide photocatalysts designed for overall water splitting under visible light," *The Journal of Physical Chemistry C*, vol. 111, no. 22, pp. 7851–7861, 2007.

[36] C. Suwanchawalit and S. Wongnawa, "Triblock copolymer-templated synthesis of porous tio 2 and its photocatalytic activity," *Journal of Nanoparticle Research*, vol. 12, no. 8, pp. 2895–2906, 2010.

[37] T. Sakata, T. Kawai, and M. Gratzel, "Energy resources through photochemistry and catalysis," *Gratzel, M., ed*, 1983.

[38] R. Moradi and K. M. Groth, "Hydrogen storage and delivery: Review of the state of the art technologies and risk and reliability analysis," *International Journal of Hydrogen Energy*, vol. 44, no. 23, pp. 12254–12269, 2019.

[39] Y. Liu, J. F. Eubank, A. J. Cairns, J. Eckert, V. C. Kravtsov, R. Luebke, and M. Eddaoudi, "Assembly of metal–organic frameworks (mofs) based on indium-trimer building blocks: A porous mof with soc topology and high hydrogen storage," *Angewandte Chemie International Edition*, vol. 46, no. 18, pp. 3278–3283, 2007.

[40] X. Lang, S. Fan, and Y. Wang, "Intensification of methane and hydrogen storage in clathrate hydrate and future prospect," *Journal of Natural Gas Chemistry*, vol. 19, no. 3, pp. 203–209, 2010.

[41] C. Liu, Y. Fan, M. Liu, H. Cong, H. Cheng, and M. S. Dresselhaus, "Hydrogen storage in single-walled carbon nanotubes at room temperature," *Science*, vol. 286, no. 5442, pp. 1127–1129, 1999.

[42] A. Peles, J. A. Alford, Z. Ma, L. Yang, and M. Y. Chou, "First-principles study of NaAlh$_4$ and na$_3$Alh$_6$ complex hydrides," *Physical review B*, vol. 70, p. 165105, Oct 2004.

[43] J. Iniguez, T. Yildirim, T. Udovic, M. Sulic, and C. Jensen, "Structure and hydrogen dynamics of pure and ti-doped sodium alanate," *Physical Review B*, vol. 70, no. 6, p. 060101, 2004.

[44] S. Chaudhuri and J. T. Muckerman, "First-principles study of ti-catalyzed hydrogen chemisorption on an al surface: a critical first step for reversible hydrogen storage in naalh4," *The Journal of Physical Chemistry B*, vol. 109, no. 15, pp. 6952–6957, 2005.

[45] W. Lohstroh and M. Fichtner, "Rate limiting steps of the phase transformations in ti-doped NaAlh$_4$ investigated by isotope exchange," *Physical review B*, vol. 75, p. 184106, May 2007.

[46] S. Bhattacharya, A. Bhattacharya, and G. Das, "Anti-kubas type interaction in hydrogen storage on a li decorated bhnh sheet: a first-principles based study," *The Journal of Physical Chemistry C*, vol. 116, no. 5, pp. 3840–3844, 2012.

[47] G. B. Wilson-Short, A. Janotti, K. Hoang, A. Peles, and C. G. Van de Walle, "First-principles study of the formation and migration of native defects in naalh$_4$," *Physical review B*, vol. 80, p. 224102, Dec 2009.

[48] T. K. Nielsen, M. Polanski, D. Zasada, P. Javadian, F. Besenbacher, J. Bystrzycki, J. Skibsted, and T. R. Jensen, "Improved hydrogen storage kinetics of nanoconfined

naalh4 catalyzed with ticl3 nanoparticles," *ACS nano*, vol. 5, no. 5, pp. 4056–4064, 2011.

[49] A. Peles and C. G. Van de Walle, "Role of charged defects and impurities in kinetics of hydrogen storage materials: A first-principles study," *Physical review B*, vol. 76, p. 214101, Dec 2007.

[50] C. Weidenthaler, A. Pommerin, M. Felderhoff, B. Bogdanović, and F. Schüth, "On the state of the titanium and zirconium in ti-or zr-doped naalh 4 hydrogen storage material," *Physical Chemistry Chemical Physics*, vol. 5, no. 22, pp. 5149–5153, 2003.

[51] M. Fichtner, O. Fuhr, O. Kircher, and J. Rothe, "Small ti clusters for catalysis of hydrogen exchange in naalh4," *Nanotechnology*, vol. 14, no. 7, p. 778, 2003.

[52] K. J. Gross, S. Guthrie, S. Takara, and G. Thomas, "In-situ x-ray diffraction study of the decomposition of naalh4," *Journal of Alloys and Compounds*, vol. 297, no. 1-2, pp. 270–281, 2000.

[53] H. Gunaydin, K. N. Houk, and V. Ozolins, "Vacancy-mediated dehydrogenation of sodium alanate," *Proceedings of the National Academy of Sciences*, vol. 105, no. 10, pp. 3673–3677, 2008.

[54] S. Saeidi, N. A. S. Amin, and M. R. Rahimpour, "Hydrogenation of co2 to value-added products?a review and potential future developments," *Journal of CO2 utilization*, vol. 5, pp. 66–81, 2014.

[55] G. A. Olah, G. S. Prakash, and A. Goeppert, "Anthropogenic chemical carbon cycle for a sustainable future," *Journal of the American Chemical Society*, vol. 133, no. 33, pp. 12881–12898, 2011.

[56] L. M. Aeshala, R. Uppaluri, and A. Verma, "Electrochemical conversion of co 2 to fuels: tuning of the reaction zone using suitable functional groups in a solid polymer

electrolyte," *Physical Chemistry Chemical Physics*, vol. 16, no. 33, pp. 17588–17594, 2014.

[57] S. Singh, B. Phukan, C. Mukherjee, and A. Verma, "Salen ligand complexes as electrocatalysts for direct electrochemical reduction of gaseous carbon dioxide to value added products," *RSC Advances*, vol. 5, no. 5, pp. 3581–3589, 2015.

[58] M. Gattrell, N. Gupta, and A. Co, "A review of the aqueous electrochemical reduction of co2 to hydrocarbons at copper," *Journal of electroanalytical Chemistry*, vol. 594, no. 1, pp. 1–19, 2006.

[59] X. Nie, M. R. Esopi, M. J. Janik, and A. Asthagiri, "Selectivity of co2 reduction on copper electrodes: the role of the kinetics of elementary steps," *Angewandte Chemie*, vol. 125, no. 9, pp. 2519–2522, 2013.

[60] W. Luo, W. Xie, R. Mutschler, E. Oveisi, G. L. De Gregorio, R. Buonsanti, and A. Züttel, "Selective and stable electroreduction of co2 to co at the copper/indium interface," *ACS Catalysis*, vol. 8, no. 7, pp. 6571–6581, 2018.

[61] M. Gong, W. Zhou, M.-C. Tsai, J. Zhou, M. Guan, M.-C. Lin, B. Zhang, Y. Hu, D.-Y. Wang, J. Yang, *et al.*, "Nanoscale nickel oxide/nickel heterostructures for active hydrogen evolution electrocatalysis," *Nature communications*, vol. 5, no. 1, pp. 1–6, 2014.

[62] S. Sarfraz, A. Garcia-Esparza, A. Jedidi, L. Cavallo, K. Takanabe, and A. Catal, "6, 2842-2851; b) y. zhao, c. wang, gg wallace," *Journal of Materials Chemistry A*, vol. 4, pp. 10710–10718, 2016.

[63] Z. B. Hoffman, T. S. Gray, K. B. Moraveck, T. B. Gunnoe, and G. Zangari, "Electrochemical reduction of carbon dioxide to syngas and formate at dendritic copper–indium electrocatalysts," *ACS Catalysis*, vol. 7, no. 8, pp. 5381–5390, 2017.

[64] S. Ma, M. Sadakiyo, M. Heima, R. Luo, R. T. Haasch, J. I. Gold, M. Yamauchi, and P. J. Kenis, "Electroreduction of carbon dioxide to hydrocarbons using bimetallic cu–pd catalysts with different mixing patterns," *Journal of the American Chemical Society*, vol. 139, no. 1, pp. 47–50, 2017.

[65] T. Shinagawa, G. O. Larrazábal, A. J. Martin, F. Krumeich, and J. Pérez-Ramirez, "Sulfur-modified copper catalysts for the electrochemical reduction of carbon dioxide to formate," *ACS Catalysis*, vol. 8, no. 2, pp. 837–844, 2018.

[66] S. Sarfraz, A. T. Garcia-Esparza, A. Jedidi, L. Cavallo, and K. Takanabe, "Cu–sn bimetallic catalyst for selective aqueous electroreduction of co2 to co," *ACS Catalysis*, vol. 6, no. 5, pp. 2842–2851, 2016.

[67] W. Zhu, L. Zhang, P. Yang, C. Hu, H. Dong, Z.-J. Zhao, R. Mu, and J. Gong, "Formation of enriched vacancies for enhanced co2 electrocatalytic reduction over aucu alloys," *ACS Energy Letters*, vol. 3, no. 9, pp. 2144–2149, 2018.

[68] R. Piercy and N. Hampson, "The electrochemistry of indium," *Journal of Applied Electrochemistry*, vol. 5, no. 1, pp. 1–15, 1975.

[69] Z. Geng, X. Kong, W. Chen, H. Su, Y. Liu, F. Cai, G. Wang, and J. Zeng, "Oxygen vacancies in zno nanosheets enhance co2 electrochemical reduction to co," *Angewandte Chemie*, vol. 130, no. 21, pp. 6162–6167, 2018.

[70] Y.-x. Pan, C.-j. Liu, D. Mei, and Q. Ge, "Effects of hydration and oxygen vacancy on co2 adsorption and activation on β-ga2o3 (100)," *Langmuir*, vol. 26, no. 8, pp. 5551–5558, 2010.

[71] S. Gao, Y. Lin, X. Jiao, Y. Sun, Q. Luo, W. Zhang, D. Li, J. Yang, and Y. Xie, "Partially oxidized atomic cobalt layers for carbon dioxide electroreduction to liquid fuel," *Nature*, vol. 529, no. 7584, pp. 68–71, 2016.

[72] B. Dibner and A. Volta, "Alessandro volta and the electric battery," 1964.

[73] P. Kurzweil, "Gaston planté and his invention of the lead–acid battery?the genesis of the first practical rechargeable battery," *Journal of Power Sources*, vol. 195, no. 14, pp. 4424–4434, 2010.

[74] M. S. Whittingham, "History, evolution, and future status of energy storage," *Proceedings of the IEEE*, vol. 100, no. Special Centennial Issue, pp. 1518–1534, 2012.

[75] M. S. Whittingham, "Lithium batteries and cathode materials," *Chemical reviews*, vol. 104, no. 10, pp. 4271–4302, 2004.

[76] B. Scrosati, "History of lithium batteries," *Journal of solid state electrochemistry*, vol. 15, no. 7-8, pp. 1623–1630, 2011.

[77] K. Xu, "Nonaqueous liquid electrolytes for lithium-based rechargeable batteries," *Chemical reviews*, vol. 104, no. 10, pp. 4303–4418, 2004.

[78] A. K. Padhi, K. S. Nanjundaswamy, and J. B. Goodenough, "Phospho-olivines as positive-electrode materials for rechargeable lithium batteries," *Journal of the electrochemical society*, vol. 144, no. 4, pp. 1188–1194, 1997.

[79] E. P. Roth and C. J. Orendorff, "How electrolytes influence battery safety," *The Electrochemical Society Interface*, vol. 21, no. 2, pp. 45–49, 2012.

[80] W. Li, L. Chen, Y. Sun, C. Wang, Y. Wang, and Y. Xia, "All-solid-state secondary lithium battery using solid polymer electrolyte and anthraquinone cathode," *Solid State Ionics*, vol. 300, pp. 114–119, 2017.

[81] J. Janek and W. G. Zeier, "A solid future for battery development," *Energy*, vol. 500, no. 400, p. 300, 2016.

[82] M. Armand and Tarascon, "Building better batteries," *nature*, vol. 451, no. 7179, p. 652, 2008.

[83] C. Monroe and J. Newman, "The impact of elastic deformation on deposition kinetics at lithium/polymer interfaces," *Journal of The Electrochemical Society*, vol. 152, no. 2, pp. A396–A404, 2005.

[84] G. Wang, D. Zhao, H. Bai, M. Pan, A. Xia, B. Han, X. Xi, Y. Wu, and W. Wang, "Nanoscale periodic morphologies on the fracture surface of brittle metallic glasses," *Physical review letters*, vol. 98, no. 23, p. 235501, 2007.

[85] S. Yu, R. D. Schmidt, R. Garcia-Mendez, E. Herbert, N. J. Dudney, J. B. Wolfenstine, J. Sakamoto, and D. J. Siegel, "Elastic properties of the solid electrolyte li7la3zr2o12 (llzo)," *Chemistry of Materials*, vol. 28, no. 1, pp. 197–206, 2015.

[86] J. E. Ni, E. D. Case, J. S. Sakamoto, E. Rangasamy, and J. B. Wolfenstine, "Room temperature elastic moduli and vickers hardness of hot-pressed llzo cubic garnet," *Journal of Materials Science*, vol. 47, no. 23, pp. 7978–7985, 2012.

[87] Y. H. Cho, J. Wolfenstine, E. Rangasamy, H. Kim, H. Choe, and J. Sakamoto, "Mechanical properties of the solid li-ion conducting electrolyte: Li 0.33 la 0.57 tio 3," *Journal of Materials Science*, vol. 47, no. 16, pp. 5970–5977, 2012.

[88] K. G. Schell, F. Lemke, E. C. Bucharsky, A. Hintennach, and M. Hoffmann, "Microstructure and mechanical properties of li 0.33 la 0.567 tio 3," *Journal of materials science*, vol. 52, no. 4, pp. 2232–2240, 2017.

[89] J. Wolfenstine, J. L. Allen, J. Sakamoto, D. J. Siegel, and H. Choe, "Mechanical behavior of li-ion-conducting crystalline oxide-based solid electrolytes: a brief review," *Ionics*, vol. 24, no. 5, pp. 1271–1276, 2018.

[90] N. Kamaya, K. Homma, Y. Yamakawa, M. Hirayama, R. Kanno, M. Yonemura, T. Kamiyama, Y. Kato, S. Hama, K. Kawamoto, *et al.*, "A lithium superionic conductor," *Nature materials*, vol. 10, no. 9, p. 682, 2011.

[91] F. Mizuno, A. Hayashi, K. Tadanaga, and M. Tatsumisago, "New, highly ion-conductive crystals precipitated from li2s–p2s5 glasses," *Advanced Materials*, vol. 17, no. 7, pp. 918–921, 2005.

[92] A. Hayashi, K. Noi, A. Sakuda, and M. Tatsumisago, "Superionic glass-ceramic electrolytes for room-temperature rechargeable sodium batteries," *Nature communications*, vol. 3, p. 856, 2012.

[93] K. Kataoka, H. Nagata, and J. Akimoto, "Lithium-ion conducting oxide single crystal as solid electrolyte for advanced lithium battery application," *Scientific reports*, vol. 8, no. 1, p. 9965, 2018.

[94] R. Kanno and M. Murayama, "Lithium ionic conductor thio-lisicon: The li2 s ges2 p 2 s 5 system," *Journal of the electrochemical society*, vol. 148, no. 7, pp. A742–A746, 2001.

[95] A. Rodger, J. Kuwano, and A. West, "Li+ ion conducting γ solid solutions in the systems li4xo4-li3yo4: X= si, ge, ti; y= p, as, v; li4xo4-lizo2: Z= al, ga, cr and li4geo4-li2cageo4," *Solid State Ionics*, vol. 15, no. 3, pp. 185–198, 1985.

[96] L. Kahle, A. Marcolongo, and N. Marzari, "Modeling lithium-ion solid-state electrolytes with a pinball model," *Physical Review Materials*, vol. 2, no. 6, p. 065405, 2018.

[97] A. Martinez-Juarez, C. Pecharroman, J. E. Iglesias, and J. M. Rojo, "Relationship between activation energy and bottleneck size for li+ ion conduction in nasicon materials of composition limm '(po4) 3; m, m '= ge, ti, sn, hf," *The Journal of Physical Chemistry B*, vol. 102, no. 2, pp. 372–375, 1998.

[98] S. Stramare, V. Thangadurai, and W. Weppner, "Lithium lanthanum titanates: a review," *Chemistry of materials*, vol. 15, no. 21, pp. 3974–3990, 2003.

[99] J. C. Bachman, S. Muy, A. Grimaud, H.-H. Chang, N. Pour, S. F. Lux, O. Paschos, F. Maglia, S. Lupart, P. Lamp, *et al.*, "Inorganic solid-state electrolytes for lithium batteries: mechanisms and properties governing ion conduction," *Chemical reviews*, vol. 116, no. 1, pp. 140–162, 2015.

[100] Y. Deng, C. Eames, B. Fleutot, R. David, J.-N. Chotard, E. Suard, C. Masquelier, and M. S. Islam, "Enhancing the lithium ion conductivity in lithium superionic conductor (lisicon) solid electrolytes through a mixed polyanion effect," *ACS applied materials & interfaces*, vol. 9, no. 8, pp. 7050–7058, 2017.

[101] S. P. Ong, Y. Mo, W. D. Richards, L. Miara, H. S. Lee, and G. Ceder, "Phase stability, electrochemical stability and ionic conductivity of the li 10 ± 1 mp 2 x 12 (m= ge, si, sn, al or p, and x= o, s or se) family of superionic conductors," *Energy & Environmental Science*, vol. 6, no. 1, pp. 148–156, 2013.

[102] S. Muy, J. C. Bachman, L. Giordano, H.-H. Chang, D. L. Abernathy, D. Bansal, O. Delaire, S. Hori, R. Kanno, F. Maglia, *et al.*, "Tuning mobility and stability of lithium ion conductors based on lattice dynamics," *Energy & Environmental Science*, vol. 11, no. 4, pp. 850–859, 2018.

[103] M. A. Kraft, S. P. Culver, M. Calderon, F. Boĺcher, T. Krauskopf, A. Senyshyn, C. Dietrich, A. Zevalkink, J. Janek, and W. G. Zeier, "Influence of lattice polarizability on the ionic conductivity in the lithium superionic argyrodites li6ps5x (x= cl, br, i)," *Journal of the American Chemical Society*, vol. 139, no. 31, pp. 10909–10918, 2017.

[104] K. Shimakawa and M. Aniya, "Dynamics of atomic diffusion in condensed matter: origin of the meyer–neldel compensation law," *Monatshefte für Chemie-Chemical Monthly*, vol. 144, no. 1, pp. 67–71, 2013.

[105] R. Sakanoi, T. Shimazaki, J. Xu, Y. Higuchi, N. Ozawa, K. Sato, T. Hashida, and M. Kubo, "Communication: different behavior of young's modulus and fracture strength of ceo2: density functional theory calculations.," *The Journal of Chemical Physics*, vol. 140, no. 12, pp. 121102–121102, 2014.

[106] A. Sakuda, A. Hayashi, and M. Tatsumisago, "Sulfide solid electrolyte with favorable mechanical property for all-solid-state lithium battery," *Scientific reports*, vol. 3, p. 2261, 2013.

[107] R. M. Martin and R. M. Martin, *Electronic structure: basic theory and practical methods.* Cambridge university press, 2004.

[108] M. Born and R. Oppenheimer, "Zur quantentheorie der molekeln," *Annalen der physik*, vol. 389, no. 20, pp. 457–484, 1927.

[109] C. F. Fischer, "Hartree–fock method for atoms. a numerical approach," 1977.

[110] P. Hohenberg and W. Kohn, "Inhomogeneous electron gas," *Physical review*, vol. 136, no. 3B, p. B864, 1964.

[111] W. Kohn and L. J. Sham, "Self-consistent equations including exchange and correlation effects," *Physical review*, vol. 140, pp. A1133–A1138, Nov 1965.

[112] W. Kohn and L. J. Sham, "Self-consistent equations including exchange and correlation effects," *Physical review*, vol. 140, no. 4A, p. A1133, 1965.

[113] F. M. Bickelhaupt and E. J. Baerends, "Kohn-sham density functional theory: predicting and understanding chemistry," *Reviews in computational chemistry*, vol. 15, pp. 1–86, 2000.

[114] W. Koch and M. C. Holthausen, *A chemist's guide to density functional theory.* John Wiley & Sons, 2015.

[115] J. P. Perdew and K. Burke, "Comparison shopping for a gradient-corrected density functional," *International journal of quantum chemistry*, vol. 57, no. 3, pp. 309–319, 1996.

[116] J. P. Perdew, M. Ernzerhof, and K. Burke, "Rationale for mixing exact exchange with density functional approximations," *The Journal of chemical physics*, vol. 105, no. 22, pp. 9982–9985, 1996.

[117] J. P. Perdew, K. Burke, and M. Ernzerhof, "Generalized gradient approximation made simple," *Physical review letters*, vol. 77, no. 18, p. 3865, 1996.

[118] J. E. Lennard-Jones, "The electronic structure of some diatomic molecules," *Transactions of the Faraday Society*, vol. 25, pp. 668–686, 1929.

[119] J. C. Slater, "Atomic shielding constants," *Physical Review*, vol. 36, no. 1, p. 57, 1930.

[120] S. F. Boys, "Electronic wave functions-i. a general method of calculation for the stationary states of any molecular system," *Proceedings of the Royal Society of London. Series A. Mathematical and Physical Sciences*, vol. 200, no. 1063, pp. 542–554, 1950.

[121] V. Blum, R. Gehrke, F. Hanke, P. Havu, V. Havu, X. Ren, K. Reuter, and M. Scheffler, "Ab initio molecular simulations with numeric atom-centered orbitals," *Computer Physics Communications*, vol. 180, no. 11, pp. 2175–2196, 2009.

[122] F. Bloch, "Über die quantenmechanik der elektronen in kristallgittern," *Zeitschrift für physik*, vol. 52, no. 7, pp. 555–600, 1929.

[123] C. Kittle, "Introduction to solid state physics (2005)."

[124] D. Hamann, M. Schlüter, and C. Chiang, "Norm-conserving pseudopotentials," *Physical Review Letters*, vol. 43, no. 20, p. 1494, 1979.

[125] D. J. Singh and L. Nordstrom, *Planewaves, Pseudopotentials, and the LAPW method*. Springer Science & Business Media, 2006.

[126] L. Kleinman and D. Bylander, "Efficacious form for model pseudopotentials," *Physical Review Letters*, vol. 48, no. 20, p. 1425, 1982.

[127] S. Goedecker and K. Maschke, "Transferability of pseudopotentials," *Physical Review A*, vol. 45, no. 1, p. 88, 1992.

[128] D. Vanderbilt, "Soft self-consistent pseudopotentials in a generalized eigenvalue formalism," *Physical review B*, vol. 41, no. 11, p. 7892, 1990.

[129] J. C. Slater, "Wave functions in a periodic potential," *Physical Review*, vol. 51, no. 10, p. 846, 1937.

[130] O. K. Andersen, "Linear methods in band theory," *Phys. Rev. B*, vol. 12, pp. 3060–3083, Oct 1975.

[131] P. E. Blöchl, "Projector augmented-wave method," *Phys. Rev. B*, vol. 50, pp. 17953–17979, Dec 1994.

[132] A. Baldereschi, "Mean-value point in the brillouin zone," *Physical Review B*, vol. 7, no. 12, p. 5212, 1973.

[133] D. J. Chadi and M. L. Cohen, "Special points in the brillouin zone," *Physical Review B*, vol. 8, no. 12, p. 5747, 1973.

[134] H. J. Monkhorst and J. D. Pack, "Special points for brillouin-zone integrations," *Physical review B*, vol. 13, no. 12, p. 5188, 1976.

[135] P. Wisesa, K. A. McGill, and T. Mueller, "Efficient generation of generalized monkhorst-pack grids through the use of informatics," *Physical Review B*, vol. 93, no. 15, p. 155109, 2016.

[136] R. L. Johnston, "Evolving better nanoparticles: Genetic algorithms for optimising cluster geometries," *Dalton Transactions*, no. 22, pp. 4193–4207, 2003.

[137] S. M. Woodley and R. Catlow, "Crystal structure prediction from first principles," *Nature materials*, vol. 7, no. 12, pp. 937–946, 2008.

[138] L. B. Vilhelmsen and B. Hammer, "A genetic algorithm for first principles global structure optimization of supported nano structures," *The Journal of chemical physics*, vol. 141, no. 4, p. 044711, 2014.

[139] S. Bhattacharya, S. V. Levchenko, L. M. Ghiringhelli, and M. Scheffler, "Efficient ab initio schemes for finding thermodynamically stable and metastable atomic structures: Benchmark of cascade genetic algorithms," *New Journal of Physics*, vol. 16, no. 12, p. 123016, 2014.

[140] H. C. Andersen, "Molecular dynamics simulations at constant pressure and/or temperature," *The Journal of chemical physics*, vol. 72, no. 4, pp. 2384–2393, 1980.

[141] R. P. Feynman, "Forces in molecules," *Physical review*, vol. 56, no. 4, p. 340, 1939.

[142] H. J. Berendsen, J. v. Postma, W. F. van Gunsteren, A. DiNola, and J. R. Haak, "Molecular dynamics with coupling to an external bath," *The Journal of chemical physics*, vol. 81, no. 8, pp. 3684–3690, 1984.

[143] S. Nosé, "A unified formulation of the constant temperature molecular dynamics methods," *The Journal of chemical physics*, vol. 81, no. 1, pp. 511–519, 1984.

[144] S. Nosé, "A molecular dynamics method for simulations in the canonical ensemble," *Molecular physics*, vol. 52, no. 2, pp. 255–268, 1984.

[145] G. J. Martyna, M. L. Klein, and M. Tuckerman, "Nosé–hoover chains: The canonical ensemble via continuous dynamics," *The Journal of chemical physics*, vol. 97, no. 4, pp. 2635–2643, 1992.

[146] X. Ke and I. Tanaka, "Decomposition reactions for $NaAlh_4$, na_3Alh_6, and nah: First-principles study," *Physical review B*, vol. 71, p. 024117, Jan 2005.

[147] A. Bhattacharya, S. Bhattacharya, C. Majumder, and G. Das, "Transition-metal decoration enhanced room-temperature hydrogen storage in a defect-modulated graphene sheet," *The Journal of Physical Chemistry C*, vol. 114, no. 22, pp. 10297–10301, 2010.

[148] S. Bhattacharya, C. Majumder, and G. Das, "3d transition metal decorated bcn composite nanostructures for efficient hydrogen storage: A first-principles study," *Bulletin of Materials Science*, vol. 32, no. 3, pp. 353–360, 2009.

[149] S. Bhattacharya, S. V. Levchenko, L. M. Ghiringhelli, and M. Scheffler, "Stability and metastability of clusters in a reactive atmosphere: Theoretical evidence for unexpected stoichiometries of mg m o x," *Physical review letters*, vol. 111, no. 13, p. 135501, 2013.

[150] S. Bhattacharya, D. Berger, K. Reuter, L. M. Ghiringhelli, and S. V. Levchenko, "Theoretical evidence for unexpected o-rich phases at corners of mgo surfaces," *Physical Review Materials*, vol. 1, p. 071601, Dec 2017.

[151] S. Bhattacharya, S. V. Levchenko, L. M. Ghiringhelli, and M. Scheffler, "Efficient ab initio schemes for finding thermodynamically stable and metastable atomic structures: benchmark of cascade genetic algorithms," *New Journal of Physics*, vol. 16, no. 12, p. 123016, 2014.

[152] A. Bhattacharya and S. Bhattacharya, "Exploring n-rich phases in li x n y clusters for hydrogen storage at nanoscale," *The journal of physical chemistry letters*, vol. 6, no. 18, pp. 3726–3730, 2015.

[153] A. Togo and I. Tanaka, "First principles phonon calculations in materials science," *Scripta Materialia*, vol. 108, pp. 1 – 5, 2015.

[154] N. A. Richter, S. Sicolo, S. V. Levchenko, J. Sauer, and M. Scheffler, "Concentration of vacancies at metal-oxide surfaces: Case study of mgo(100)," *Physical Review Letters*, vol. 111, p. 045502, Jul 2013.

[155] S. Bhattacharya, C. Majumder, and G. Das, "Ti-decorated bc4n sheet: A planar nanostructure for high-capacity hydrogen storage," *The Journal of Physical Chemistry C*, vol. 113, no. 36, pp. 15783–15787, 2009.

[156] M. Tahir and N. S. Amin, "Indium-doped tio2 nanoparticles for photocatalytic co2 reduction with h2o vapors to ch4," *Applied Catalysis B: Environmental*, vol. 162, pp. 98–109, 2015.

[157] E. Karamian and S. Sharifnia, "On the general mechanism of photocatalytic reduction of co2," *Journal of CO2 Utilization*, vol. 16, pp. 194–203, 2016.

[158] B. Kumar, M. Llorente, J. Froehlich, T. Dang, A. Sathrum, and C. P. Kubiak, "Photochemical and photoelectrochemical reduction of co2," *Annual review of physical chemistry*, vol. 63, pp. 541–569, 2012.

[159] P. Farinazzo Bergamo Dias Martins, P. Papa Lopes, E. A. Ticianelli, V. R. Stamenkovic, N. M. Markovic, and D. Strmcnik, "Hydrogen evolution reaction on copper: Promoting water dissociation by tuning the surface oxophilicity," *Electrochemistry Communications*, vol. 100, pp. 30–33, 2019.

[160] H. Xie, T. Wang, J. Liang, Q. Li, and S. Sun, "Cu-based nanocatalysts for electro-chemical reduction of co2," *Nano Today*, vol. 21, pp. 41–54, 2018.

[161] N. C. Bartelt, Y. Li, J. D. Sugar, K. Fenton, A. L. D. Kilcoyne, D. A. Shapiro, T. Tyliszczak, W. C. Chueh, and F. El Gabaly, "Simple stochastic model of multi-particle battery electrodes undergoing phase transformations," *Phys. Rev. Applied*, vol. 10, p. 044056, Oct 2018.

[162] X. Jiang, B. Song, and D. Tománek, "Formation dynamics of potassium-based graphite intercalation compounds: An ab initio study," *Phys. Rev. Applied*, vol. 9, p. 044015, Apr 2018.

[163] A. Moradabadi and P. Kaghazchi, "Effect of strain on polaron hopping and electronic conductivity in bulk licoo$_2$," *Phys. Rev. Applied*, vol. 7, p. 064008, Jun 2017.

[164] S. Pugh, "Xcii. relations between the elastic moduli and the plastic properties of polycrystalline pure metals," *The London, Edinburgh, and Dublin Philosophical Magazine and Journal of Science*, vol. 45, no. 367, pp. 823–843, 1954.

[165] R. J. Friauf, "Correlation effects for diffusion in ionic crystals," *Journal of Applied Physics*, vol. 33, no. 1, pp. 494–505, 1962.

[166] A. Marcolongo and N. Marzari, "Ionic correlations and failure of nernst-einstein relation in solid-state electrolytes," *Physical Review Materials*, vol. 1, no. 2, p. 025402, 2017.

[167] N. J. De Klerk, I. Rosioní, and M. Wagemaker, "Diffusion mechanism of li argyrodite solid electrolytes for li-ion batteries and prediction of optimized halogen doping: the effect of li vacancies, halogens, and halogen disorder," *Chemistry of Materials*, vol. 28, no. 21, pp. 7955–7963, 2016.

List of publications

1. **Ekta Arora**, Shikha Saini, Pooja Basera, Manish Kumar, Arunima Singh,and Saswata Bhattacharya, "Elucidating the Role of Temperature and Pressure to the Thermodynamic Stability of Charged Defects in Complex Metal-Hydrides: A Case Study of $NaAlH_4$", The Journal of Physical Chemistry C **123**, 62 (2019).

2. Pinki Devi, Karan Malik, **Ekta Arora**, Saswata Bhattacharya, V. Kalendra, K. V. Lakshmi, Anil Verma, and Jitendra P. Singh, "Selective electrochemical reduction of CO_2 to CO on CuO/In_2O_3 nanocomposites: role of oxygen vacancies",Catal. Sci. Technol. **9**, 5339 (2019)

3. Pooja Basera, Shikha Saini, **Ekta Arora**, Arunima Singh, Manish Kumar, and Saswata Bhattacharya, "Stability of non-metal Dopants to Tune the Photo-absorption of TiO_2 at Realistic Temperatures and Oxygen Partial Pressures: A Hybrid DFT Study", Scientific Reports **9**, 11427 (2019).

4. Shikha Saini, Pooja Basera, **Ekta Arora**, and Saswata Bhattacharya, "Unraveling Thermodynamic Stability, Catalytic Activity and Electronic Structure of $[TM_xMg_yO_z]^{+/0/-}$ clusters at Realistic Conditions: A Hybrid DFT and *Ab initio* Thermodynamics Study", The Journal of Physical Chemistry C **123**, 15495 (2019).

Conference proceedings

1. Shikha Saini, Pooja Basera, **Ekta Arora**, Saswata Bhattacharya, "Electronic Structure and. Thermodynamic Stability of Ternary Oxide Clusters (Ni1Mg1Ox)", AIP Conference Proceedings, 2115, 030190 (2019).

2. Pooja Basera, Shikha Saini, **Ekta Arora**, Arunima Singh, Saswata Bhattacharya, "Electronic, Magnetic and Optical Properties of C, N-doped TiO2 Anatase: A Hybrid Density Functional Study", AIP Conference Proceedings, 2115, 030394 (2019).

3. Pooja Basera, Shikha Saini, **Ekta Arora**, Arunima Singh, and Saswata Bhattacharya, "Ab-initio Study on Opto-Electronic Properties of Non-metal Doped TiO2", Materials today: proceedings (2019). DOI: 10.1016/j.matpr.2019.05.393

Author's Bio-data

Personal data

Name:	Ekta Arora
Affiliation:	Department of Physics, Indian Institute of Technology Delhi
Date of birth:	25/10/1991
Nationality:	Indian
Sex:	Female
Marrital status:	Married
Email:	ektaarora1990@gmail.com

Profile

Ekta Arora is a research scholar in the deparment of physics, Indian Institute of Technology Delhi since july 2016. She has been persuing her research work under the guidance of Dr. Saswata Bhattacharya. Her research interests include a broad range of solid-state materials used as advanced energy materials. She uses the state-of-the-art Density Functional Theory (DFT) in addition to *ab initio* atomistic thermodynamics to study the properties of the advanced energy materials at various experimental conditions. She employs *ab inito* molecular dynamics (AIMD) simulations to investigate the diffusion of defects or ions in the bulk materials.

Education

2016-2021	Ph.D in physics, Department of Physics, Indian Institute of Technology Delhi, Hauz Khas, New Delhi 110016, INDIA. Thesis title: *Understanding Defects in Advanced Energy Materials from First-Principles Calculations* Course work grade: B (8.5 CGPa)
2013-2015	MSc. Physics, Maharishi Dayanand University, Rohtak, Haryana. Overall percentage: 67%
2009-2012	BSc. (Hons.) Physics, Miranda House College, University of Delhi, Delhi. Overall percentage: 74%

Technical skills

Methods:	Density Functional Theory (DFT), *Ab Initio* Atomistic Thermodynamics, *Ab Initio* Molecular Dynamics (AIMD), PHONOPY, Genetic Algorithm
Programming:	Python, Matlab, Shell
Electronic structure codes:	VASP, FHI-AIMS
Softwares:	Gnuplot, JMOL, VESTA, Xmgrace, Matplotlib

Conference attended

- International Conference On Nano Science & Engineering Applications (ICONSEA-2018), 4-6th October 2018, at CNST, IST, JNTU Hyderabad, India .
(Poster presentation)

- International Workshop on Nano/Micro 2D-3D Fabrication, Manufacturing of Electronic Biomedical Devices & Applications (IWNEBD-2018), 31st October to 2nd November 2018, at IIT Mandi, H.P, India.
(Poster presentation)

- Workshop and Symposium on Advanced Simulation Methods: DFT, MD and Beyond (ASM-2019), 6-10th March 2019, at Indian Institute of Technology Delhi, India.
(Oral and poster presentation).

Awards and academic recognitions

- Recipient of best poster presentation award in ICONSEA-2018 held at CNST, IST, JNTU Hyderabad, India.

- Recipient of best poster presentation award in IWNEBD-2018 held at IIT Mandi, H.P, India.

- Recipient of best poster presentation award in ASM-2019 held at IIT Delhi, Delhi, India.

- Recipient of best poster presentation award in departmental symposium at department of physics, IIT Delhi (April 2019).

- All India Rank 51 in GATE-2016 examination.